

Search for $W' \rightarrow t\bar{b}$ in $p\bar{p}$ Collisions at $\sqrt{s} = 1.96$ TeV

by

J. Clark Cully

A dissertation submitted in partial fulfillment
of the requirements for the degree of
Doctor of Philosophy
(Physics)
in The University of Michigan
2009

Doctoral Committee:

Professor Dante E. Amidei, Chair
Professor David W. Gerdes
Professor Keith Riles
Professor James D. Wells
Assistant Professor Robert J. Adams

*“Whatever things are true, Whatever things are noble,
Whatever things are just, Whatever things are pure,
Whatever things are lovely, Whatever things are of good report,
If there is any virtue and if there is anything praiseworthy,
Meditate on these things.”*

— Phillipians 4:8

© J. Clark Cully 2009
All Rights Reserved

ACKNOWLEDGEMENTS

First and foremost I would like to offer my heartfelt gratitude to Professor Dan Amidei. He has truly been the model advisor, scholar, and mentor. I richly value his efforts to pass on his knowledge and passion for particle physics. Only his investment in my education and career has made this dissertation possible. I am in his debt.

I also appreciate the support of my friends and classmates over the years. In particular I am fortunate to have known Glenn Strycker and Nick Licata. Their charitable wisdom and humor made it possible to endure many dark hours of coursework; I could not have succeeded without them. I wish them both the best on the journey ahead.

Many Michigan CDF alumni helped shorten my long learning curve. In particular, thank you to Tom Schwarz not only for showing me the ropes, but also for passing on his plush data validation job and all his legacy analysis code. Bo Jayatilka and Kathy Copic are among two of the brightest young people I know, but I have most valued most their hospitality and generosity. Professors Dave Gerdes and Myron Campbell, and the rest of the CDF research staff, have all contributed to Michigan's strong support for particle physics.

There have been many people at Fermilab who helped me get acquainted with the many facets of life at CDF. I would like to single out Michigan veterans Tom Wright and Alexi Varganov, as well as Kevin Lannon, Bernd Stelzer and Peter Dong. They have all taught me a great deal and been reliable resources whenever I needed help tackling a problem. I

would also like to acknowledge the full support given to me by the leaders of the top and single-top groups.

Thank you to my committee for their time and effort; I appreciate the opportunity to share all the interesting things I have learned.

And finally, thank you to my wife for her unending grace, my family for their constant encouragement, and the Lord Jesus Christ for blessing me with people such as these. It has been quite the ride and I cherish being given the opportunity to chase after the mysteries of our universe.

TABLE OF CONTENTS

ACKNOWLEDGEMENTS	ii
LIST OF FIGURES	vii
LIST OF TABLES	x
CHAPTER	
1. The Standard Model and the W'	1
1.1 Introduction	1
1.2 The Standard Model	2
1.2.1 Development of the Standard Model	2
1.2.2 Overview of the Standard Model	3
1.3 Searching for a New Particle	10
1.4 Luminosity, Cross-section, and Branching Ratio	11
1.5 Features of a W'	12
1.6 W' Search Methodology and $t\bar{b}$ Mass	14
2. Fermilab and the CDF Experiment	16
2.1 Fermilab and the Tevatron	16
2.2 Accelerator Complex	17
2.3 CDF Detector	21
2.3.1 CDF Coordinate System	22
2.3.2 Silicon Tracking System	23
2.3.3 Central Outer Tracker	25
2.3.4 Electromagnetic Calorimeter and ShowerMax Detector	25
2.3.5 Hadronic Calorimeter	26
2.3.6 Muon Chambers	27
2.3.7 Neutrino Detection	28
2.4 CDF Data Acquisition System	29
3. Event Selection	33
3.1 W' Decay Signature	33
3.2 Triggers	35
3.3 Lepton Selection	37
3.3.1 Tight Central Electron Selection	37
3.3.2 Tight Phoenix Electron Selection	38
3.3.3 Tight Muon Selection	39
3.3.4 Loose Muon Selection	39
3.4 Jet Selection	40
3.4.1 Jet Energy Corrections	41

3.4.2	b -Tagging	42
3.5	\cancel{E}_T Selection	43
3.5.1	Non- W Background Removal	44
3.6	Other Selection Criteria	45
3.7	Event Selection Summary	46
4.	Background Modeling	47
4.1	Sources of Background	48
4.1.1	W +Jets	48
4.1.2	$t\bar{t}$	49
4.1.3	Single-Top	49
4.1.4	Diboson	50
4.1.5	Z +jets	51
4.1.6	Non- W	51
4.2	Background Simulations	52
4.2.1	Removal of Overlap in Background Simulations	53
4.2.2	b -Tagging Treatment and Weighting of Simulated Events	54
4.2.3	Mistag Model	56
4.2.4	Non- W Model	56
4.3	Preliminary Background Contributions	57
4.4	Correction to Bottom and Charm Fractions in Simulation	59
4.5	Corrected Background Contributions	63
4.6	Validation of Background Prediction	64
5.	W' Signal Measurement	70
5.1	Methodology	70
5.2	W' Simulation	71
5.3	Selecting a Kinematic Distribution	71
5.4	$M_{t\bar{b}}$ Distribution	72
5.4.1	Solving for P_z^ν	73
5.5	Measuring the Signal Contribution	74
5.5.1	Setting W' Limits with CL_s	74
5.5.2	Grouping of Background Components	76
5.5.3	Fitting Channels in Parallel	76
5.6	Expected Limits	77
6.	Systematic Uncertainties	86
6.1	Jet Energy Scaling	87
6.2	b -tag Scale-Factor Uncertainty	89
6.3	Initial and Final State Radiation	91
6.4	Signal Acceptance	91
6.4.1	Integrated Luminosity	91
6.4.2	Lepton Acceptance	92
6.4.3	Parton Distribution Functions	92
6.5	Background Acceptance	93
6.6	ALPGEN Q^2 Scale	93
6.7	Mistag and Non- W Modeling	94
6.8	Top-Quark Mass	95
7.	Conclusion	101

BIBLIOGRAPHY 104

LIST OF FIGURES

Figure

1.1	Grouping of quarks and leptons based upon the forces in which they participate [5]. . .	5
1.2	Graph of the Standard Model particles with lines illustrating the interactions mediated by each type of boson. From [8].	9
1.3	Dominant s -channel Feynman diagram for production of a positively charged W' and subsequent decay to $t\bar{b}$. This signal is the focus of this analysis.	13
2.1	An overview of the Fermilab accelerator complex.	18
2.2	Cutaway view of CDF.	22
2.3	Cross-section view of the CDF tracking and calorimeter systems.	24
2.4	Penetration of various particles through the detector layers.	27
2.5	Angular coverage of each set of muon chambers. The BMU is not shown.	29
2.6	Schematic of the CDF data acquisition system.	31
3.1	$W' \rightarrow t\bar{b}$ Feynman diagrams for hadronic decay (left) and for leptonic decay (right). . .	34
3.2	Total Tevatron production cross-section of various background processes. The $W' \rightarrow t\bar{b}$ cross-section is expected to be smaller than that shown for single-top production.	34
3.3	Illustration of secondary vertex identification. The figure on the left shows a displacement opposite the jet direction: a negative tag likely from track mismeasurement. On the right, the vertex displacement matches the jet direction, consistent with a b -hadron conserving momentum during its decay.	43
3.4	Tight SecVTX tagging efficiency as a function of jet energy for b -jets from top decay. From [25]	44
4.1	Representative Feynman diagram for $Wb\bar{b}$, $Wc\bar{c}$, and $W+l\bar{l}$ production to two jets (left) and to three jets (right).	48
4.2	Representative Feynman diagram for Wc production.	49
4.3	Feynman diagram for s -channel single top production (left), and t -channel single top production (right).	50
4.4	Representative Feynman diagram for WW , WZ , and ZZ production.	51

4.5	Standard Model prediction as a function of jet multiplicity.	60
4.6	Fit of the bottom and charm fractions in $W+1$ jet data using the loose secondary vertex mass distribution (left) and using the KNN discriminant distribution (right). The light-flavor fraction is fixed to its expected contribution.	62
4.7	k-factors for bottom (blue) and charm (red), using loose <code>SecVtx</code> mass and the KNN discriminant. In $W+1$ jet bin we measure approximately $KF = 1.4$ for both bottom and charm. The $W+2$ jet case is shown only for error estimation.	63
4.8	Standard Model prediction as a function of jet multiplicity after applying the correction to heavy-flavor fraction.	65
4.9	Comparison of the model lepton P_T distribution to the data for the 2 jet 1 b -tag channel (left) and the 3 jets 1 b -tag channel (right). The bottom row shows the plots on a log scale.	66
4.10	Comparison of the model lead jet E_T distribution to data for the 2 jet 1 b -tag channel (left) and the 3 jets 1 b -tag channel (right). The bottom row shows the plots on a log scale.	67
4.11	Comparison of the model \cancel{E}_T distribution to data for the 2 jet 1 b -tag channel (left) and the 3 jets 1 b -tag channel (right). The bottom row shows the plots on a log scale.	68
4.12	Comparison of the model transverse W mass distribution to data for the 2 jet 1 b -tag channel (left) and the 3 jet 1 b -tag channel (right). The bottom row shows the plots on a log scale.	69
5.1	Comparison of various signal distributions. The $M_{t\bar{b}}$ distribution is shown to have separation from background superior to its individual inputs.	79
5.2	Comparison of the $M_{t\bar{b}}$ distribution shape in signal and in background. Models for several different W' masses are shown, set to arbitrary normalization.	80
5.3	This figure shows how P_{S+B} and P_B are determined by plotting $\chi^2(data H_{S+B}) - \chi^2(data H_B)$ for ensembles of H_{S+B} pseudo-experiments and H_B pseudo-experiments. CL_s is the ratio of P_{S+B} (blue area) to P_B (red area).	81
5.4	Comparison of the background shapes (normalized to unit area) in each grouping.	82
5.5	Comparison of the $M_{t\bar{b}}$ distribution in data to background expectation. Channels are separated according to the number of jets and b -tags. No large discrepancy is apparent.	83
5.6	Expected 95% C.L. upper limits for each channel individually. The 2 jet 1 b -tag channel, with its small top fraction, is the most sensitive.	84
5.7	Comparison of expected 95% C.L. upper limits among various lepton types.	85
6.1	Expected sensitivity including various systematic uncertainties.	88
6.2	Comparison of the nominal background distributions (blue), 1σ JES varied background distributions (green), and 3σ JES varied background distributions (red). Positive variations are on the left and negative variations are on the right.	96
6.3	Comparison of the nominal background distributions (blue), 1σ JES varied background distributions (green), and 3σ JES varied background distributions (red). Positive variations are on the left and negative variations are on the right.	97

6.4	The lead jet E_T spectrum for W' of $950 \text{ GeV}/c^2$	98
6.5	Current calculation for the b -tag scale factor [44]	98
6.6	Comparison of the nominal $800 \text{ GeV}/c^2$ W' distribution (blue), $+1\sigma$ b -tag scale factor varied distribution (green), and -1σ b -tag scale factor varied distribution (red).	99
6.7	Comparison of the nominal $800 \text{ GeV}/c^2$ W' distribution (blue), $+1\sigma$ variation (green), and -1σ variation (red) for ISR (left) and FSR (right).	99
6.8	Comparison of the default W +bottom background distribution with nominal Q^2 scale (blue), alternative distribution with the Q^2 scale doubled (green), and the alternative distribution with the Q^2 scale halved (red).	100
6.9	Comparison of the default mistag/non- W model (blue) and the $\pm 1\sigma$ variation (green) of the mistag model (left) and of the non- W model (right). For the mistag model variation we substitute pretag data, and for the non- W model variation we use non-isolated electron data in place of anti-electron data.	100
7.1	Expected and observed 95% C.L. limits on $\sigma \times \text{BR}(W' \rightarrow t\bar{b})$ as function of $M_{W'}$ for 1.9 fb^{-1} , along with theoretical predictions for a W'_R with Standard Model coupling strength.	102
7.2	Observed 95% C.L. upper limits on the W' coupling strength compared to the Standard Model coupling, $g_{W'}/g_W$, as function of $M_{W'}$ for 1.9 fb^{-1} . The shaded regions above the lines are excluded.	103

LIST OF TABLES

Table

1.1	Fundamental particles in the Standard Model [6]. The undiscovered Higgs boson is not listed. Note also that the masses of free quarks can only be indirectly inferred due to color confinement, and that neutrinos are massless in the Standard Model. Because they have been experimentally shown to have a small mass, neutrinos and antineutrinos may in fact be identical.	6
1.2	Electroweak transformation properties of quarks and leptons. The subscripts L and R indicate the left- and right-handed helicities. The left-handed states transform as SU(2) doublets and the right-handed states as singlets.	8
1.3	Predictions for $\sigma \times \text{BR}(W' \rightarrow t\bar{b})$ and expected number of events in 1.9 fb^{-1} using our selection, as a function of W' mass.	14
4.1	Simulated background components and associated datasets.	53
4.2	Theoretical cross-sections for electroweak backgrounds produced via $p\bar{p} \rightarrow X$	58
4.3	Result of heavy-flavor fits in $W+1$ jet data using the secondary vertex mass for loose tags (left) and the KNN discriminant (right).	63
4.4	Standard Model background predictions for tagged event in 1.9 fb^{-1}	64
5.1	Predicted background (BG) and signal events in 1.9 fb^{-1} in the case of $M_{W'}=800 \text{ GeV}/c^2$ and $M_{W'} < M_{\nu_R}$	70
5.2	Background processes are combined into five components.	76
6.1	Sources of systematic uncertainty for each background process	87
7.1	Expected and observed 95% C.L. upper limits on $\sigma \times \text{BR}(W' \rightarrow t\bar{b})$ as function of $M_{W'}$ for 1.9 fb^{-1} , including both statistical and systematic uncertainties.	102

CHAPTER 1

The Standard Model and the W'

1.1 Introduction

The fundamental goal of science is to explain all the complex phenomena of the physical universe in terms of simple rules. We often do not take the time to marvel at how successful this endeavor has been, nor should we have expected it. It should be astounding that our minds, with a little help from calculus, can understand galaxies we will never reach, times long before we existed, and features trillions of times larger or smaller than we can comprehend. We are indeed fortunate that such consistency exists, allowing our narrow perspectives in time and space to tell us of the deep, vast, immeasurable sea of the cosmos. In fact, we can understand and explore many concepts such as a fourth spatial dimension that we are not even capable of imagining! Such is the quantum world of particle physics.

The last few decades have shown us just how connected this topic is to the great mysteries of science: how the universe began, how will it end, the enigmas of dark matter and dark energy, the universe's precise suitability for life, extra dimensions, and many other wonders. The properties uncovered in our particle colliders inform our cosmic theories. Many are optimistic that with the discoveries expected at the Large Hadron Collider, a revolution is at hand. Perhaps we will be the generation to officiate the marriage of general relativity to the quantum world.

Some see this as an inevitable triumph of reductionism, but I prefer to see it as the triumph of beauty in the design of the universe (or perhaps multiverse). The beauty comes from underlying symmetries which seem to be hidden in plain sight. There is an incredibly compact efficiency in these properties, a simplicity which allows us to discover the familiar in very unfamiliar places. Particle physics is a quest in search of this beauty, and I consider the adventure among our greatest cultural, as well as scientific, endeavors.

1.2 The Standard Model

1.2.1 Development of the Standard Model

The nineteenth century reveled in the scientific triumph of Maxwell's equations, compactly unifying all electrical and magnetic laws. A great many disparate phenomena were now related via the conceptualization of an electromagnetic field permeating all space, much as Newton unified terrestrial and celestial mechanics. The euphoria that science may be nearing completion did not last long. In 1905, Einstein realized that photon energies were quantized, and that the speed of light should be independent of reference frame. The quantum revolution, which is still ongoing, soon led to a quantized theory of electromagnetic fields. Modified for consistency with special relativity, it soon evolved into quantum electrodynamics.

The advent of accelerator research after World War II soon led to a zoo of new particles the old theories could not explain. Patterns emerged, such as the "Eightfold-Way", confirming that these new particles were composites of more fundamental particles known as quarks. Using the powerful gauge formalism of quantum electrodynamics, quantum chromodynamics was developed to describe the new strong nuclear force which binds quarks together.

Another strange discovery was that some reactions only occur in particles with left-

handed spin orientations, violating the assumption that nature was invariant under mirror reflections (parity). The behavior of this weak interaction, responsible for beta decay, had many similarities to the better understood electromagnetic force. While attempting to explain why particles have mass, a new symmetry was introduced which proposed that the two forces were in fact low-energy manifestations of a single force, described by quantum electroweak theory [1].

Quantum electroweak theory and quantum chromodynamic theory [2] combined are known the Standard Model, which fully explains the strong, weak, and electromagnetic forces. Einstein would spend the rest of his life unsuccessfully attempting to devise a quantum theory for gravity as well. Nonetheless, the Standard Model provides a complete description of the quantum mechanical universe because the effect of gravity is negligible on such small scales. The Standard Model has been tested to greater precision than any other theory, and its predictions have withstood rigorous experimental validation over the last thirty years.

1.2.2 Overview of the Standard Model

Fundamental particles are point-like objects, with no known internal structure, described only by a small number of quantum properties. One important property is intrinsic angular momentum, or spin. The implied notion of rotation is only an analogy. Spins are angular momentum vectors with magnitudes that are quantized as integer or half-integer values. Particles with half-integer spin are called fermions, and particles with integer spin are called bosons. To date, all fundamental particles are spin $\frac{1}{2}$ or spin 1. Particles may have additional quantized properties, generally called charges, which correspond to each of the forces. The conservation of these charge types, along with energy and mass conservation, determine the interactions allowed by the Standard Model.

Quarks are fermions that have nonzero values for all types of charge. There are six types, or “flavors”, of quark: up, down, charm, strange, top, and bottom. They are grouped into three pairs, one with an electric charge of $+\frac{2}{3}$ and one with $-\frac{1}{3}$. These pairs are referred to as families or generations, and differ only in mass. The $171 \text{ GeV}/c^2$ top quark was discovered in 1995 at Fermilab [3] after nearly twenty years of searching, and was the final quark to complete the Standard Model.

Leptons are fermions that do not have strong charge, called “color”, and transform as singlets in strong interactions. The electron, muon, and tau all have an electric charge of -1, differing only in mass. They are paired into three generations along with a corresponding neutrino, which has no color or electric charge. Neutrinos are only created or destroyed via weak interactions.

One of the curious features of nature is that all normal matter is composed of only particles from the first generation. Atoms simply consist of electrons orbiting the protons and neutrons formed from up and down quarks. The impact on the structure of the universe from the dozens of other particles is still being explored.

The various types of fermions are illustrated in Figure 1.1 and Table 1.1 shows all their properties. Note that each quark can have three different strong charges and gluons can have eight (discussed below). Also listed is each fermion’s antimatter counterpart. An antiparticle has the same mass and spin as an ordinary particle, but the charges are opposite. Thus an antielectron, or positron, is identical to an electron with positive charge. Though the Standard Model treats them as distinct, it has not been demonstrated experimentally whether neutrinos are separate from their antimatter version (Majorana condition) [4].

The bosons in the Standard Model are determined by its mathematical properties known as gauge symmetries: transformations under which the theory is invariant. They

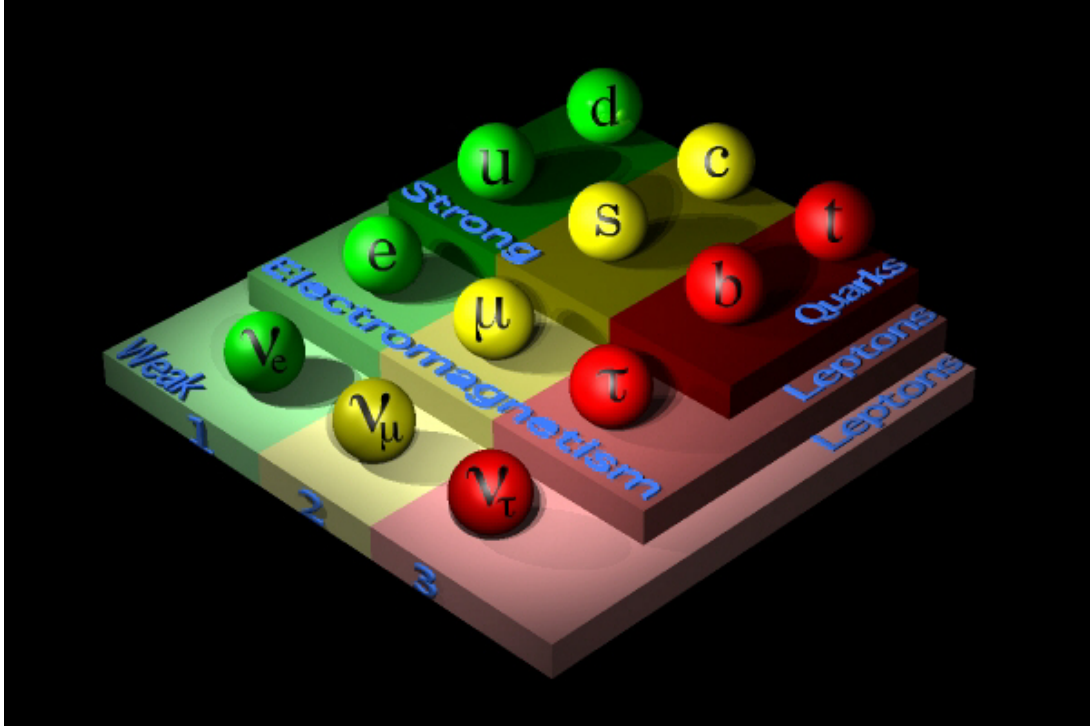


Figure 1.1: Grouping of quarks and leptons based upon the forces in which they participate [5].

mediate the interaction of appropriately charged particles with each of the fields.

Quantum chromodynamics is symmetric under rotations in $SU(3)$ space. The associated charge, color, may have one of three values referred to as red, blue, or green. Quarks possess a color and transform as triplet states; antiquarks have corresponding anticolor complements. The analogy to light is used because the sum of the three colors, or a color and its anticolor complement, is neutral or colorless similar to white light. Leptons are colorless and transform as singlet states. $SU(3)$ rotations, which turn one color into another, occur via the mediation of massless gauge bosons known as gluons. Each of the eight gluons has two colors: a red antigreen one will transform a green quark into a red one. Because gluons themselves have color charges, they can interact with one another.

A subtlety of the model is that the strength of the strong interaction, or coupling, increases rather than decreases with distance on small scales. The result is that when two

First Generation Fermions (Spin 1/2)				
Name	Symbol	Electric Charge	Color Charge	Mass
Electron	e^-	-1	0	0.511 MeV/ c^2
Positron	e^+	+1	0	0.511 MeV/ c^2
Electron-neutrino	ν_e	0	0	< 2 eV/ c^2
Electron-antineutrino	$\bar{\nu}_e$	0	0	< 2 eV/ c^2
Up quark	u	+2/3	r, g, b	1.5-3 MeV/ c^2
Antiup quark	\bar{u}	-2/3	$\bar{r}, \bar{g}, \bar{b}$	1.5-3 MeV/ c^2
Down quark	d	-1/3	r, g, b	3-7 MeV/ c^2
Antidown quark	\bar{d}	+1/3	$\bar{r}, \bar{g}, \bar{b}$	3-7 MeV/ c^2
Second Generation Fermions (Spin 1/2)				
Name	Symbol	Electric Charge	Color Charge	Mass
Muon	μ	-1	0	106 MeV/ c^2
Antimuon	$\bar{\mu}$	+1	0	106 MeV/ c^2
Muon-neutrino	ν_μ	0	0	< 2 eV/ c^2
Muon-antineutrino	$\bar{\nu}_\mu$	0	0	< 2 eV/ c^2
Charm quark	c	+2/3	r, g, b	1.25 GeV/ c^2
Anticharm quark	\bar{c}	-2/3	$\bar{r}, \bar{g}, \bar{b}$	1.25 GeV/ c^2
Strange quark	s	-1/3	r, g, b	95 MeV/ c^2
Antistrange quark	\bar{s}	+1/3	$\bar{r}, \bar{g}, \bar{b}$	95 MeV/ c^2
Third Generation Fermions (Spin 1/2)				
Name	Symbol	Electric Charge	Color Charge	Mass
Tau	τ	-1	0	1.8 GeV/ c^2
Antitau	$\bar{\tau}$	+1	0	1.8 GeV/ c^2
Tau-neutrino	ν_τ	0	0	< 2 eV/ c^2
Tau-antineutrino	$\bar{\nu}_\tau$	0	0	< 2 eV/ c^2
Top quark	t	+2/3	r, g, b	171 GeV/ c^2
Antitop quark	\bar{t}	-2/3	$\bar{r}, \bar{g}, \bar{b}$	171 GeV/ c^2
Bottom quark	b	-1/3	r, g, b	4.2 GeV/ c^2
Antibottom quark	\bar{b}	+1/3	$\bar{r}, \bar{g}, \bar{b}$	4.2 GeV/ c^2
Bosons (Spin 1)				
Name	Symbol	Electric Charge	Color Charge	Mass
Photon	γ	0	0	0
Neutral Boson	Z	0	0	91.188 GeV/ c^2
W^+ Boson	W^+	+1	0	80.404 GeV/ c^2
W^- Boson	W^-	-1	0	80.403 GeV/ c^2
Gluon	g	0	Octet	0

Table 1.1: Fundamental particles in the Standard Model [6]. The undiscovered Higgs boson is not listed. Note also that the masses of free quarks can only be indirectly inferred due to color confinement, and that neutrinos are massless in the Standard Model. Because they have been experimentally shown to have a small mass, neutrinos and antineutrinos may in fact be identical.

quarks are widely separated (compared to the size of a proton), the increase in energy produces a quark antiquark pair from the vacuum. These combine with the original quarks so that they are never individually isolated (color confinement). Two quark combinations, known as mesons, possess a colored quark and an antiquark of the same anticolor; the

pion is the most prominent example. Baryons are three quarks combinations, containing a red, blue, and green quark. This color confinement process allows only colorless hadrons (mesons or baryons), not individual quarks, to be directly observed. During a collision, rapid quark hadronization produces a group of neutrons, protons, and pions which travel away from the interaction in a narrow cone; this is known as a jet. The strong force is, nonetheless, very short ranged. The force is strong because it can bind adjacent quarks in the protons (two up quarks and a down quark) and neutrons (two down and an up) of a nucleus despite their electrostatic repulsion, but the strong force between nuclei in adjacent atoms is negligible.

Electroweak theory includes a $U(1)$ gauge symmetry from electromagnetism, giving rise to a single massless boson: the photon. The photon mediates the interaction of electrically charged particles, but is itself uncharged and thus does not self-interact. The weak force is appropriately named because its coupling strength is several orders of magnitude smaller than the other Standard Model forces. Parity is violated because it only interacts with particles of left-handed chirality, a property associated with the direction of a particle's spin relative to its motion. Pairs of left-handed quarks and leptons transform as doublets under the weak force, while right-handed particles transform as singlets (Table 1.2). A complication is that these quark doublets can mix because a state of definite mass is not a state of definite flavor. Thus a charm quark will generally decay to a strange quark, but occasionally it can also decay to a down quark. The Cabbibo-Kobayashi-Maskawa (CKM) matrix gives the magnitudes of these mixings [7].

The weak interaction is associated with $SU(2)$, but a complication arises because the three associated bosons are not observed to be massless. The solution is the addition of a symmetry between the electric and weak forces which mixes the two. The mass terms are produced via interaction with the resulting complex scalar field known as the

Fermion Type	First Generation	Second Generation	Third Generation
Quarks	$\begin{pmatrix} u \\ d \end{pmatrix}_L, u_R, d_R$	$\begin{pmatrix} c \\ s \end{pmatrix}_L, c_R, s_R$	$\begin{pmatrix} t \\ b \end{pmatrix}_L, t_R, b_R$
Leptons	$\begin{pmatrix} \nu_e \\ e \end{pmatrix}_L, e_R, (\nu_e)_R$	$\begin{pmatrix} \nu_\mu \\ \mu \end{pmatrix}_L, \mu_R, (\nu_\mu)_R$	$\begin{pmatrix} \nu_\tau \\ \tau \end{pmatrix}_L, \tau_R, (\nu_\tau)_R$

Table 1.2: Electroweak transformation properties of quarks and leptons. The subscripts L and R indicate the left- and right-handed helicities. The left-handed states transform as SU(2) doublets and the right-handed states as singlets.

Higgs field. This new symmetry is only apparent at high energy because the Higgs field's vacuum state is unstable, such that symmetry is spontaneously broken. The result is that the weak force has two massive electrically charged bosons, W^+ and W^- , and a massive neutral boson, Z . The discovery of these predicted bosons in 1983 stands as one of the greatest successes of the Standard Model. The Higgs field also introduces at least one Higgs boson, which has yet to be observed. Its discovery, expected at the Large Hadron Collider, may be the start of a breakthrough in the search for new physics, answering whether the Higgs mechanism involves additional bosons, whether there are additional symmetries, and explain why the vacuum expectation value is 10^{54} orders of magnitude smaller than expected from dimensional arguments.

Figure 1.2 summarizes the possible interactions mediated by the various types of bosons. Combining the contributions from quantum chromodynamics and electroweak theory, the

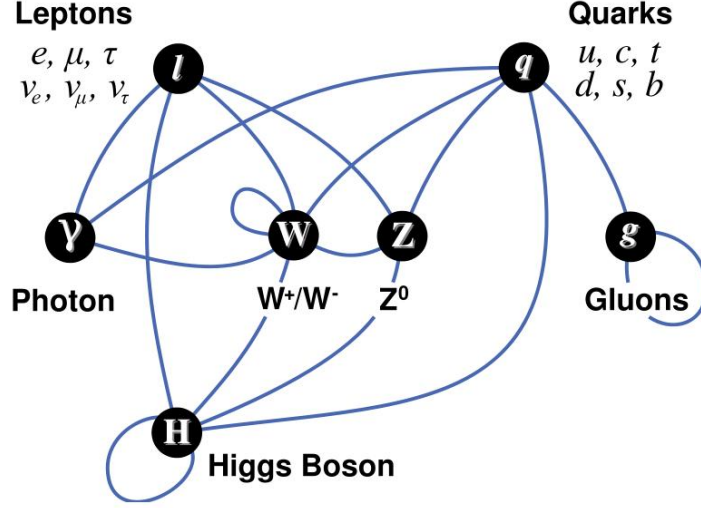


Figure 1.2: Graph of the Standard Model particles with lines illustrating the interactions mediated by each type of boson. From [8].

entire Standard Model Lagrangian can be expressed for fermions as:

$$\begin{aligned}
\mathcal{L} = & e \sum_{f=\nu,e,u,d} Q_f (\bar{f} \gamma^\mu f) A_\mu \\
& + \frac{g_2}{\cos \theta_w} \sum_{f=\nu,e,u,d} \{ (\bar{f}_L \gamma^\mu f_L) [T_f^3 - Q_f \sin^2 \theta_w] + (\bar{f}_R \gamma^\mu f_R) [-Q_f \sin^2 \theta_w] \} Z_\mu \\
& + \frac{g_2}{\sqrt{2}} \left[\{ (\bar{u}_L \gamma^\mu d_L) + (\bar{\nu}_L \gamma^\mu e_L) \} W_\mu^+ + \{ (\bar{d}_L \gamma^\mu u_L) + (\bar{e}_L \gamma^\mu \nu_L) \} W_\mu^- \right] \\
& + \frac{g_3}{2} \sum_{q=u,d} (\bar{q}_\alpha \gamma^\mu \lambda_{\alpha\beta}^\delta q_\beta) G_\mu^\delta, \tag{1.1}
\end{aligned}$$

This expression prescribes the interaction of all known matter on quantum scales with remarkable precision. It is a monumental achievement, but still a bit unwieldy for physicists' tastes. The model still contains nineteen arbitrary parameters: particle masses, flavor mixing angles, and coupling strengths. The recent observation of neutrino flavor oscillation [9] confirms that they do have mass, and thus the Standard Model must be modified. As mentioned earlier, the Higgs field is tied to the origin of mass; the discovery and study of particles in the Higgs sector will also shed light on possible new symmetries. Such symmetries may explain Standard Model properties such as why there are three

generations and matching groups of quarks and leptons. Some suspect that the Standard Model's complexities are simply low-energy manifestations of a single unified force. This is supported by the fact that the energy-dependent coupling strengths of all three quantum forces converge at around 10^{16} GeV. Eventually even a quantized theory of gravity may be incorporated, but progress thus far has been slow.

1.3 Searching for a New Particle

The classic particle physics experiment is the search for something new or unexpected. For a fundamental particle to have escaped detection thus far, it must either be difficult to produce in an accelerator, difficult to detect, or both. Particles can be difficult to produce if they have a small coupling to normal matter or if their mass is near the upper limit of the accelerator's reach. Detection is difficult for particles with small couplings, but their presence can still be inferred from the energy and momentum they carry away from an interaction, as is done for neutrinos. Detection is also difficult if particles are massive and quickly decay into ordinary quarks and leptons. Only by reconstructing all the outgoing secondary decay products in a large set of collisions (or events) can the parent particle be inferred. For masses well above the top quark, decay to any allowed combination of fermions is energetically possible, complicating the types of detector signal one must include in the search. Identifying a few unusual events in a sea of trillions of ordinary processes is the challenge which must be overcome to discover new phenomena.

As mentioned earlier, much of the evolution of particle physics has been based on the discovery of new patterns and symmetries. Most theoretical predictions for modifying or extending the Standard Model are based on plausible new symmetries which include additional particles. We begin our search for novel features in the data by narrowing our focus using some general assumptions about the new physics considered. We are interested

in the generic case that some Standard Model particles are mirrored at higher mass-scales, remaining undiscovered. This is analogous to the way the second and third generation particles are identical to the first generation but with larger masses. Neutrino studies have constrained the possibility of fourth generation leptons, while others have looked for fourth generation quarks. The CDF group at the University of Michigan determined there was an opportunity to further the search for massive new electroweak bosons, denoted W' and Z' . We have particular expertise and analysis tools suited to the study of decays involving top quarks. The Michigan group has recently completed a search for $Z' \rightarrow t\bar{t}$ [10]; a study of $W'^+ \rightarrow t\bar{b}$ and $W'^- \rightarrow \bar{t}b$ decays is complementary. This analysis describes the search for these signals, the sum of which we denote as $W' \rightarrow t\bar{b}$.

1.4 Luminosity, Cross-section, and Branching Ratio

It is useful at this point to introduce additional terminology. Cross-section (σ) refers to the likelihood of two particles interacting in a particular way. It is measured in units of area called barns ($1 \text{ b} = 10^{-24} \text{ cm}^2$) as an analogy to the classical scenario of an incident particle attempting to hit a target of a given size.

Most heavy particles can decay in several different ways. The branching ratio (BR) or branching fraction for a particular decay mode is the fraction of total particles expected to decay in this way. Thus the likelihood of a W boson decaying to an electron and neutrino can be expressed as the production cross-section $\sigma(p\bar{p} \rightarrow W)$ times the branching ratio $\text{BR}(W \rightarrow \ell\nu)$.

The instantaneous luminosity (\mathcal{L}) is a measure of the collision rate of the beams in an accelerator (sometimes called brightness) and depends on the transverse size of the beams and the number of particles they contain. Luminosity is measured in units of

inverse seconds and inverse barns, such that the instantaneous reaction rate is:

$$\frac{dN}{dt} = \sigma \cdot \mathcal{L}. \quad (1.2)$$

Integrating over a period of time gives the expected number of such interactions:

$$N = \int dN = \int \sigma \cdot \mathcal{L} dt. \quad (1.3)$$

Particle colliders typically run at a fixed energy such that σ does not significantly vary with time. To determine the interactions we actually expect to record, we must include a coefficient term for the overall efficiency of the detector for that process:

$$N_{Det} = \epsilon_{Det} \cdot \sigma \int \mathcal{L} dt. \quad (1.4)$$

The time-integrated luminosity, generally measured in inverse femtobarns (fb^{-1}), is sometimes simply called luminosity. This is how the size of a dataset can be expressed.

1.5 Features of a W'

A W' -like boson which decays via $t\bar{b}$ occurs in a variety of proposed models: as the excitation of the W boson in Kaluza-Klein extra dimensions [11], as the techni- ρ of technicolor theories [12], or as a bosonic partner in little Higgs scenarios [13]. The classic W' model is a simple extension of the Standard Model to the left-right symmetric group $SU(2)_L \times SU(2)_R \times U(1)$ [14], which has a right-handed charged boson W'_R with universal weak coupling strength and large mass. Currently the most sensitive W' searches use the $W' \rightarrow l\nu$ decay channel [15]. Searches in the $t\bar{b}$ [16] can probe models where the couplings are unknown or where the leptonic decays are suppressed. This channel complements general investigations of novel charged and neutral states coupling to the third generation, such as those involving decays to $t\bar{t}$ [10].

The Lagrangian describing the W' coupling to fermions can be written as [17]:

$$\mathcal{L} = \frac{g}{\sqrt{2}} \bar{f}_i \gamma_\mu (C_{ij}^R P_R + C_{ij}^L P_L) W' f_j + \text{h.c.}, \quad (1.5)$$

where $P_{L,R} = (1 \pm \gamma_5)/2$ are the projection operators, g is the gauge coupling, and the $C_{ij}^{L,R}$ are arbitrary couplings that differ for quarks and leptons. To restrict our search such that we can make a quantitative measurement, we must make some general assumptions. Our signal model assumes a W' with unknown mass, unspecified coupling strength to $t\bar{b}$, and purely right or left-handed chirality (W'_R or W'_L); this is referred to as a SM-like W' .

The W' is produced entirely by an s -channel process (Figure 1.3); contributions from the t and u channels are suppressed by the large W' mass. Like the Standard Model W boson, the W' decays nearly instantaneously to a quark-antiquark pair, or to a lepton and neutrino. This search is focused on the events that decay to $t\bar{b}$, which occur about a fourth of the time (Table 1.5). Our model is narrow in the sense that the width of the reconstructed mass peak is determined by detector resolution rather than the intrinsic width.

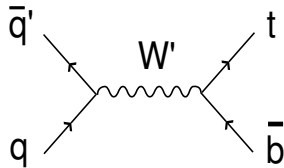


Figure 1.3: Dominant s -channel Feynman diagram for production of a positively charged W' and subsequent decay to $t\bar{b}$. This signal is the focus of this analysis.

Because the interference between the W boson and W'_L is model dependent and constrained to be very small, we neglect this term in our signal model. Studies have shown [18] that destructive interference for W'_L reduces the total $t\bar{b}$ cross-section across our mass interval, thus we only consider this model in the context of setting limits for W' with arbitrarily small coupling strength.

The right-handed W'_R case has a degeneracy based on whether decay to ν_R is allowed; we consider both possibilities. A right-handed model where ν_R decays are possible is identical to a left-handed model with negligible $W - W'_L$ interference: they have identical cross-sections and branching ratios. Properties that do not depend on helicity, such as mass, also have identical kinematics for both the right- and left-handed cases. A single simulation can be used to represent both. Chapter 4 will discuss simulated data in more detail. If the ν_R decay channel is closed, as it would be for a leptophobic W' or when suppressed due to $M_{W'} < M_{\nu_R}$, the branching ratio to $t\bar{b}$ increases. The two right-handed cases only differ by a simple scaling of the branching ratios. The theoretical prediction for these two cases [17] is shown in Table 1.5.

$M_{W'}$ (GeV/ c^2)	BR _{NLO} ($t\bar{b}$)		$\sigma \times \text{BR}$ (pb)		Expected Events	
	$M_{W'} < M_{\nu_R}$	$M_{W'} > M_{\nu_R}$	$M_{W'} < M_{\nu_R}$	$M_{W'} > M_{\nu_R}$	$M_{W'} < M_{\nu_R}$	$M_{W'} > M_{\nu_R}$
500	0.298	0.222	7.95	5.92	531	396
600	0.310	0.232	2.79	2.10	173	130
700	0.317	0.238	0.974	0.743	57.0	43.5
800	0.321	0.241	0.337	0.262	18.4	14.3
900	0.324	0.244	0.116	0.093	6.08	4.88

Table 1.3: Predictions for $\sigma \times \text{BR}(W' \rightarrow t\bar{b})$ and expected number of events in 1.9 fb^{-1} using our selection, as a function of W' mass.

In summary, this analysis is a search for a narrow SM-like W' with purely left-handed or right-handed couplings, and no interference. This model is sufficiently general, however, to allow us to quantify the significance of any narrow excess in the $t\bar{b}$ distribution from 350 to 950 GeV/ c^2 .

1.6 W' Search Methodology and $t\bar{b}$ Mass

The kinematics of individual decays do not uniquely identify the underlying source; this is due to mismeasurement and the probabilistic outcome of single quantum events. Large ensembles of similar events must be selected and compared to Standard Model

prediction to measure the statistical significance of a novel signal. The first step, discussed in Chapter 3, is to use various criteria to select potential W' events while eliminating as many background events as possible. The candidate signal events must then be modeled. Chapter 4 discusses modeling of the Standard Model processes that appear as background in the data, as well as how their relative contributions are determined. Chapter 5 discusses the W' model used for our signal.

High-fidelity modeling is the key to the success of this analysis. We cannot simply count the events: we do not know our expected background rates well enough to measure such a small signal contribution. Instead we must look for changes in the resulting kinematic distributions. The only property with sufficient discriminating power to isolate our few signal events is the $t\bar{b}$ mass ($M_{t\bar{b}}$), discussed in Chapter 5. Most background processes involve a Standard Model W boson with a much smaller mass ($80.403 \text{ GeV}/c^2$) than the W' mass range to which we are sensitive: $300 \text{ GeV}/c^2$ to $950 \text{ GeV}/c^2$. This high-mass region of the $t\bar{b}$ distribution, or tail, is sparsely populated in data; correct modeling of the small background there will impact the amount of measured signal.

Chapter 5 details the numerical method we use to quantify the presence or absence of signal by comparing signal and background predictions to the $M_{t\bar{b}}$ distribution we observe in data. Chapter 6 focuses on sources of uncertainty in this measurement and how they are quantified.

The last chapter quotes the result of our measurement of $M_{t\bar{b}}$. We begin by setting 95% confidence level (C.L.) upper limits on the $W' \rightarrow t\bar{b}$ cross-section for a SM-like W' . We then compare these upper limits to theoretical predictions for a SM-like W'_L and W'_R . We then set a lower bound on the W' mass for such a model. Finally we consider the more general case of a W' -like decay with unknown coupling. We place 95% C.L. upper limits on the coupling strength for such a $t\bar{b}$ resonance.

CHAPTER 2

Fermilab and the CDF Experiment

The data in this analysis were recorded by the Collider Detector at Fermilab (CDF) from 2001 to 2007. This is a massive experiment by any measure: size (3 stories tall and 5000 tons), personnel (600 physicists), or scientific output (now 50 publications/year). The particle collisions it records are produced by the four-mile circumference Tevatron, which in turn relies on the entire Fermilab complex to operate. The impressive scope of this facility makes possible the exploration of the particle physics frontier.

2.1 Fermilab and the Tevatron

The Tevatron is a proton-antiproton ($p\bar{p}$) collider located at the Fermi National Accelerator Lab, or Fermilab, near Chicago, Illinois. Fermilab is the largest particle physics laboratory in the United States, and 2009 is its final year as host to the highest-energy particle collider in the world. Fermilab is the only single purpose facility in Department of Energy's national laboratory system and the only one dedicated to the field of high-energy physics.

Fermilab was founded in 1967 on a site of 6800 acres of tall-grass prairie. The Tevatron was completed in 1983 as the world's first superconducting synchrotron. The use of superconducting magnets allowed greater magnetic fields to be achieved at lower cost;

they require no power to maintain their magnetic field. Including the penalty of keeping the magnets refrigerated to 3.8 K, the Tevatron uses only a third of the electricity required by conventional magnets. Initially used to accelerate proton beams into a dense target, the Tevatron was soon made into a proton-antiproton collider. In 1985 the first of two massive detectors, CDF, recorded the first collisions; the DØ experiment was completed in 1992. In 1995 both detector groups concurrently announced the discovery of the top quark. The arduous search had taken decades, but the Standard Model was now firmly established; the groups could now focus on better understanding the quark interactions and looking for new physics phenomena.

The entire facility underwent a major upgrade from 1995-2001. The energy of the Tevatron was increased ten percent, and with the addition of a new injector, the luminosity could be increased by a factor of twenty. The detectors were upgraded to handle the increased data rate and to improve particle tracking and energy resolution. The Tevatron has run continually since 2001, excluding periodic maintenance. This post-upgrade data-taking period is referred to as Run II.

2.2 Accelerator Complex

The Tevatron is only the last of a series of seven accelerators comprising the majority of the Fermilab complex [19], shown in Figure 2.1. The protons begin as nuclei of hydrogen atoms in a bottle of compressed molecular hydrogen gas. The application of a high-voltage gradient disassociates the molecules into plasma, some of which forms negative hydrogen ions comprised of a proton and two electrons.

The first stage of acceleration begins inside one of the two large Cockcroft-Walton devices. Voltage ladders boost the ions to 750 keV. They are then grouped into bunches and enter the 500 foot linear accelerator (linac). Radio waves matched to the size and

FERMILAB'S ACCELERATOR CHAIN

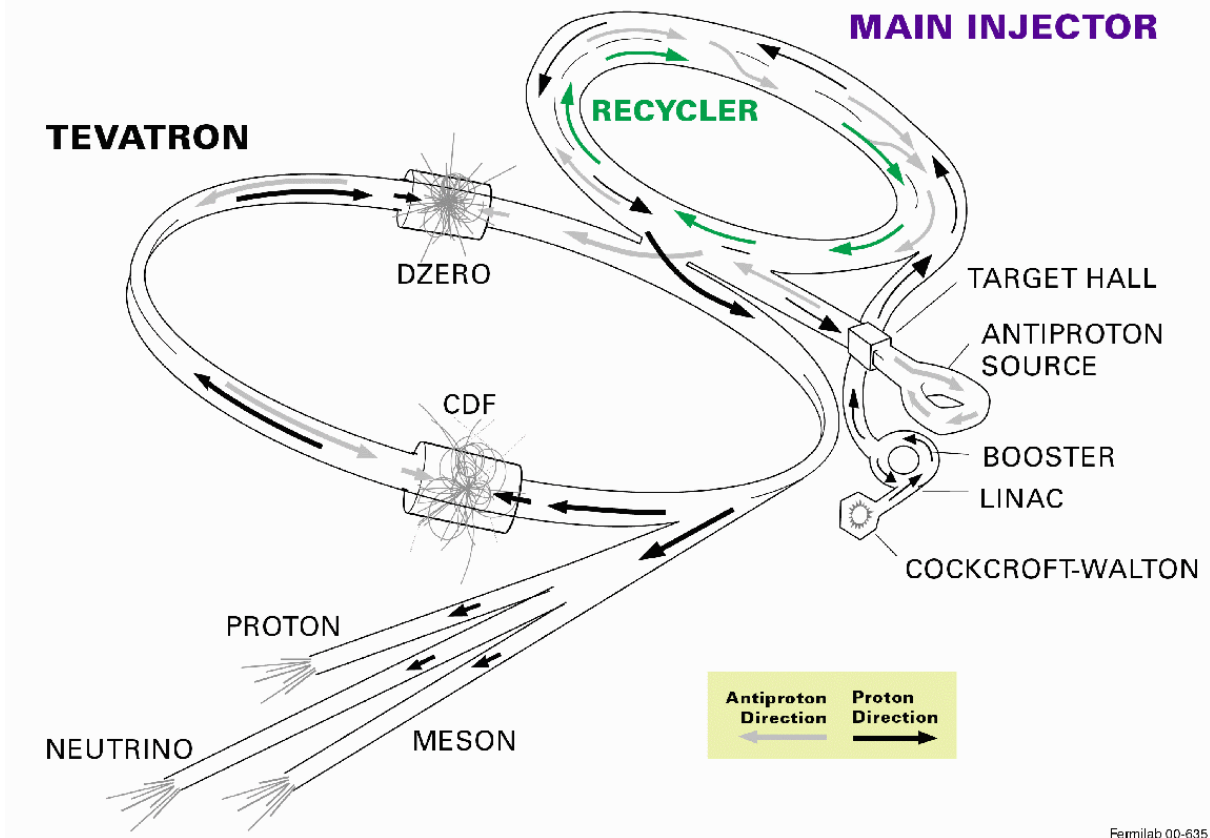


Figure 2.1: An overview of the Fermilab accelerator complex.

timing of the bunches push and pull the ions along a string of copper cavities. The spacing of the cavities increases along the linac to cancel the Lorentz contraction apparent in the reference frame of the accelerating ions. They leave the linac at 400 MeV and pass through a thin strip of foil as they reach the accelerator known as the Booster. The foil removes the two electrons, and a magnet steers the now bare positively-charged protons into the machine. The 500 foot diameter Booster is the first of a series of circular accelerators known as synchrotrons.

A synchrotron consists of a circular beampipe surrounded by dipole electromagnets

to bend the particles around the circuit. Straight sections contain radio-frequency (RF) cavities in which the particles are accelerated to higher energy. The strength of the magnetic field is synchronized with the increasing speed of the particles such that their path remains fixed inside the beampipe. Since protons within each bunch spread out over time due to electrostatic repulsion, a series of alternating quadrupole magnets focus the bunches in the vertical or horizontal directions. As a bunch circulates around, a single RF section can accelerate it repeatedly, allowing synchrotrons to be far more compact than a linear accelerator achieving the same energy.

A quarter of the 8 GeV bunches leave the Booster and enter the main injector for use in the Tevatron. The other seventy-five percent are sent to a target to produce pions, and eventually neutrinos, for the Miniboone neutrino experiment. The main injector accelerates the protons to 120 GeV and sends them in a pulse either to the antiproton target or the MINOS neutrino experiment. The antiproton target is a specially shaped nickel disk which produces a shower of particles when hit by the energetic pulse every 1.5s. This shower is focused into a column by a lithium lens, and a bending magnet separates out the negatively-charged antiprotons, which have an average energy of 8 GeV. For every million incident protons, only about twenty antiprotons are collected.

The filtered antiprotons then enter an 8 GeV accelerator called the Debuncher. The antiprotons from each pulse are grouped in time but have a spread of momenta. Those which are faster or slower than average arrive at the accelerator cavities slightly out of phase with the RF waves, and thus are shepherded to match the RF timing. This effectively trades the grouping in time for grouping in momentum space. Thus they leave with uniform energy but are no longer in a bunch.

The antiprotons next pass to the Accumulator, which resides in the same tunnel. Here the antiprotons have the transverse components of their momentum reduced, a process

known as cooling for the similarity to thermal oscillations. The Accumulator uses a stochastic cooling technique [20] by which minute deviations in the antiproton orbits detected on one side of the ring are cancelled by compensating magnets on the opposite side. The signals from the pickups to the correcting quadrupoles travel directly across the ring so as to arrive before the circuitously traveling antiprotons. As the antiprotons aggregate over several hours, they are grouped back into bunches which can then be stored in the Recycler.

The Recycler is a fixed energy storage ring using permanent magnet technology, and is housed in the same tunnel as the Main Injector. The Recycler was originally designed to reuse antiprotons not expended in the Tevatron. It was later repurposed for antiproton storage in order to increase the efficiency of the antiproton complex. After 20-30 hours of collection, a sufficient number of antiprotons are available to load into the Tevatron.

The use of antiprotons for collisions reduced accelerator cost. Because they are oppositely charged and circulate in opposite directions, both the protons and antiprotons can be steered by the same expensive superconducting magnets. A slight helical offset ensures the beams do not collide except when intended. The penalty is the difficulty of producing and storing antiprotons, a severe constraint on the rate at which the Tevatron can be reloaded; this limits overall integrated luminosity.

The Tevatron's one kilometer radius, combined with its use of 53.1 MHz RF for acceleration, translates to a design 1113 wavelengths in circumference. Since it is the radio waves which create and maintain the bunch spacing, there are 1113 differently timed slots or buckets in which bunches can travel. At the start of a collision run, the main injector transfers 36 bunches of 150 GeV protons to the Tevatron, then 36 bunches of antiprotons from the Recycler, orbiting in the opposite direction. Because they are easy to obtain, each proton bunch (about 10^{13} protons) is made as large as possible to increase the colli-

sion rate. The practical limit due to the Tevatron impedance is about $8\times$ larger than the antiproton bunches. The bunches are arranged in three groups of twelve, called trains, with twenty empty buckets between bunches and larger spacing between trains. This large gap allows the Tevatron the time to abort the beam if it becomes unstable. The abort switch magnet (kicker) needs about $2.8\mu\text{s}$ to reach full strength before the bunches arrive in order to direct them into the concrete dump block.

Once the Tevatron is loaded, it accelerates each beam from 150 GeV to 980 GeV in about 90 s, the low β quadrupole magnets on each side of the two detectors ramp to full power to reduce the transverse beam size to two microns, and stray particles are removed from the outer edges of the beam by inserting large steel blocks (collimators) into their path. Collisions at CDF and $D\bar{O}$ are initiated by electrostatic separators that rotate the offset proton and antiproton beams to collide head on. The detectors surround the approximately two meter long sections of beampipe where most of the inelastic collisions occur. Even with trillions of particles focused into such a narrow area, the bunches remain mostly empty space and can pass through one another like two swarms of bees. On average, one to ten collisions occur with each bunch crossing, and the Tevatron can run nearly 30 hours before it needs to be reloaded

2.3 CDF Detector

CDF is a cylindrically-symmetric general purpose detector utilizing a solenoidal magnet [21]. It can identify the hundreds of secondary particles produced in each collision via precision measurement of the charge, momentum, and energy deposition (calorimetry). CDF is a layered combination of several detector systems (Figure 2.2), each optimized for a particular particle or crucial measurement. The innermost detector is the silicon tracking system, enclosed by the central outer tracker. These are both inside the 1.4

The superconducting solenoidal magnet, around which are mounted the electromagnetic and hadronic calorimeter towers. The outermost detector is the muon detection system. The central portion of CDF is referred to as the central barrel and the separate end cap systems are referred to as the plugs.

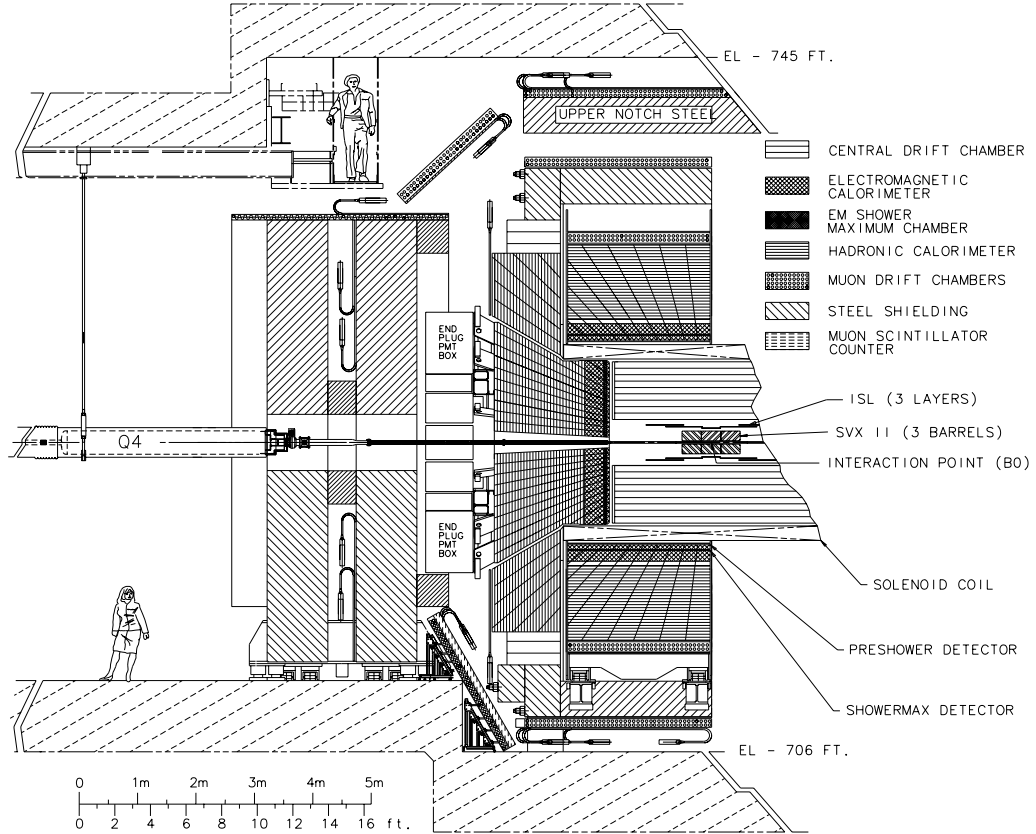


Figure 2.2: Cutaway view of CDF.

2.3.1 CDF Coordinate System

A right-handed coordinate system is used to describe collisions in the detector: the origin lies at the center of CDF, the z -axis points in the direction of the proton beam, azimuthal angle ϕ is measured from direction away from the center of the Tevatron, and polar angle θ is measured from the z -axis. However, the lab frame is not the same as the collision's center of mass frame. Even though the proton and antiproton have the same

momentum, it is the quarks or gluons (partons) inside which actually collide and they do not partition that momentum equally. Thus the center-of-mass frame has some boost along the z -axis. A more natural polar coordinate in the circumstance is pseudo-rapidity, defined as:

$$\eta = -\ln\left(\tan\frac{\theta}{2}\right). \quad (2.1)$$

The convenience is that the density of final state particles is approximately uniform in units of η . This is because the η coordinate is invariant under boosts in the z direction, and thus is the same in the center-of-mass frame and in the lab frame. This variable also provides a useful measure of the angular separation between objects:

$$\Delta R = \sqrt{(\Delta\phi)^2 + (\Delta\eta)^2}. \quad (2.2)$$

2.3.2 Silicon Tracking System

The innermost detector system is the silicon tracking system, Figure 2.3. This system is critical to the identification of bottom quarks produced by top-quark decay. Bottom quarks quickly form hadrons with lifetimes limited by that of the b -quark: 1.568×10^{-12} s [6]. These hadrons can travel a few mm from the interaction point before decaying into a number of other hadrons. By providing track impact parameter resolution of approximately 30 microns, the silicon system allows the displaced track vertex to be reconstructed, identifying the presence of a bottom quark. This process is called b -tagging and was first pioneered at CDF.

The silicon system comprises overlapping silicon microstrip detectors, arranged in concentric cylindrical layers. The microstrips are arranged in pairs called ladders with integrated electronic readout chips and cooling channels. The strips are double-sided: each side has a silicon crystal etched with lines of p - n junctions to which a reverse voltage bias is applied. Because the harsh radiation environment so close to the beam gradually

CDF Tracking Volume

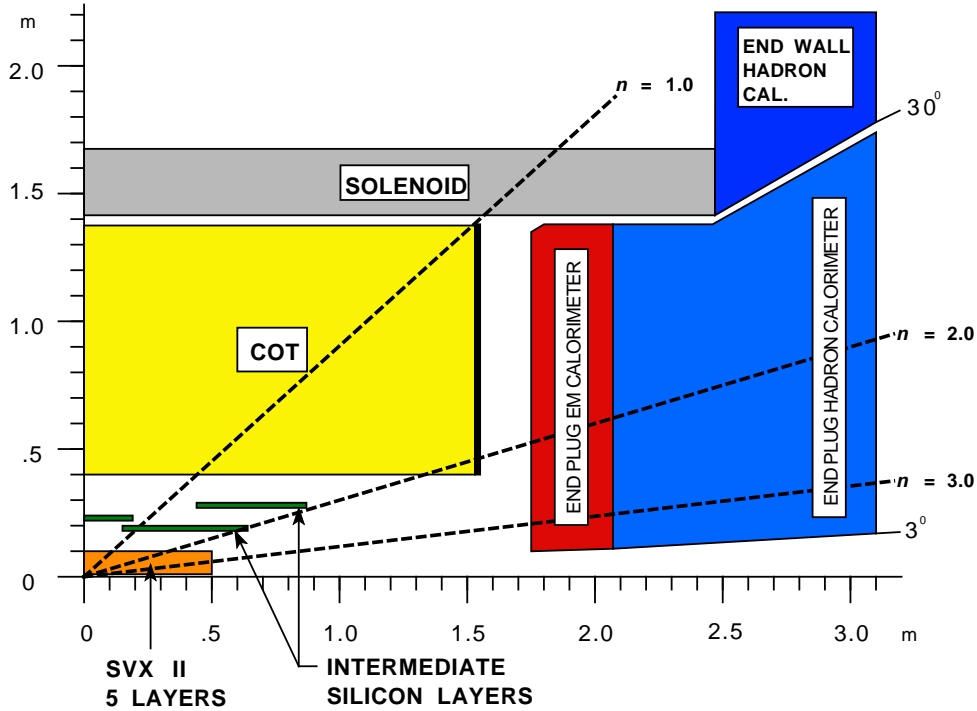


Figure 2.3: Cross-section view of the CDF tracking and calorimeter systems.

degrades the silicon crystals, these ladders are only energized when the beam is stable and tightly confined. Charged particles passing through the silicon crystal cause ionization; the freed electrons are captured in the junction, causing a current pulse. The junctions on one side are aligned to provide position measurement in the azimuthal plane, while those on the other side are offset either 90° or 1.25° , so as to provide excellent overall η and z -position tracking.

The innermost layer of the silicon system, Layer 00, is single-sided and attached to a carbon-fiber framework bonded directly onto the beampipe (1.3 cm radius). It is surrounded by the five layers of the silicon vertex detector (SVX II). Further out, at a 29 cm radius, are the three intermediate silicon layers (ISL). They improve tracking at high η by covering a greater range along the z -axis.

2.3.3 Central Outer Tracker

The silicon tracking system sits entirely inside the central outer tracker (COT). The COT is an open cell drift chamber using a mix of argon and ethane as the ionizing medium. The COT contains eight concentric layers of tracking cells. Each cell contains a linear arrangement of 29 wires which span the length of the chamber. Wires at 2000 V and at 3000 V are arranged in an alternating pattern, with two additional wires at the end serving to ground the potential.

When a charged particle passes through the gas, many atoms along the path are ionized. The nearly massless free electrons quickly drift in the high-voltage field to the 3000 V wires, causing an avalanche of secondary ionization. By measuring the drift time and knowing the drift velocity in the gas, the radial distance to the original particle's track can be determined to within approximately 180 microns. Orienting half of the cells at a different angle allows track locations to be fully determined in three-dimensions.

The chamber is enclosed inside a 1.4 T superconducting solenoidal magnet, curving tracks in the azimuthal plane according to the particle's transverse momentum (P_T). By combining track hits across dozens of COT cells and performing a fit to a continuous helix, the COT can be used to measure the track P_T with an uncertainty of $\frac{\delta P_T}{P_T} = 0.0015 P_T$.

2.3.4 Electromagnetic Calorimeter and ShowerMax Detector

Surrounding the magnet are the calorimeters which measure energy deposition. The central electromagnetic calorimeters (CEM) cover $|\eta| < 1.1$ and the plug calorimeters (PEM) cover $1.3 < |\eta| < 3.6$. An electromagnetic calorimeter is optimized to measure the energy of electrons and photons. It comprises 23 layers of lead and scintillator: plastic doped to give off light when charged particles pass through. Each layer has 4.5 mm of lead and 4.0 mm of scintillator. As electrons pass through a dense medium, they lose

energy when they deflect from the electric field of atomic nucleus by emitting a photon. The photons can spit into an electron-positron pair, which radiate more photons. This combination of processes results in a shower of electrons and photons (bremsstrahlung), each of which has a diminishing fraction of the initial energy as the shower grows. Eventually each particle has so little energy that it can lose the remainder by ionizing an atom before reaching the nucleus, terminating the shower. The calorimeters contain 21 radiation lengths of lead, enough to reduce an average particle to $\frac{1}{e^{21}}$ of its initial energy.

Because the energy is partitioned nearly evenly among the particles in the bremsstrahlung shower, and each particle produces a similar amount of scintillation light, the total energy of the showers is proportional to the light produced. The calorimeter simply counts the total light output from the various scintillator layers. The light from a shower is collected at the edge of each layer, shifted in frequency, and transmitted along a light pipe to a photomultiplier tube at the top. The uncertainty in the measured transverse energy E_T is given by $\frac{\delta E_T}{E_T} = 0.14/\sqrt{E_T}$ in the CEM.

Embedded six radiation lengths inside the CEM is the Central EM ShowerMax system (CES); similarly the PEM has an embedded Plug EM ShowerMax system (PES). These consist of a series of parallel proportional wire chambers with capacitively coupled scintillator strips running the other direction. This highly segmented system images the transverse profile of the shower to provide better electron and photon identification, and to improve the matching of showers to tracks in the COT.

2.3.5 Hadronic Calorimeter

The hadronic calorimeters enclose the electromagnetic calorimeters and are similar in design. They consist of a stack of 23 two-inch iron plates interleaved with 6 mm layers of scintillator, suited to stopping the pions, neutrons, and protons that comprise a jet.

These particles lose energy by nuclear interactions within the iron, again producing a shower of daughter particles, in this case pions and nucleons. This calorimeter system is much larger because the cross-section for nuclear interaction is much smaller. The central hadronic calorimeter (CHA) provides 4.5 nuclear absorption lengths of iron, while the plug hadronic calorimeter (PHA) provides 7.0 absorption lengths. Because of the larger and more varied nature of these showers, the energy resolution ($0.50/\sqrt{E_T}$ in the CHA) is much poorer than in the electromagnetic calorimeters and is one of the largest sources of systematic uncertainty in our measurement. Chapter 3 discusses how the energy deposits in different calorimeter sections are grouped according to jet.

The flow of various types of particles through the detectors is summarized in Figure 2.4.

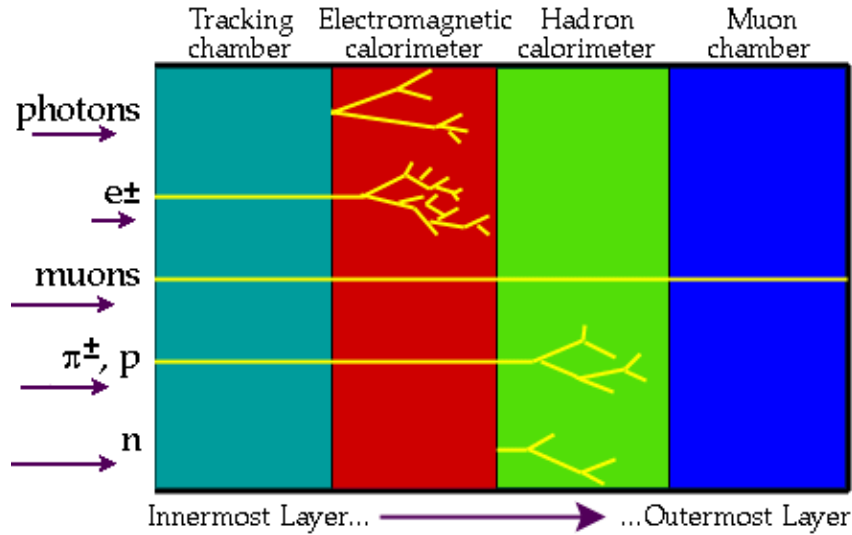


Figure 2.4: Penetration of various particles through the detector layers.

2.3.6 Muon Chambers

The outermost detection system is the muon chambers. Because the bremsstrahlung process is inversely proportional to the square of the mass and muons are $200\times$ more massive than electrons, they have a very small likelihood of interacting with material; they can easily pass through the entire detector unimpeded. Additional slabs of steel sur-

rounding CDF stop hadrons which occasionally penetrate the calorimeters. This ensures that nearly all particles which reach the externally mounted muon chambers are actually muons.

Because of the non-uniform shape of CDF, several sets of chambers are needed to provide robust angular coverage. The box-shaped Central MUon Detector (CMU) and Central Muon uPgrade (CMP) cover the central region of $|\eta| < 0.6$, the Central Muon eXtension (CMX) is mounted on arches in each corner and covers from $0.6 < |\eta| < 1.0$, and the Barrel Muon Upgrade (BMU) covers the plug from $1.0 < |\eta| < 1.5$. Figure 2.5 shows the location of these systems; some areas are not covered due to penetrations of cryogenic lines and cabling to the inner detectors.

Each muon chamber consists of four layers of proportional drift tubes, covered with an outer layer of scintillator. These chambers operate similarly to the cells of the COT and also contain argon-ethane. The pulse of scintillator light from a passing muon is used to start the measurement of the drift time, as the ions liberated in the gas tubes travel toward the high-voltage wires running down the center. By slightly offsetting two of the four layers, the track position can be determined unambiguously.

2.3.7 Neutrino Detection

Neutrinos pass through the entire detector like muons, but leave no trace of their presence other than the energy and momentum they remove from the system. Because the proton and antiprotons collide head on, there is no initial momentum in the transverse direction. Because CDF provides nearly total azimuthal coverage, we can detect the transverse momentum of nearly all the other particles. An imbalance larger than the experimental uncertainty is likely due to the presence of one or more neutrinos (or undiscovered noninteracting particle). Because the particle masses are negligible relative

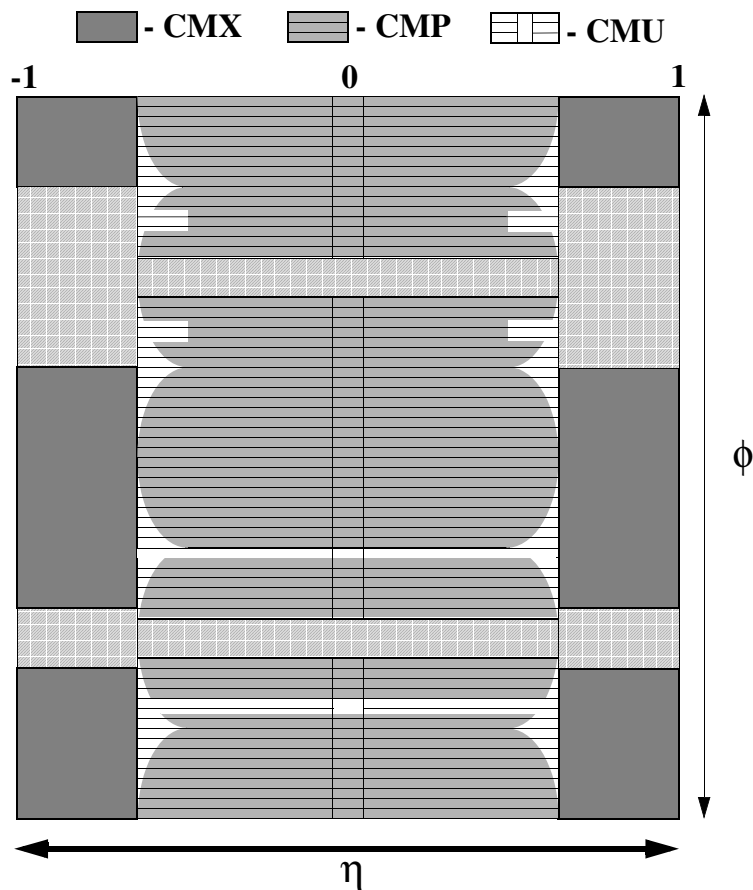


Figure 2.5: Angular coverage of each set of muon chambers. The BMU is not shown.

to the momenta involved, this large missing transverse momentum is actually measured as missing transverse energy (\cancel{E}_T), discussed in detail in Chapter 3.

2.4 CDF Data Acquisition System

When originally designed, there was consideration of separating the Tevatron bunches by seven buckets (132 ns) rather than the actual 21 bucket (396 ns) spacing. This spacing determines the frequency of collisions, and thus the rate at which the data acquisition system (DAQ) must determine whether to record events. The DAQ was designed to sift

through 95% of those events before becoming saturated. This is a challenge when there are 750k channels to be read out, which translates to a dataflow of 20 TB/s! Also 132 ns is barely enough time for light to travel from the detector to the computers upstairs, so a buffer is required to provide latency in the decision-making. Since it is not feasible to record every possible event, a three stage trigger system (Figure 2.6) was designed to select only the 75 or so most interesting of the two million collisions occurring every second.

The first selection stage, Level 1, has a hardware buffer to store information for 42 consecutive bunch crossings. This delay allows the ions in the COT and muon drift tubes to be collected and read out. Several operations are performed in parallel by the hardware: helical tracks are fit to hits in the COT, extrapolated COT tracks are matched to tracks in the muon chambers, and the sum of the transverse energy deposited in the calorimeters is calculated. The end results are compared with the selection criteria specified for interesting events (trigger tables), and a global decision is made whether to continue processing the event. The Level 1 acceptance rate is set to 50 kHz.

The Level 2 stage allows an event to be stored in one of four parallel buffers. During this time the silicon tracking system reconstructs the impact parameter of the tracks to see whether there are potentially any b -tags, the calorimeter boards identify electrons and photons, and any showers in the hadronic calorimeters are reconstructed into jets. The hardware uses a more sophisticated set of programmable decision criteria to further reduce the acceptance rate to 700 Hz.

The Level 3 trigger decision is made by sending event information to one processor of several hundred dual core Linux computers. The computer fully reconstructs the event using all the relevant detector channels and takes up to one second to render a final verdict. This trigger has a 75 Hz accept rate. The trigger requirements are relaxed with decreasing instantaneous luminosity, such that CDF always records data near its maximum rate.

Dataflow of CDF "Deadtimeless" Trigger and DAQ

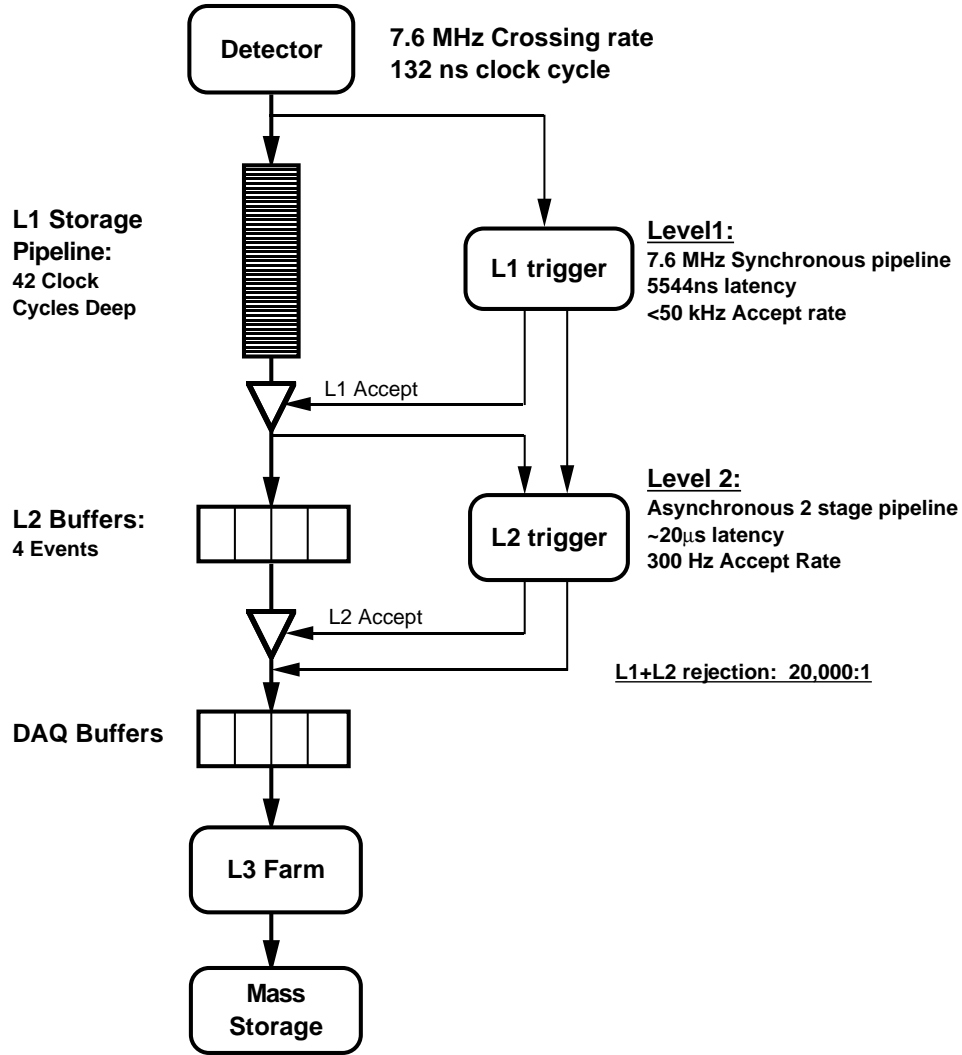


Figure 2.6: Schematic of the CDF data acquisition system.

Accepted events are temporarily written to a hard disk, then copied to more cost-effective magnetic tape in the offsite computing center. All the most recent data is processed to apply final calibrations for time-sensitive variables such as beam alignment, detector alignment, component aging, and operational detector configuration. This of-line processing, including detailed validation, is required before the data is available for

analysis. In addition, the different physics groups at CDF apply further processing in order to store the event information in a compact and conveniently organized framework for a given physics study.

CHAPTER 3

Event Selection

3.1 W' Decay Signature

As discussed in Chapter 1, this analysis is focused on $W' \rightarrow t\bar{b}$. The top quark decays in 10^{-25} s via $t \rightarrow Wb$ [6]. This W boson also quickly decays: $\text{BR}(q\bar{q}) = 68\%$ and $\text{BR}(\ell\nu) = 32\%$. Thus the W' final state (Figure 3.1) appears in the detector either as hadronic jets from four quarks (hadronic case), or as two jets from the b -quarks, a lepton, and missing energy from a neutrino (leptonic case). The all hadronic case, though dominant, is very difficult to distinguish from the large multi-jet background. Frequent strong interactions produce $b\bar{b}$ pairs, often with an additional quark-antiquark pair, appearing in the detector as a collection of jets masking any W' contribution. Instead we focus on the leptonic final state which has a less prodigious Standard Model background. This is because electroweak processes at the Tevatron have smaller cross-sections than QCD (Figure 3.2), thus fewer background events contain a lepton and neutrino in addition to jets. Thus we search for $W' \rightarrow t\bar{b} \rightarrow \ell\nu b\bar{b}$.

We must consider the special leptonic case of $W \rightarrow \tau\nu$. Tau leptons, like the top quark, decay too quickly (10^{-13} s) to be directly observed [6]. The tau may decay to $q\bar{q}\nu_\tau$, $\mu\nu_\mu\nu_\tau$, or $e\nu_e\nu_\tau$. We again discard the hadronic case. The leptonic final state is nearly unchanged: instead of a single neutrino, the tau decay produces two more. The consequence is that

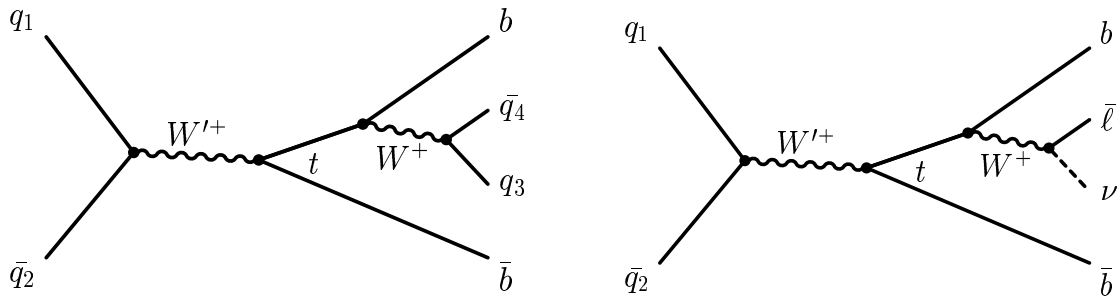


Figure 3.1: $W' \rightarrow t\bar{b}$ Feynman diagrams for hadronic decay (left) and for leptonic decay (right).

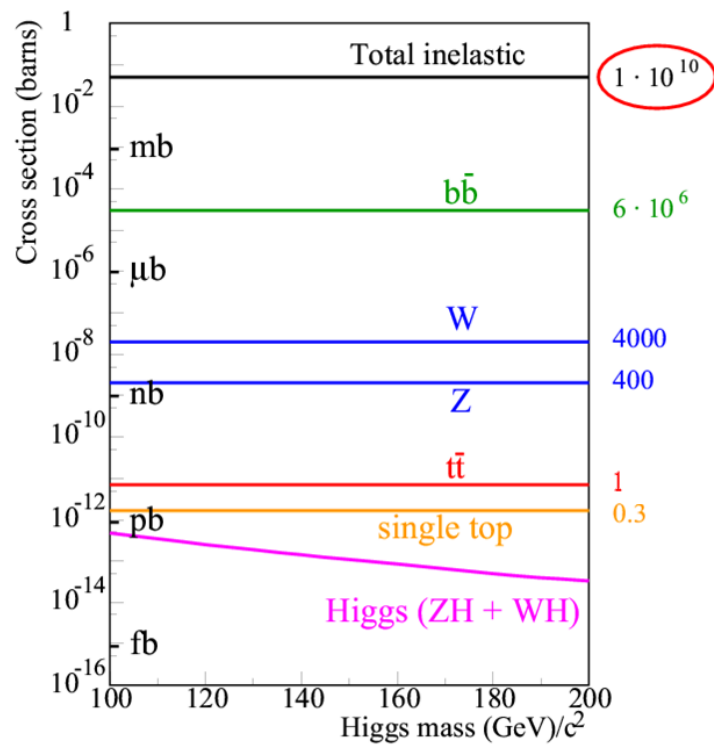


Figure 3.2: Total Tevatron production cross-section of various background processes. The $W' \rightarrow t\bar{b}$ cross-section is expected to be smaller than that shown for single-top production.

we mis-reconstruct these events by assuming the \cancel{E}_T is from one neutrino rather than three.

The two b -quarks in the leptonic final state are not the only source of jets in the signal.

Gluon radiation from the incoming or outgoing partons, along with other detector effects, frequently causes an additional jet. Thus we consider signal events with two or three jets, in addition to an electron or muon and \cancel{E}_T .

QCD processes can produce an electron via semi-leptonic decay of a b -mesons, or a muon via pion decay. These leptons appear close to the jet in which they were produced, thus we can exclude them if we require the leptons to be well isolated from jets. Similarly, detector mismeasurement results in all events having a slightly non-zero \cancel{E}_T , so we only include events with significantly large \cancel{E}_T , increasing our neutrino detection efficiency. These are just two examples of the many event requirements, or cuts, necessary to preserve signal while efficiently cutting background. This is important when the W' cross-section is at least $10^6 \times$ smaller than the total inelastic cross-section.

To summarize, we search for $W' \rightarrow t\bar{b}$ by selecting leptonic events with two or three high- P_T jets, a high- P_T electron or muon, and large \cancel{E}_T ; these are referred to as the $W+2$ jet and $W+3$ jet channels. The purity of these channels serves as the basis for many top analyses, and allows us to use the same selection and background treatments honed in the recent single top searches [22].

3.2 Triggers

Event selection begins online, in real time, as the detector is triggered and read out. The online trigger requirements generally characterize interesting events as having large quantities of transverse energy deposited as leptons, photons, and/or jets, often with large \cancel{E}_T . Datasets are created that contain all the events passing a particular trigger. The datasets containing triggers useful for $W+2$ and $W+3$ jet analysis are called `bhel`, `bpe1`, `bhmu`, and `emet`.

The `bhel` dataset contains events passing the high- P_T CEM trigger, which is optimized

to identify electrons in the central calorimeter. This trigger requires:

- A cluster of energy in the CEM with $E_T \geq 18 \text{ GeV}$ (Ensures the energy deposited is well above noise)
- A COT track with $P_T \geq 8 \text{ GeV}/c$ is matched to the cluster (Ensures the particle came from the interaction and is not a photon)
- $E_{Had}/E_{EM} \leq 0.125$ (The small hadronic to electromagnetic energy fraction ensures the source was not likely a hadron)
- A cut on the lateral shower profile (Ensures the shower collimation is consistent with electron beam data)

The `bpe1` dataset contains events passing the MET+PEM20 trigger, which is optimized to identify electrons in the detector plug. This trigger requires:

- A cluster of energy in the PEM with $E_T \geq 20 \text{ GeV}$
- $E_{Had}/E_{EM} \leq 0.125$
- $\cancel{E}_T \geq 15 \text{ GeV}$ (Because the PEM is at large η where COT tracking is poor, this trigger reduces the background rate with a \cancel{E}_T requirement rather than a track requirement)

The `bhmu` dataset contains events passing the high- P_T CMUP and CMX triggers, which are optimized to identify central muons. The CMUP trigger requires:

- A muon track (stub) matched in both the CMU and CMP detectors
- A COT track with $P_T \geq 18 \text{ GeV}/c$ is matched to the muon stubs (Ensures both detector systems identified the same particle)
- The extrapolated track in the transverse plane is within 10 cm of the CMU stub and within 30 cm for the CMP stub (Ensures false track rejection)

The CMX trigger requirements are analogous, except the stubs occur only in the CMX detector.

The `emet` dataset contains events passing the MET+2JET trigger, which is not designed for lepton selection. We select muon from these events using offline selection. This trigger requires:

- $\cancel{E}_T \geq 35 \text{ GeV}$
- Two jets with $E_T \geq 25 \text{ GeV}$

3.3 Lepton Selection

After the datasets have their final calibrations applied, additional cuts are made offline which precisely define whether an object in the detector is classified as an electron or muon. These more stringent cuts ensure that only the unambiguous leptons are used, further reducing contamination from background sources and false signals. There are two general categories: “tight” leptons must meet very selective criteria designed to maximize purity, and “loose” leptons meet less restrictive requirements, trading increased acceptance for reduced purity.

3.3.1 Tight Central Electron Selection

Tight electrons must have an EM calorimeter cluster with $E_T \geq 20 \text{ GeV}$ and COT track $P_T \geq 10 \text{ GeV}/c$. For $P_T \leq 50 \text{ GeV}/c$, the COT track must have $E/P \leq 2.0$ to ensure consistency with calorimetry. Quality tracking resolution in both the longitudinal and transverse dimensions is ensured by requiring tracks to have at least three axial COT segments and two stereo COT segments, each with five or more hits. Also tracks must have a longitudinal coordinate (z_0) within 60 cm of the center of the interaction region to avoid any edge effects.

A fiduciality requirement guarantees that the center of the calorimeter cluster is not on the edge between towers, where the response is poorly predicted. The lateral shower profile cut is tailored to ensure close agreement with calibration data. There are also a series of quality cuts ensuring that the tracking information in the CES is in agreement with the COT track. A tighter cut ($E_{Had}/E_{EM} \leq 0.055 + 0.00044 E$) on the hadronic energy fraction further removes hadronic background.

One source which can mimic an electron coming from the interaction is the conversion of a photon into an electron-positron pair. At high energies they are produced with small separation angle, such that the positron track is nearly collinear with the electron. An algorithm rejects conversions by identifying such tracks.

The final requirement is angular isolation: the leptons cannot be close to any jet. This removes electrons produced by the semi-leptonic decay of a b -meson in a jet. Isolated electrons are defined as having most of their energy deposited in a narrow cone about the center of the EM cluster:

$$Isolation = \frac{E_T^{\Delta R \leq 0.4} - E_T^{Total}}{E_T^{Total}} < 0.1. \quad (3.1)$$

3.3.2 Tight Phoenix Electron Selection

To be detected in the plug calorimeters, electrons must travel at large $|\eta|$. Thus they rarely leave good tracks in the COT. If a plug electron leaves a quality track in the silicon detector which can be matched to an energy cluster in the PEM, it is kept and referred to as a phoenix (PHX) electron. To keep only the more central PHX electrons which are better measured by the detector, we require $|\eta| < 1.6$.

Tight PHX electrons are similar to central electrons; they are required to have $E_T \geq 20 \text{ GeV}$, $E_{HAD}/E_{EM} \leq 0.05$, and $Isolation < 0.1$. The matched silicon track must have at least three hits and $|z_0| \leq 60 \text{ cm}$. There are also similar matching requirements for the

PES and quality cuts on the shower profile. If the extrapolated silicon track is outside the defined window around the PES track, the PHX candidate is rejected.

3.3.3 Tight Muon Selection

Tight muons must have $P_T \geq 20 \text{ GeV}/c$, a COT track with hits in at least three axial segments and two stereo segments (each with at least five hits), and track $|z_0| \leq 60 \text{ cm}$. The extrapolated COT track must have an impact parameter relative to the beamline, $|d_0|$, of less than 0.2 cm if there are not silicon hits, and less than 0.02 cm if silicon hits are included. Additionally there is a cut on the quality of fit of the muon track to the COT hits; we require $\chi^2 \leq 2.3$, where χ^2 is the sum of the squares of the differences between each hit and the fit for each degree of freedom. This helps to exclude muons produced by secondary hadron decays.

Muons must leave very little energy deposition: $E_{HAD} \leq 6 + \text{MAX}[0, 0.028 \cdot (P - 100)] \text{ GeV}$ and $E_{EM} \leq 2 + \text{MAX}[0, 0.0115 \cdot (P - 100)] \text{ GeV}$. We also require $Isolation < 0.1$.

A fiduciality requirement ensures that the muon passes through the central volume of the muon detector. The track matching requirement depends upon the detector system; a COT track extrapolated to the muon stub must have an impact parameter of be less than 7.0 cm for the CMU, 5.0 cm for the CMP, and 6.0 cm for the CMX detector.

3.3.4 Loose Muon Selection

Muon acceptance is increased by including additional muons categories with less stringent stub requirements [23]; these are referred to as loose muons. Most of the requirements are the same as for tight muons: $P_T \geq 20 \text{ GeV}/c$, $Isolation < 0.1$ and track $|z_0| \leq 60 \text{ cm}$. The extrapolated COT track must have an impact parameter relative to the beamline of less than 0.2 cm if there are not silicon hits, and less than 0.02 cm if silicon hits are included. We still require $\chi^2 \leq 2.3$, $E_{HAD} \leq 6 + \text{MAX}[0, 0.028 \cdot (P - 100)] \text{ GeV}$ and

$$E_{EM} \leq 2 + \text{MAX}[0, 0.0115 \cdot (P - 100)] \text{ GeV}.$$

No CMX or CMUP trigger is required, nor is fiduciality in any detector. Loose muons may pass through the CMU, CMP, CMX, or BMU chambers, or through an uninstrumented location between them. Muons that pass through gaps in muon chamber coverage do not leave a stub, so there are no matching requirements for the COT track. Central muons must include at least three axial segments and two stereo segments with at least five hits per segment. For the high- η muons detected in the BMU, the tracks are only required to have a COT hit fraction ≥ 0.6 .

These loose muon categories add substantially to the total yield, contributing more events than the CMUP trigger requirement. This provides an overall twelve percent increase in candidate signal events.

3.4 Jet Selection

Quarks and gluons produced in an interaction rapidly hadronize into a collimated jet of neutral and charged particles which deposit energy in a contiguous set of calorimeter towers. This cluster of energy deposition must be identified and summed to determine the measured energy of the initial jet.

The identification of isolated energy clusters in the calorimeter is achieved with an algorithm called `JetClu`. It begins with the tower of highest energy, provided it is above $E_T \geq 3.0$. It adds the energies of all towers within a cone of $\Delta R < 0.4$ from the center of the first tower. The jet centroid is calculated as the energy-weighted sum of the clustered tower centers. The cone is moved to this jet centroid and the algorithm repeated to find a second centroid. This loop continues until the solution converges. The process starts again if there are additional towers with $E_T \geq 3.0$ GeV that were not included previously. Eventually, all the jets in the event are defined, along with their corresponding energy, η ,

and ϕ .

3.4.1 Jet Energy Corrections

A number of corrections to the clustered energy are needed to provide an estimate of the energy of the initial parton. These corrections are applied in the following order.

- Level 1 (η -Dependence): Corrects for the varying calorimeter response due to its non-uniformity over the full η -range
- Level 2: No longer used
- Level 3: No longer used
- Level 4 (Multiple Interactions): Subtracts energy contributed by a second interaction if it occurred simultaneously inside the detector
- Level 5 (Absolute): Corrects for energy lost in the gaps between towers; the jet energy is corrected according to the total P_T of the particles within a cone in the COT that matches the jet cone of $\Delta R < 0.4$ in the calorimeter
- Level 6 (Underlying Event): Some jet energy results from interactions between partons in the proton and antiproton other than those directly in the collision. Simulations of this process are calibrated using one-jet events in the data.
- Level 7 (Out-of-Cone): Based on simulation studies, this correction adds back the energy a jet typically deposits outside a cone of $\Delta R < 0.4$.

At the end of this procedure, the energy represents the energy of the original parton before fragmentation. Our selection requires two or three jets with a Level 5 $E_T \geq 20$ GeV and $|\eta| \leq 2.8$ relative to the detector. For event reconstruction, discussed in Chapter 5, jets are corrected to Level 7.

3.4.2 *b*-Tagging

As discussed in Chapter 2, the precision silicon tracking system allows detection of bottom quarks via the measurement of the small distances *b*-hadrons travel from the interaction before the *b*-quark decays. These hadrons have a lifetime of $\sim 10^{-12}$ s and thus travel about 0.3 mm if produced at rest [24]. The long-lived *b*-hadrons produce a cluster of tracks that point back to a secondary vertex offset from the primary interaction (defined by the highest-energy lepton’s intersection with the beamline). The `SecVtx` algorithm determines if the displacement is sufficient to “tag” the resulting jet as having originated from a *b*-quark. Note that charm quarks also form long-lived mesons that can produce secondary vertices. These tend to have lower momentum and with fewer charged tracks, but they are still often misidentified as *b*-jets.

`SecVtx` begins by identifying tracks which extrapolate into the cone of a jet. If at least two tracks have three or more hits in the silicon detector and $|d_0| \leq 0.3$ cm, there is sufficient information to make a determination; the jet is considered “taggable”. If there are more than two tracks meeting these requirements, the algorithm fits for the average vertex, success requiring that each track $\chi^2 < 50$.

If a solution is found, the algorithm then measures the transverse displacement of the secondary vertex from the beam. If the displacement is more than $3\times$ the uncertainty of the measurement, the result is significant enough to be considered a *b*-tag. Because the momentum of the *b*-hadron is conserved during its decay, the direction of the jet should be in the same direction as the displacement of the secondary vertex. This concept is illustrated in Figure 3.3. If this is not the case, i.e. if the jet direction differs from the displacement by more than 90° , the *b*-tag is discounted. Such “negative tags” are not used for selection, but they do provide an overall estimate of the rate at which light-flavor

jets are incorrectly b -tagged, discussed more in Chapter 4.

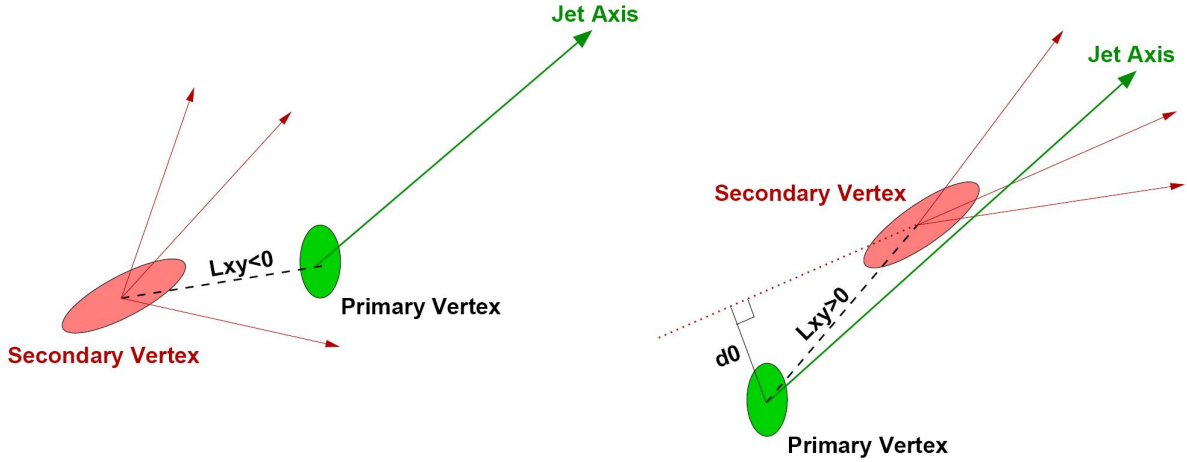


Figure 3.3: Illustration of secondary vertex identification. The figure on the left shows a displacement opposite the jet direction: a negative tag likely from track mismeasurement. On the right, the vertex displacement matches the jet direction, consistent with a b -hadron conserving momentum during its decay.

The overall b -tagging efficiency is shown in Figure 3.4. It depends on many factors, particularly energy, but for top decay events the efficiency peaks at around forty-five percent for 80 GeV jets. b -tagging is a powerful tool well suited for rejecting background processes, such as W bosons produced in association with light-flavor jets ($W+lf$). Because of the low efficiency, we only require that at least one of the two b -quarks is tagged in data. For our background model, simulated events are weighted by the probability of observing a b -tag for such an event, rather than whether a b -tag was actually found. This greatly increases the number of simulated events which can be used in our data model.

3.5 \cancel{E}_T Selection

Our signal is the $W' \rightarrow \ell\nu b\bar{b}$ final state. Chapter 2 discusses how the presence of this neutrino can be inferred from an overall imbalance in the transverse energy known as \cancel{E}_T . It is defined as the magnitude of the vector $\sum_i E_T^i \vec{n}_i$, where E_T^i are the magnitudes of transverse energy contained in each calorimeter tower i , and \vec{n}_i is the unit vector

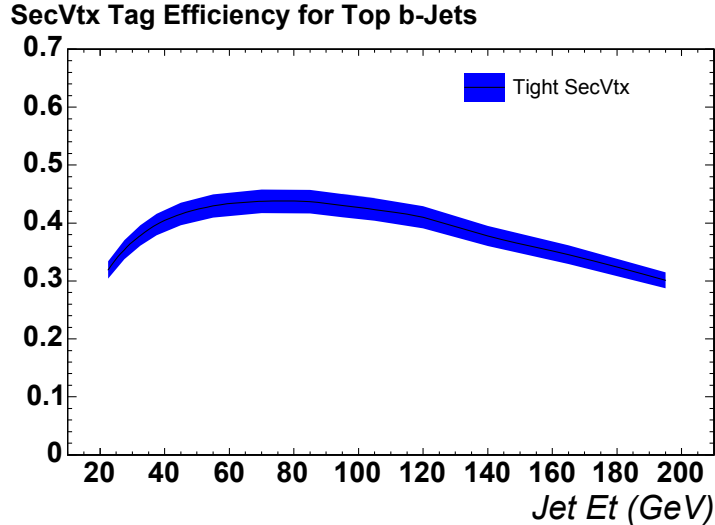


Figure 3.4: Tight SecVTX tagging efficiency as a function of jet energy for b -jets from top decay. From [25]

from the interaction vertex to the tower in the transverse plane. The muon momentum contribution used for the \cancel{E}_T calculation is determined by its track in the COT, minus any energy it deposits in the calorimeter (avoiding double-counting). Our selection requires $\cancel{E}_T \geq 25$ GeV, where the \cancel{E}_T is calculated with jets corrected to Level 5.

It is useful to know whether this energy imbalance is primarily from the jets and leptons or due to deposits of unclustered energy (calorimeter energy not part of jet). This is quantified in the \cancel{E}_T significance, defined as:

$$\cancel{E}_T^{\text{Sig}} = \frac{\cancel{E}_T}{\vec{E}_T^{\text{Unclustered}} \cdot \hat{\cancel{E}}_T}. \quad (3.2)$$

3.5.1 Non- W Background Removal

Some background processes, discussed in Chapter 4, do not contain W bosons or the associated neutrinos yet pass our \cancel{E}_T requirement. This non- W contribution can be reduced by removing events with very low \cancel{E}_T significance. A common source of the \cancel{E}_T for these events is a jet directed near a crack in the calorimeter coverage, resulting in

a \cancel{E}_T vector opposite that jet. This motivates a further cut on $\Delta\phi(\cancel{E}_T\text{-Jet})$. In addition, the W boson transverse mass (M_T^W), formed by summing the transverse components of the lepton and \cancel{E}_T , is generally very small. We use these characteristics as the basis of a non- W removal cut, or veto, customized for each lepton type:

$$\text{CEM: } M_T^W > 20 \text{ GeV}/c^2$$

$$\cancel{E}_T^{\text{Sig}} \geq -0.05 M_T^W + 3.5$$

$$\cancel{E}_T^{\text{Sig}} \geq 2.5 - 3.125 \cdot \Delta\phi(\cancel{E}_T\text{-Jet}_2)$$

$$\text{PHX: } M_T^W > 20 \text{ GeV}/c^2$$

$$\cancel{E}_T^{\text{Sig}} \geq 2.0$$

$$\cancel{E}_T > 45 - 30 \cdot \Delta\phi(\cancel{E}_T\text{-Jet}_{1,2,3})$$

$$\text{All Muons: } M_T^W > 10 \text{ GeV}/c^2$$

3.6 Other Selection Criteria

Several additional constraints are applied to veto unwanted background events:

- Cosmic Veto: This veto is necessary to reject muons produced by cosmic rays, many of which penetrate the detector volume every second. If two muon stubs on opposite sides of the detector are well-aligned, have tracks that pass far from the primary vertex, and the upper one occurred first (implying a skyward source), the muons are removed from consideration.
- Dilepton Veto: Events are removed if they contain more than one isolated lepton, whether tight or loose (Non-isolated leptons are treated as part of a jet)
- Z Veto: If an electron or muon can be combined with another isolated track of opposite sign, and they form a mass close to the Z mass (between 76 and 106 GeV/c^2), the lepton and track are not used.

- **z -Vertex Veto:** To ensure that all the objects detected in the event result from the same interaction, this veto requires the distance between the lepton and the primary vertex must be less than 5 cm. A vertex is defined by a collection of two or more good COT tracks generally associated with a jet. The primary vertex of the event is the vertex closest to the high- P_T lepton, or by the lepton vertex itself if there are not at least two good tracks in any jet.

3.7 Event Selection Summary

We employ $W+2$ and $W+3$ jet event selection to 1.9 fb^{-1} of Run II data as summarized below:

- **High- P_T Isolated Lepton:** We require one electron (tight CEM or tight PHX) or muon (tight or loose) with $P_T \geq 20 \text{ GeV}/c$ and $Isolation < 0.1$.
- **Large \cancel{E}_T :** We require $\cancel{E}_T \geq 25 \text{ GeV}$ using Level 5 corrected jets.
- **Two or Three High- E_T Jets:** We count jets corrected to Level 5 with $E_t \geq 15 \text{ GeV}$ and $|\eta| < 2.8$.
- **b -tag Requirement:** We require at least one of the jets have a b -tag.
- **Background Vetoes:** We reject events with characteristics consistent with cosmic rays, dileptons, Z decay, multiple interactions, or various non- W features.

In the data we find 1476 candidate events with two jets and 653 events with three jets. In order to better validate our model in the side-bands, we also retain the 2386 events with a single jet, though this channel will not be included in our measurement.

CHAPTER 4

Background Modeling

High-fidelity modeling is the key to the success of this analysis. We cannot simply count the events: we do not know our expected background rates well enough to measure such a small signal contribution. Instead we must look for small contributions to the tail of kinematics distributions, such as reconstructed mass, that separate the signal from background. The high-mass region is sparsely populated in data, so proper modeling of the small background impacts the amount of measured signal.

Backgrounds are processes that pass our selection criteria but do not include actual $W' \rightarrow t\bar{b}$ events. Most of these events contain no top quarks, and instead result from W bosons produced in association with one or more partons. These processes include $Wb\bar{b}$, $Wc\bar{c}$, Wc , and $W+lf$. Additional backgrounds have jets that result from hadronic decay of a W , Z , or τ ; these include $t\bar{t}$ pair production, s -channel and t -channel single top quark production, and diboson processes (WW , WZ , and ZZ). There is a small additional non- W background in which the lepton and \cancel{E}_T are from QCD processes rather than an actual boson. We discuss the underlying background processes, how they are simulated, and the method for determining their relative contributions.

4.1 Sources of Background

4.1.1 W +Jets

The dominant backgrounds in the W +2 jet and W +3 jet data are from W boson production in association with one or more partons. The basic processes are shown in the in Figures 4.1 and 4.2. We classify them according to the flavor of the quark pair produced: $Wb\bar{b}$, $Wc\bar{c}$, Wc , and incorrectly b -tagged W +lf (mistags). Even though only $Wb\bar{b}$ events contain actual b -quark jets, all these processes can contribute to the b -tagged background. Charm quarks form long-lived mesons that can produce secondary vertices (though generally with lower momentum and with fewer charged tracks) that are misidentified as b -jets. W +lf jets may contain long-lived strange particles which, in addition to occasional tracking errors, lead to a small probability of being mistagged as a b -jet. Since the light-flavor background is $500\times$ larger than the heavy-flavor contribution before the b -tag requirement, this small probability still leads to a significant mistag population.

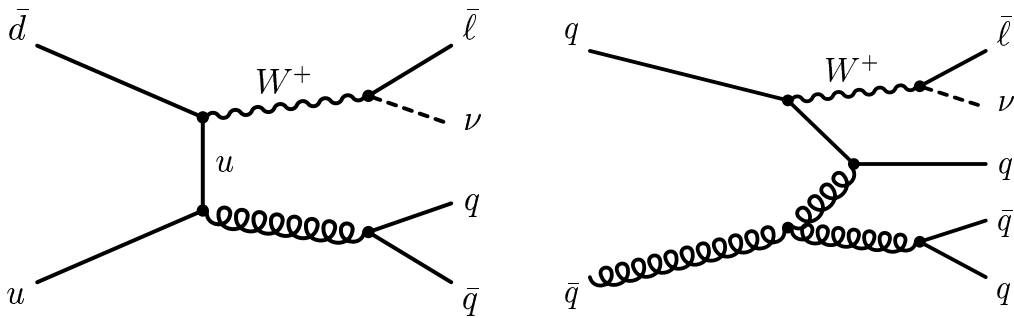


Figure 4.1: Representative Feynman diagram for $Wb\bar{b}$, $Wc\bar{c}$, and W +lf production to two jets (left) and to three jets (right).

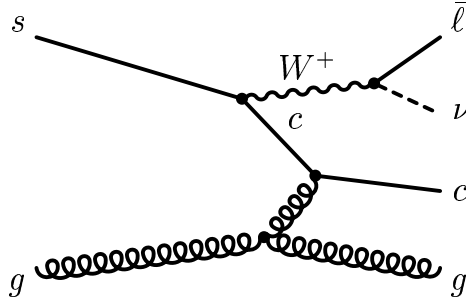


Figure 4.2: Representative Feynman diagram for Wc production.

4.1.2 $t\bar{t}$

The dileptonic $t\bar{t}$ decay produces an $\ell\bar{\ell}\nu\bar{\nu}b\bar{b}$ final state. To detect these events as $W+2$ or $W+3$ jets, one lepton must be missed. For electrons this can happen when one travels into a crack in the calorimeter coverage or along the beampipe. One of the leptons may also be counted as part of a jet. The dilepton veto and isolation requirement help to reduce this, but some top dilepton background persists.

The semi-leptonic decay of $t\bar{t}$ typically produces an $\ell\nu b\bar{b}q\bar{q}$ final state. To contribute to the $W+3$ jet channel, only one of the jets needs to be missing. This could occur because it had very little energy, was aligned with the beampipe, or overlapped with another jet. Missing two of the four jets is less likely, and thus the contribution of this background to W +jets is much smaller.

4.1.3 Single-Top

Most top quarks at the Tevatron are strongly produced in pairs, but they also are produced individually via the electroweak processes known as single top. Diagrams for these processes are shown in Figure 4.3. About a third of single-top-quark production

occurs via the same s -channel process as W' , but with an off-mass-shell Standard Model W boson. The t -channel requires the presence of a b -quark supplied by gluon fusion, and contributes the majority of single-top events. Single-top production results in the same final state as W' , so our selection is very efficient at keeping this background. In fact, this analysis is adapted from the selection and modeling techniques created and optimized for single-top searches [22].

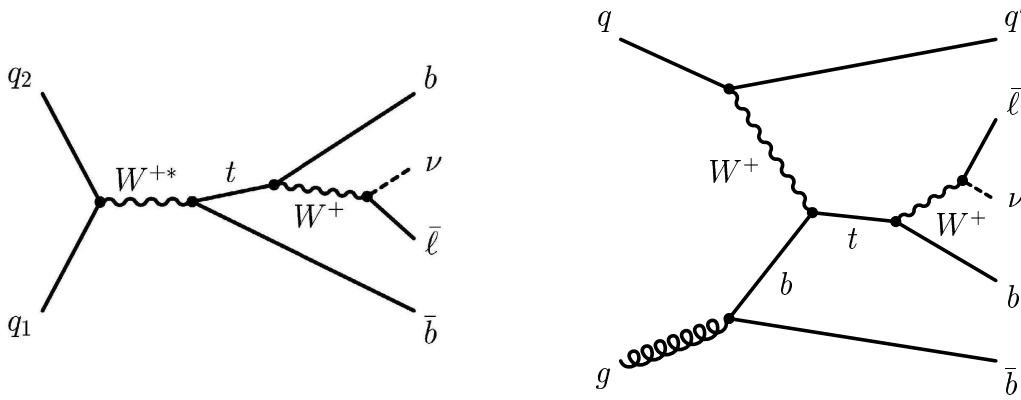


Figure 4.3: Feynman diagram for s -channel single top production (left), and t -channel single top production (right).

4.1.4 Diboson

Vector boson pair production includes WW , WZ , and ZZ processes (diboson); the predominant ones are illustrated in Figure 4.4. The events passing selection for a lepton, missing transverse energy, and jets typically have one boson which decays hadronically and one which decays leptonically. The b -tag can be generated in a number of ways: WW can produce an $l\nu cs$ final state where the charm jet gets b -tagged, WZ can produce the same $l\nu b\bar{b}$ final state, and ZZ can produce an $\ell\bar{\ell}b\bar{b}$ final state. As with dileptonic $t\bar{t}$ decay, any second lepton can be counted as a jet or lost in a crack or along the beampipe. The Z veto in our selection reduces the WZ contribution, and nearly removes ZZ entirely.

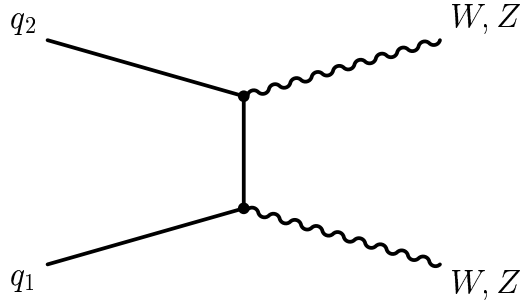


Figure 4.4: Representative Feynman diagram for WW , WZ , and ZZ production.

4.1.5 Z +jets

As in the diboson case, occasionally a Z boson will decay to a lepton pair and one lepton will get lost in a crack. It will appear as a lepton and \cancel{E}_T , faking the kinematics of a W event. If a radiated gluon produces a $b\bar{b}$ pair, this event will appear as $Wb\bar{b}$. These jets can also be produced by $Z \rightarrow \tau\bar{\tau}$ if one τ decays to quarks. There is a large cross-section for Z +jets, as with W +jets, but passing W selection is unlikely so the background contribution is small. This process is often lumped in with the much larger diboson background for convenience.

4.1.6 Non- W

Finally there are backgrounds that do not contain an actual boson. The lepton is produced by semi-leptonic b -decay, when a pion decays to $\mu\nu$, or when a QCD jet produces a false signal in the electromagnetic calorimeter. Generally the resulting lepton will be close to the jet which produced it, thus failing the isolation requirement. These events may have a source of large \cancel{E}_T , such as a jet which is centered on a crack in the calorimeter. The QCD veto reduces this source of \cancel{E}_T by removing events in which the \cancel{E}_T is directly

opposite a large jet. Nonetheless, a small non- W component (also assumed to be non- Z) remains.

4.2 Background Simulations

A unique simulation is created for each background processes, except non- W . This is a multi-step process: the simulation must generate initial conditions for the colliding partons, calculate the kinematics of the particular interaction, simulate the showers of the final-state partons, and model their interaction with the detector. The initial conditions of the incoming partons are determined from parton distribution functions (PDF's) which predict the momentum distribution among the quarks and gluons within the proton and antiproton based on other experiments. These incident momenta are fed into an event generator, which solves the matrix elements for the various leading-order or next-to-leading-order processes included as part of that background. The outgoing partons must be translated to jets by modeling of the hadronization process (parton showering). Finally these results are passed through a simulation of the detector response, `CDFSim`.

The generators and showering algorithms for our background simulations include:

- `PYTHIA` [26], a semi-leading-order generator which includes parton showering, used for its speed and convenience.
- `ALPGEN` [27], a leading order matrix element generator tailored to describe electroweak bosons produced in association with energetic, well-separated partons.
- `Herwig` [28], a leading order matrix element generator which includes parton showering models for the emission of low-energy gluons, used coupled to `ALPGEN` to provide showering.
- `MadEvent` [29], a leading order generator that includes color effects and spin polar-

ization effects, but not parton showering.

A summary of all the simulated background components and their event generators/showering is shown in Table 4.1.

Background	Generator	Showering	Simulation Datasets
Wbb	ALPGEN	HERWIG	btopXp
$Wc\bar{c}, Wc$	ALPGEN	HERWIG	ctopXw, stopwX
Mistagged $W+lf$	ALPGEN	HERWIG	ptopXw, utopXw
Non- W	Data	Data	anti-electrons, jet-electrons
$t\bar{t}$ (dilepton)	PYTHIA	PYTHIA	ttop75
$t\bar{t}$ (lepton+jets)	PYTHIA	PYTHIA	ttop75
Single Top (t -channel)	MadEvent	PYTHIA	stop00
Single Top (s -channel)	MadEvent	PYTHIA	stopm0
WW	PYTHIA	PYTHIA	itopww
WZ	PYTHIA	PYTHIA	itopwz
ZZ	PYTHIA	PYTHIA	itopzz
Z +jets	ALPGEN	PYTHIA	ztopXY
W'	PYTHIA	PYTHIA	wptbXY

Table 4.1: Simulated background components and associated datasets.

A W' signal would appear as a slight excess of events with large reconstructed mass, appearing in the decaying tail of the mass distribution. This high-mass region is sparsely populated in data, requiring a precise understand the background contribution in order to make a sensitive measurement. We do this by simulating many more background events than are observed in data. Producing these simulated events is very time consuming; typically our background models contain $10\times$ as many events as data to improve our model at large mass while minimizing the computational resources required.

4.2.1 Removal of Overlap in Background Simulations

Simulated datasets are classified according to the generator-level processes they include. When different programs are used for generation and parton showering, overlap between these datasets can occur. This is an issue for the W +jets events produced by ALPGEN + Herwig. For example, some W +2 jet events generated by ALPGEN will gain a jet during showering with Herwig. These overlap with W +3 jet events generated by

ALPGEN and must be removed to avoid double-counting. Our removal scheme [30] requires that each jet-cone in an event contains exactly one generator-level parton and that the jet multiplicity must match the number of partons. All events with the same jet-multiplicity are then grouped together, regardless of the simulation which produced them.

There is an additional source of overlap for W +jets: bottom and charm quarks are occasionally produced in the light-flavor simulation during parton showering. These processes are already generated by the $Wb\bar{b}$ and $Wc\bar{c}$ simulations and thus can be double-counted. To avoid this, events with bottom and charm generated by the $Wb\bar{b}$ and $Wc\bar{c}$ simulations are kept only if the two heavy quarks are in different jets, while those generated by showering in light-flavor simulation are kept only if the heavy quarks lie in the same jet [31]. The result is that all the W +jets simulations can contribute events to the W +bottom background and W +charm background.

Another example of overlap occurs in the t -channel single-top simulation. The initial b -quark needed for this process can be produced by the event generator or by the showering algorithm via gluon splitting. A matching procedure [32] is used to properly mix the various contributions.

4.2.2 b -Tagging Treatment and Weighting of Simulated Events

Most of the background processes we simulate, such as $t\bar{t}$ production, may result in a variety of final state particles. Some simulations, such as ZZ , very rarely produce events which contain a b -quark. Because they are very computationally intensive to run, we cannot always simulate enough events to have a large remainder after our selection requirements are applied, particularly the b -tag requirement. This requirement is not used for selection of simulated events. Instead of requiring b -tags, we apply an overall weight to each event corresponding to their likelihood of having a b -tag. The result is that our

prediction for the expected mass distribution uses information from a greater number of events, and thus has smaller statistical fluctuations. This improves our overall sensitivity in the high-mass tail by better characterizing our expected Standard Model contribution.

We first select events that pass all selection criteria except the b -tag requirement. These are referred to as pretag events. These events are then weighted by the sum of the probabilities that each jet in the event would be tagged. These events are then summed according to their weights to give the overall prediction for the mass distribution. This weighting approach is useful because we are making use of additional information: instead of representing the b -tagging state as zero or one, we express the b -tag probability using the whole interval from zero to one.

The probability that a jet in a particular event will be reconstructed as a b -tag is based upon a number of kinematic properties which have been studied in data. Data have shown that the b -tagging rate can be determined primarily from jet E_T , η_{jet} , η_{vert} , z_{vert} , the number of good silicon tracks in a jet, and the sum E_T for the event. The resulting b -tag probability [33] can be determined for both positive b -tags and negative b -tags. The negative tagging rate is used later when determining the contribution of mistag events.

A simulated event's weight also includes a few minor correction factors. Some are necessary because the simulation does not account for how the detector configuration evolves over time: run-dependent changes to calibrations, active subdetectors, software, trigger definitions. Another correction accounts for the differing number of events produced by our W +jets simulations. This correction ensures, for example, that the $Wb\bar{b} + 1p$ and $Wb\bar{b} + 2p$ components have the proper cross-sections so they can be combined. A second weight involves events selected using the \cancel{E}_T trigger: those with PHX electrons or loose muons. Selection requires $\cancel{E}_T \geq 25$ GeV, but these triggers are not fully efficient until

the \cancel{E}_T is roughly 35 GeV. This means that to avoid over-representing low \cancel{E}_T events in simulation, we must use a trigger efficiency that is \cancel{E}_T -dependent. Weighting at the event level is the simplest treatment to account for this non-uniform trigger efficiency.

4.2.3 Mistag Model

There are several approaches for modeling the kinematics of events with mistagged light-flavor jets. One approach is to use events in the data with negative b -tags. All negative b -tags are non-physical (Chapter 3) and thus are mistags. They can be used to model the positive mistags in the data. There are not enough negative b -tags in the data to produce a smooth prediction for the mass distribution, however. One alternative is to simply use pretag data, weighting events according to their mistag probability. This selection provides better statistics but retains some correlation with the data, particularly in our high-mass signal region. We reject this approach, though we do use it as a substitute to quantify our mistag-modeling uncertainty (Chapter 6).

We model this background using simulated ALPGEN W +jets events matched to light flavor. As discussed above, heavy-flavor overlap removal is addressed by matching all jets to generator level partons. We include any heavy- or light-flavor event without a bottom or charm quark. Some mistagged light-flavor events do come from heavy-flavor simulations, though most are from W +lf.

4.2.4 Non- W Model

Non- W events are difficult to simulate because they include a variety of miscellaneous QCD processes that are poorly understood. Without a solid physical model, we must use a data-based approach to represent this background. This is the only process predicted by data rather than simulation, though we use only data events which are not included in our signal selection.

For a non- W event to pass our selection, a jet must be mistaken for an isolated lepton. We represent this using non- W enriched data which contains objects that pass all but two of our standard non-kinematic electron ID cuts: CES Δx , CES Δz , hadronic fraction, lateral shower profile, and track χ^2 . If these objects, referred to anti-electrons, are treated as tight electrons. They provide a good kinematic model of electrons in the non- W background.

The PHX electrons involve a complex, non-standard selection such that an anti-PHX election dataset has not been made. Instead we use data containing high- η jets which deposit energy in a way consistent with a PHX electron; this is referred to as the jet-electron dataset. The jet must have at least four tracks (to be sure it is not an actual electron) and EM_{frac} between 0.8 and 0.95 (to be consistent with an electron). These jets are then treated as tight PHX electrons.

This composite of anti-electron plus jet-electron data is assumed to be sufficient for also modeling the non- W events containing muons. As with the simulated events, we do not require b -tags, but weight events by their b -tag probability to improve the model's statistics.

4.3 Preliminary Background Contributions

Each background process results in a unique mass distribution. When summing to give an overall prediction for the data, we must consider the relative rates. Each background component must be scaled (or normalized) to the number of events it is expected to contribute to data. Some background contributions are determined from well known theoretical cross-sections (Table 4.2) and the rate which simulated events pass our selection criteria:

$$N_{BG} = \sigma_{BG} \cdot \epsilon_{BG} \cdot \epsilon_{btag} \int \mathcal{L} dt. \quad (4.1)$$

The term ϵ_{BG} is the overall pretag selection efficiency for that process and is given by the selection efficiency in simulation multiplied by data-based corrections for trigger efficiency, lepton ID efficiency, and z -vertex range. Other processes such as W +jets and non- W are difficult to predict, and thus their contribution must be determined from data [34]. They are more easily distinguished using the pretag data, because without the b -tag requirement, only the contributions from W +jets and non- W are significant.

Background	Theoretical Cross-section
$t\bar{t}$	6.7 ± 0.08 pb
Single Top (t -channel)	1.98 ± 0.08 pb
Single Top (s -channel)	0.88 ± 0.05 pb
WW	12.4 ± 0.25 pb
WZ	3.96 ± 0.06 pb
ZZ	1.58 ± 0.02 pb
Z +jets	787.4 ± 50 pb

Table 4.2: Theoretical cross-sections for electroweak backgrounds produced via $p\bar{p} \rightarrow X$.

Thus the first step is to determine the pretag fraction of non- W events in data using fits. The prior “four-sector” method was deficient in that it assumes that \cancel{E}_T and lepton isolation are independent and does not give consistent results using different jet energy corrections. The kinematic distribution which best separates the non- W and W +jets backgrounds is \cancel{E}_T ; this is because the non- W events do not have a neutrino contributing to the production of \cancel{E}_T . To boost the separation, we also remove our \cancel{E}_T cut from the pretag selection. We perform a two-component fit to the data to obtain the raw non- W fraction. We correct for the \cancel{E}_T cut by multiplying by the \cancel{E}_T selection efficiencies (ϵ^{MET}) in pretag data and non- W events:

$$N_{nonW}^{pretag} = N^{pretag} \cdot F_{nonW}^{pretag} = N^{pretag} \cdot \frac{N_{nonW}^{pretag, preMET}}{N^{pretag, preMET}} \cdot \frac{\epsilon_{nonW}^{MET}}{\epsilon^{MET}}. \quad (4.2)$$

We subtract the non- W and electroweak contributions (determined using Equation 4.1) from the pretag events; the remainder are from W +jets. From our simulations we know

the fraction of pretag W +jets events that match to heavy flavor. Multiplying by the b -tagging efficiency converts to the tagged contribution.

$$N_{W+hf}^{tagged} = N_{W+jets}^{pretag} \cdot F_{W+hf}^{pretag} \cdot \epsilon^{btag} = (N^{pretag} - N_{nonW}^{pretag} - N_{EW}^{pretag}) \cdot F_{W+hf}^{pretag} \cdot \epsilon^{btag}. \quad (4.3)$$

F_{W+hf}^{pretag} and ϵ^{btag} can be calculated for each heavy-flavor process ($Wb\bar{b}$, $Wc\bar{c}$, Wc) separately to determine their rates individually.

If F_{W+hf}^{pretag} is the fraction of pretag W +jets events that are from heavy flavor, then $F_{W+lf}^{pretag} = 1 - F_{W+hf}^{pretag}$. The mistagging efficiency is estimated from the fraction of negative b -tagged events observed in data, F_{negtag}^{pretag} . Since poor reconstruction of a vertex is as likely to produce a negative displacement as a positive one, the amount of negative tags approximates the amount of positive mistags. Thus the mistagged light-flavor contribution is:

$$N_{W+lf}^{tagged} = N_{W+jets}^{pretag} \cdot F_{W+lf} \cdot \epsilon^{mistag} = N_{W+jet}^{pretag} \cdot F_{W+lf} \cdot F_{negtag}^{pretag}. \quad (4.4)$$

We now have preliminary background normalizations for all components.

4.4 Correction to Bottom and Charm Fractions in Simulation

An additional complication arises: this technique consistently predicts a total event rate well below that observed in data [35]. This trend is most severe in the one and two jet bins, and the deficiency has only grown with the increase in data during Run II. The mismatch between our prediction and the data is shown in Figure 4.5. This discrepancy appears to be the result of imperfect modeling of W +hf. This is because the **ALPGEN** simulation is known to neglect some important higher-order effects, and the discrepancy is roughly proportional to the heavy-flavor contribution in a particular jet bin. The excess in data does not appear consistent with new physics in various control samples. It was determined a correction to the heavy-flavor fraction was needed to absorb this departure

from data.

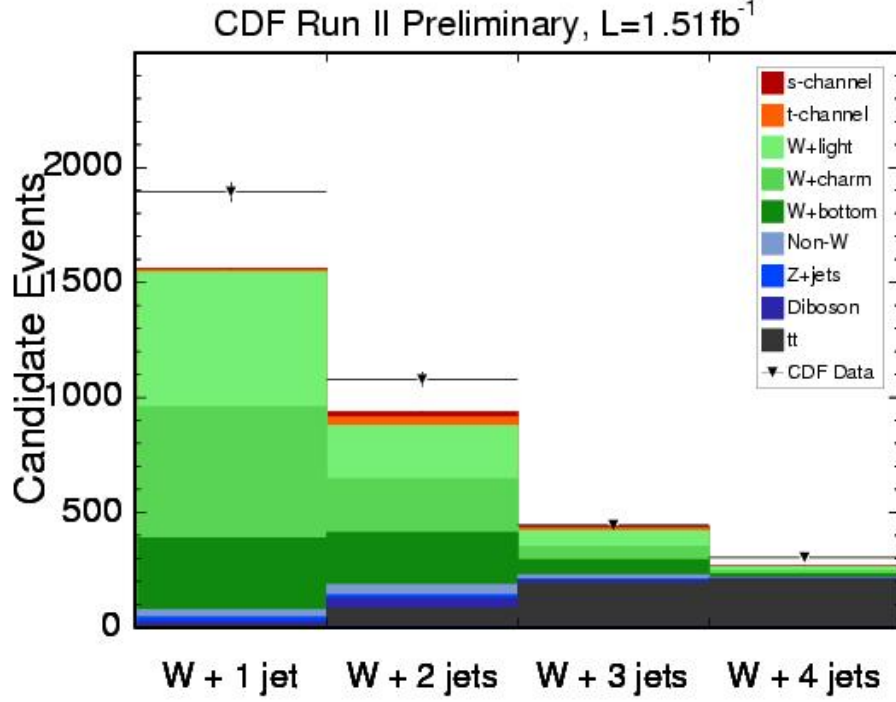


Figure 4.5: Standard Model prediction as a function of jet multiplicity.

This correction, known as the k-factor, may differ for $Wb\bar{b}$, $Wc\bar{c}$, and Wc . We assume the k-factor for $Wc\bar{c}$ and Wc are indistinguishable:

$$KF_b = \frac{F_{Wb\bar{b}}^{data}}{F_{Wb\bar{b}}^{Sim}} \approx \frac{F_{bjets}^{data}}{F_{bjets}^{Sim}}, \quad KF_c = \frac{F_{Wc\bar{c}+Wc}^{data}}{F_{Wc\bar{c}+Wc}^{Sim}} \approx \frac{F_{cjets}^{data}}{F_{cjets}^{Sim}}. \quad (4.5)$$

We know the quark flavor matched to the jets in our simulated data, and thus can directly determine the denominators. Distinguishing the flavor associated with a particular jet in data (numerator) is more difficult. Our approach is to measure a related quantity, the fraction of b -tagged jets corresponding to a particular flavor, in the data in order to determine the k-factor.

This is how F_{bjets}^{data} or F_{cjets}^{data} can be determined. The fraction of jets from a b -quark times the bottom tagging efficiency, ϵ_{btag} , is equal to the fraction of jets that are b -tagged

times the fraction of b -tagged jets from b -quarks:

$$F_{bjets}^{data} \times \epsilon_{btag} = F_{tagged\ jets}^{data} \times F_{tags\ from\ b}^{data} \quad (4.6)$$

The relation for charm flavor is analogous. We determine the bottom and charm fractions in data from the tagging efficiency, the observed b -tagging fraction, and a measurement of the fractions of b -tagged jets from bottom and charm quarks (F_{bjets}^{data} or F_{cjets}^{data}).

We assume that the k-factor is not strongly dependent on jet multiplicity, which we later verify by direct comparison. Thus we can measure the bottom and charm fractions by fitting the $W+1$ jet data, and apply the results to our search region, the $W+2$ and $W+3$ jet data. In this way we can calibrate using data that is not part of our final measurement. The b -tagged $W+1$ jet background is modeled as the sum of three components: simulated W +bottom events in which a jet matches a b -quark, simulated W +charm events in which the jet matches a charm quark, and simulated W +lf events in which the jet is not matched to a bottom or charm quark. The light-flavor component is normalized to its expected contribution and the charm and bottom component normalizations are unconstrained during the fit. The results are corrected to subtract the bottom and charm contributions from electroweak processes. This is done based on matching studies in the various simulated electroweak data. The adjusted bottom and charm fractions are then inserted into Equation 4.6 to determine the bottom and charm k-factors.

The best distribution for distinguishing jet flavor is the mass of b -tagged jet, constructed from the tracks in the secondary vertex. To include a larger number of tagged events, we used a less stringent set of b -tagging criteria known as “loose” b -tagging [36]. As a check for consistency, we repeat the fit with an alternative distribution: the Karlsruhe neural-net discriminant (KNN) [37]. The KNN is a combination of variables optimized

to separate bottom jets from those of other flavors. A comparison of these distributions is shown in Figure 4.6. For our final result, we average the k-factors derived from fitting both distributions.

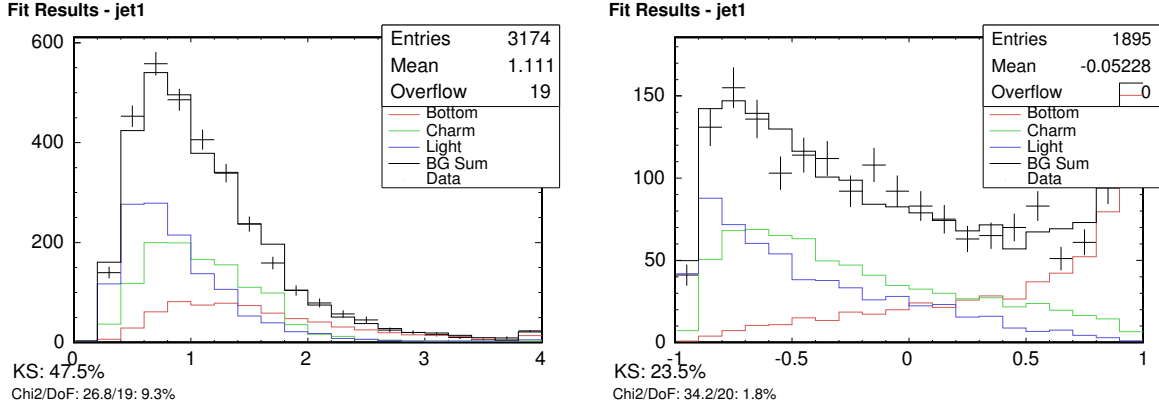


Figure 4.6: Fit of the bottom and charm fractions in $W+1$ jet data using the loose secondary vertex mass distribution (left) and using the KNN discriminant distribution (right). The light-flavor fraction is fixed to its expected contribution.

Our measured fractions and the corresponding k-factors are shown in Table 4.4. Apparently the contributions from both bottom and charm in the data are forty percent larger than simulation suggests. Based on the similarity of these results, we use a common k-factor for both bottom and charm: $KF = 1.4 \pm 0.4$. The uncertainty was determined by repeating the calculation in the $W+2$ jet bin, shown in Figure 4.7, and noting the variation. The result supports the assumption that the k-factor does not depend strongly on jet multiplicity. The k-factor uncertainty, shown as the hashed band in the figure, is derived as the maximum deviation of the measurement from the average and symmetrically applied. These fits use a 1.51 fb^{-1} subset of our data; results from the full 1.9 fb^{-1} are consistent. We return to the background calculation to apply the heavy-flavor calibration ($KF = 1.4 \pm 0.4$) and determine our final background prediction.

Fraction	1-jet Data (KNN)	1-jet Data (Loose Vertex Mass)
bottom	0.317 ± 0.019	0.220 ± 0.021
charm	0.374 ± 0.025	0.370 ± 0.025
light flavor	0.380 ± 0.000	0.409 ± 0.000
$K F_b$	1.757 ± 0.118	1.669 ± 0.178
$K F_c$	1.211 ± 0.082	1.412 ± 0.100

Table 4.3: Result of heavy-flavor fits in $W+1$ jet data using the secondary vertex mass for loose tags (left) and the KNN discriminant (right).

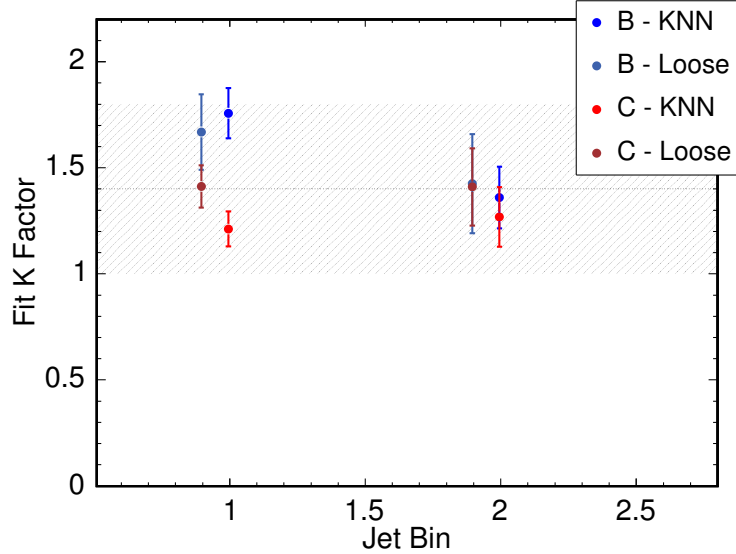


Figure 4.7: k-factors for bottom (blue) and charm (red), using loose SecVtx mass and the KNN discriminant. In $W+1$ jet bin we measure approximately $K F = 1.4$ for both bottom and charm. The $W+2$ jet case is shown only for error estimation.

4.5 Corrected Background Contributions

We repeat the calculations for the light and heavy-flavor expectations using the new k-factor. Having a precise prediction of the contributions from W +jets and electroweak processes, we can refine our non- W prediction (which had earlier been estimated from fitting pretag data). We now have sufficient information to directly fit the tagged data for this contribution. We construct a background model for the b -tagged \cancel{E}_T distribution, again removing the cut on \cancel{E}_T . We normalize each background component to its

expected contribution, summing all except non- W . We then fit the b -tagged data with two components: the summed backgrounds fixed within their overall uncertainty and the non- W component which is unconstrained. The measured non- W fraction is corrected for the absent \cancel{E}_T requirement via multiplication with the \cancel{E}_T selection efficiency. This final procedure only revises the non- W fraction; all others remain fixed.

The final Standard Model predictions are shown in Table 4.4. Figure 4.8 shows the background prediction after applying the k-factor. The final prediction is in much better agreement with the data than before the correction (Figure 4.5). The various systematic uncertainties are properly propagated through these calculations. The sources of these uncertainties are discussed in Chapter 6.

Background	2 Jets 1 b -Tag	3 Jets 1 b -Tag	2 Jets 2 b -Tags	3 Jets 2 b -Tags
Wbb	361.2 ± 108.8	107.8 ± 32.5	48.2 ± 15	17.8 ± 5.5
$Wc\bar{c}$	406.9 ± 125.5	106.5 ± 32.7	5.5 ± 1.8	2.9 ± 0.9
Mistagged $W+lf$	275.4 ± 34.8	81.6 ± 10.5	1.2 ± 0.3	0.8 ± 0.2
Non- W	52.4 ± 21	18.4 ± 7.3	1.2 ± 0.5	0.2 ± 0.1
$t\bar{t}$ (dilepton)	33.9 ± 4.7	27.5 ± 3.8	9.4 ± 1.5	9.3 ± 1.5
$t\bar{t}$ (lepton+jets)	69.3 ± 9.7	197.4 ± 27.5	13.9 ± 2.3	57.6 ± 9.5
Single Top (t-channel)	27.3 ± 3.8	8.7 ± 1.2	8 ± 1.3	2.8 ± 0.5
Single Top (s-channel)	51.9 ± 7.6	13.6 ± 1.9	1.5 ± 0.3	2.2 ± 0.4
WW	36.1 ± 4	12.8 ± 1.4	0.2 ± 0	0.3 ± 0
WZ	14.7 ± 1.1	4.2 ± 0.3	2.9 ± 0.3	0.9 ± 0.1
ZZ	0.5 ± 0	0.2 ± 0	0.1 ± 0	0 ± 0
Z +Jets	21.5 ± 3.2	8.7 ± 1.3	1 ± 0.2	0.6 ± 0.1
Total Prediction	1351.1 ± 238.1	587.5 ± 73.0	93.0 ± 17.4	95.5 ± 12.6
Data	1273	520	89	97

Table 4.4: Standard Model background predictions for tagged event in $1.9 fb^{-1}$

4.6 Validation of Background Prediction

We validate our background model by comparing to data in over 40 different distributions. We examine the level of agreement separately for the $W+1$ jet, $W+2$ jet, and $W+3$ jet data; we also consider separately distributions with zero, one, or two b -tags [38]. Our model distributions are in agreement with the data in these regions, and our distributions

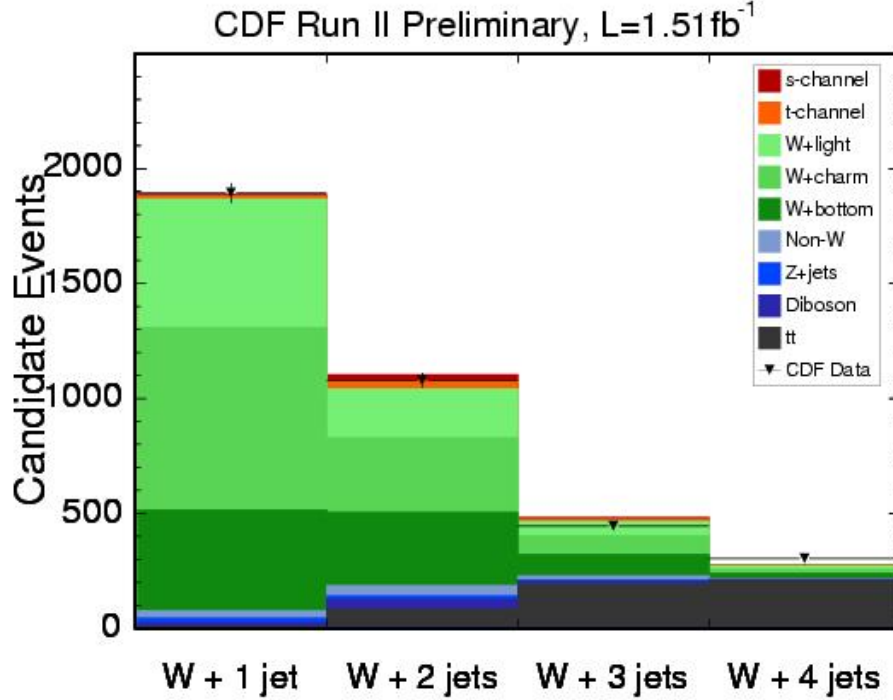


Figure 4.8: Standard Model prediction as a function of jet multiplicity after applying the correction to heavy-flavor fraction.

are consistent with prior validation for single top [39]. Figure 4.9 shows the lepton P_T distribution, Figure 4.10 shows the energy of the lead, or highest-energy, jet, Figure 4.11 shows the \cancel{E}_T distribution and Figure 4.12 shows the transverse W mass. These are important variables because they contribute to the $M_{t\bar{b}}$ distribution, discussed in Chapter 5, in which we make our measurement; the shapes for the signal distribution are shown in Chapter 5. All show good agreement with expectation for the bulk of the distribution. A slight excess of events with large jet E_T and large lepton P_T is noted. Any statistical significance of these contributions will be apparent in our limit procedure.

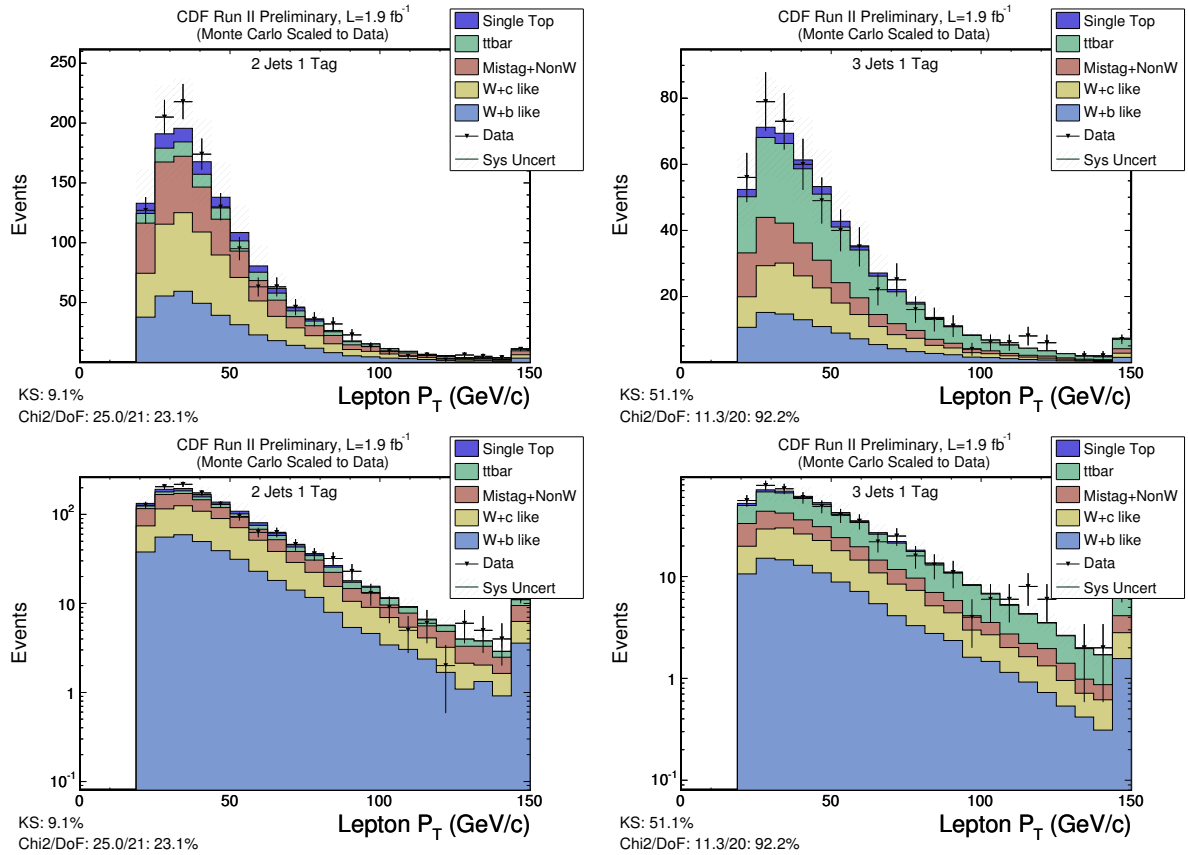


Figure 4.9: Comparison of the model lepton P_T distribution to the data for the 2 jet 1 b -tag channel (left) and the 3 jets 1 b -tag channel (right). The bottom row shows the plots on a log scale.

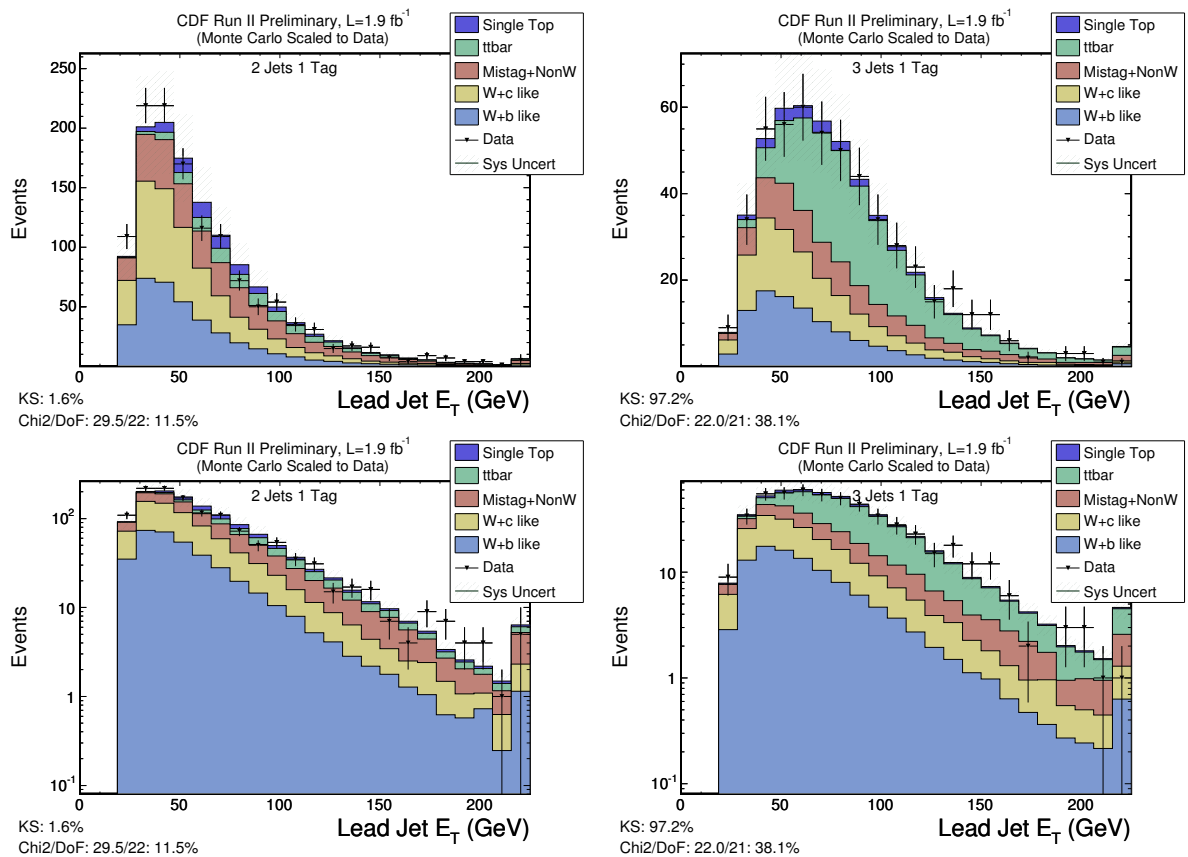


Figure 4.10: Comparison of the model lead jet E_T distribution to data for the 2 jet 1 b -tag channel (left) and the 3 jets 1 b -tag channel (right). The bottom row shows the plots on a log scale.

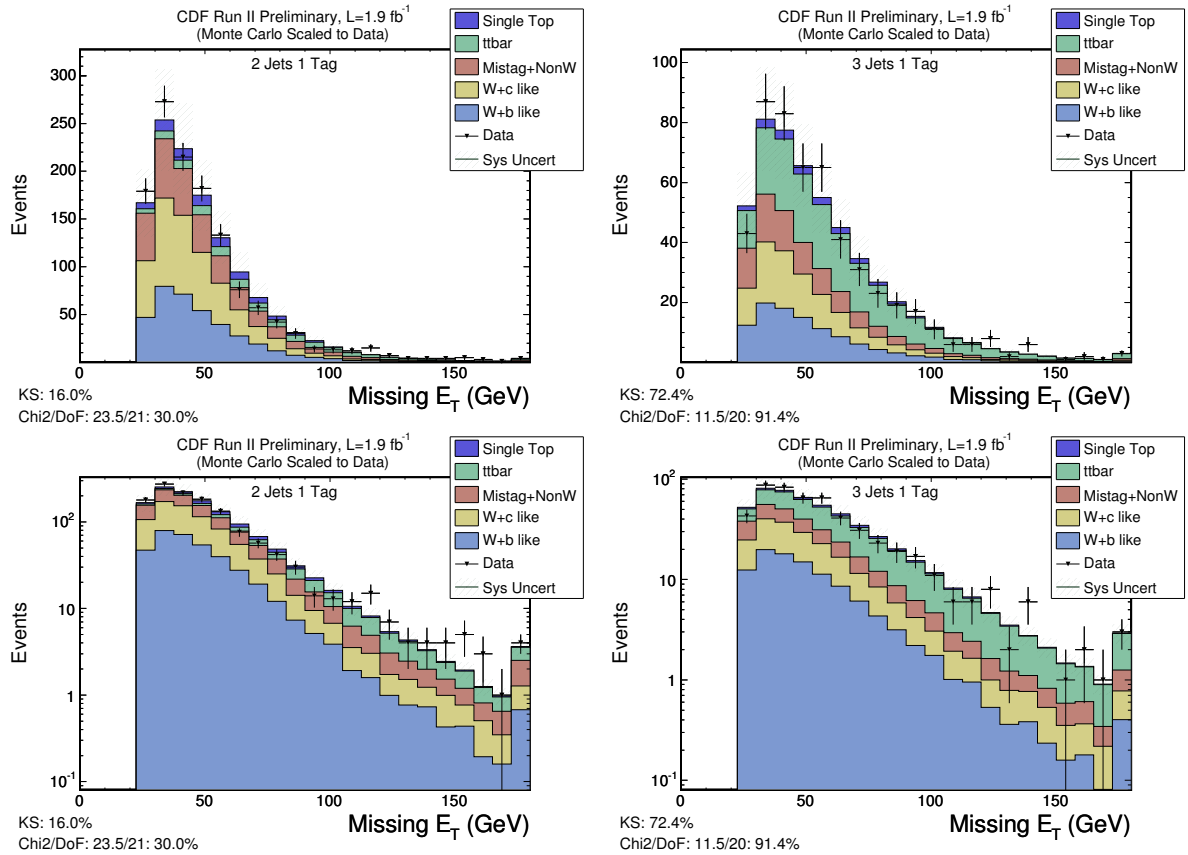


Figure 4.11: Comparison of the model E_T distribution to data for the 2 jet 1 b -tag channel (left) and the 3 jets 1 b -tag channel (right). The bottom row shows the plots on a log scale.

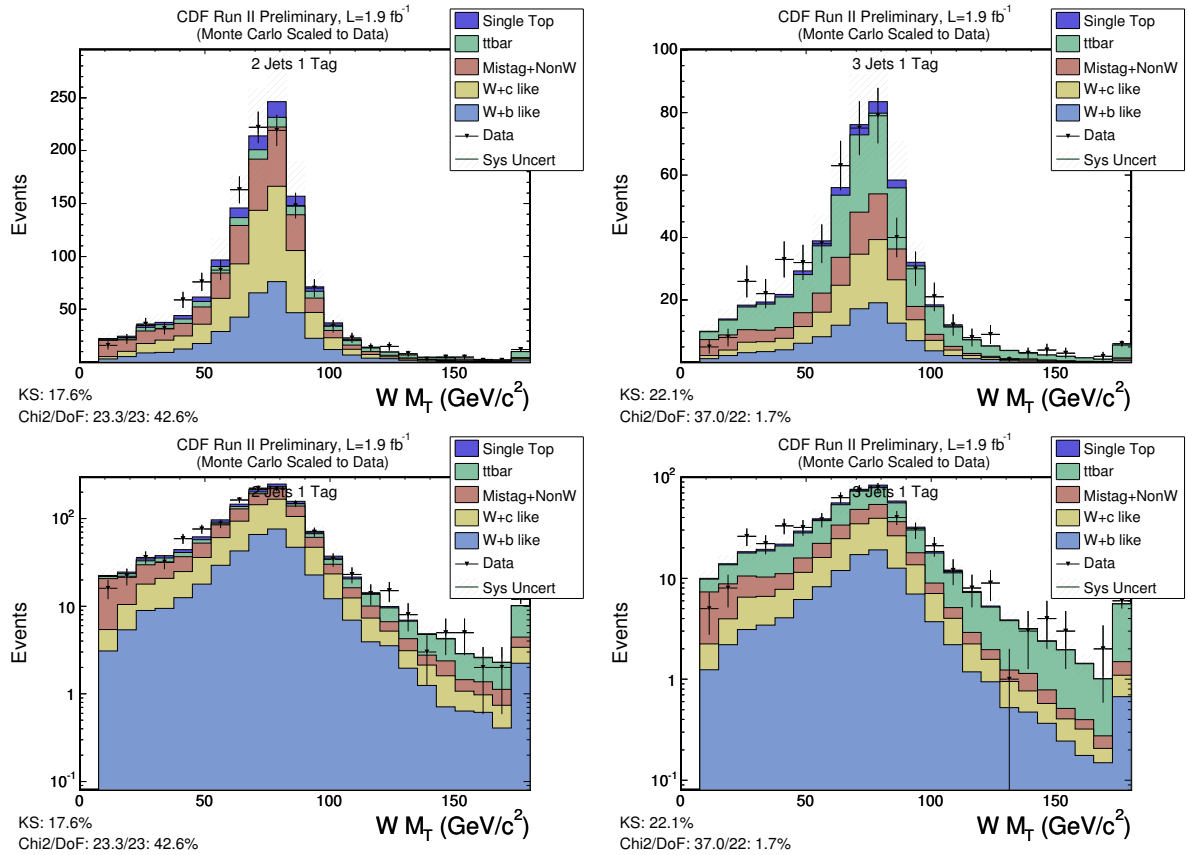


Figure 4.12: Comparison of the model transverse W mass distribution to data for the 2 jet 1 b -tag channel (left) and the 3 jet 1 b -tag channel (right). The bottom row shows the plots on a log scale.

CHAPTER 5

W' Signal Measurement

5.1 Methodology

We are searching for a small excess of events in the data consistent with our W' hypothesis. The expected signal contribution is much smaller than the uncertainty of our predicted background rate, as shown in Table 5.1. Thus we cannot simply count data events to see whether W' is present, nor can we confidently determine on a case-by-case basis whether a detected event is from signal. To discriminate signal from background we must use kinematic distributions from many such events and look for differences.

	2 Jets 1 b -Tag	3 Jets 1 b -Tag	2 Jets 2 b -Tags	3 Jets 2 b -Tags
Data Events	1273	520	89	97
Prediction BG Events	1351.1 ± 238.1	587.5 ± 73.0	93.0 ± 17.4	95.5 ± 12.6
Predicted W' Events	10.3	6.8	2.0	1.6
S/B	0.008	0.013	0.022	0.016
S/\sqrt{B}	0.29	0.30	0.21	0.16

Table 5.1: Predicted background (BG) and signal events in $1.9 fb^{-1}$ in the case of $M_{W'}=800 GeV/c^2$ and $M_{W'} < M_{\nu_R}$

Thus our measurement strategy is as follows. We model, primarily using simulated events, the kinematics distributions of the Standard Model background. We also model the kinematic distributions of our W' signal using simulated events. These depend upon the W' mass assumed, so multiple simulations are needed to cover the 300 to 950 GeV/c^2 mass range. Finally, we use the $M_{t\bar{b}}$ distribution in data to measure the

signal contribution. This can be translated into a 95% C.L. upper limit on the $W' \rightarrow t\bar{b}$ cross-section. The measurement technique is complex because we must properly include the uncertainties in our background model; a simple fit will not do. The final chapter discusses the implication this result has for a W' -like signal of arbitrary coupling strength.

5.2 W' Simulation

The simulation of various background processes was detailed in the previous chapter; W' events are analogous. We use PYTHIA for both the event generation and parton showering. Again we assume signal with no interference with the Standard Model W boson. Because the resulting kinematics depend on the assumed mass of the signal, we must produce multiple simulations. The lowest W' mass we consider is $300 \text{ GeV}/c^2$; below this value it is difficult to distinguish our signal from the Standard Model W boson and interference cannot be ignored. The highest mass we consider is $950 \text{ GeV}/c^2$; Tevatron collisions typically do not exchange enough momentum to produce more massive particles and we do not expect to see such rare events in a dataset this size. Each $W' \rightarrow t\bar{b}$ simulation was used to generate 140k events; they include the following W' masses: 300, 400, 500, 600, 650, 700, 750, 800, 850, 900, and $950 \text{ GeV}/c^2$.

5.3 Selecting a Kinematic Distribution

We want to identify the kinematic distribution most sensitive to the presence of signal, one which shows a W' signature. We consider a number of possible candidates. The simplest is the E_T of the b -tagged jet. $W' \rightarrow t\bar{b}$ decay follows the two-body formula, which states that the energy of the b -quark in the W' rest frame is:

$$E_b = \frac{M_{W'}^2 + M_b^2 - M_t^2}{2M_{W'}} \approx \frac{1}{2}M_{W'}. \quad (5.1)$$

Because the massive W' is produced nearly at rest, the W' rest frame is approximately the lab frame. Thus we expect to observe a very energetic b -jet, with nearly half the energy of the W' mass.

One could also use the E_T distribution of the lead jet. The b -tagged jet typically has the highest energy, so this distribution is highly correlated. The shapes of these distributions, as well as others, are compared in Figure 5.1. The energetic nature of the W' decay products makes almost any jet or energy variable somewhat useful. There are also a range of mass variables to consider: the W boson mass, the sum of the W and lead jet, the sum of including all jets, and so on. The W' contribution leads to a peak in the tail of these distributions.

Linear combinations of these variables in which the coefficients are optimized for maximum signal separation are also promising candidates. These offer the best overall sensitivity, but the gain is too small to compensate for their time-consuming and cumbersome implementation. For the other mass and energy distributions, comparison of the expected sensitivity (using our measurement technique described later) shows that $M_{t\bar{b}}$ is best over the full range signal masses.

5.4 $M_{t\bar{b}}$ Distribution

The natural variable for searching for a massive, short-lived particle which decays via an s -channel process (Figure 1.3) is the total invariant mass. Our signal hypothesis assumes $W' \rightarrow t\bar{b} \rightarrow \ell\nu b\bar{b}$, so $M_{W'}$ is approximately the mass constructed from the detected jets, lepton, and \cancel{E}_T . We denote this quantity as $M_{t\bar{b}}$. Figure 5.1 shows these inputs and the increased separation gained by forming $M_{t\bar{b}}$. The goal of this analysis is to measure this distribution in data for anomalous contribution indicative of W' .

There are several possible variations in $M_{t\bar{b}}$ construction that must be considered:

whether to include the third tight jet in the 3 jet bin, whether to include any loose jets, how to treat the unmeasured P_z of the neutrino, and so on. Our event selection includes the 3-jet bin because simulated W' events often have an additional jet that originates from initial or final-state gluon radiation (Chapter 6). For examples, simulation of $800 \text{ GeV}/c^2$ W' events show that forty percent of them have an extra jet. The initial state radiation occurs before W' production, and including the extra jet will lead to some mis-reconstruction of the W' mass. Our sensitivity studies show that it is best to exclude the jet of lowest energy $W+3$ jet events. For this reason we assume the two leading jets are from the b -quarks in the $W+3$ jet bin. The same reasoning also explains why including loose jets does not add any additional sensitivity.

5.4.1 Solving for P_z^ν

The transverse neutrino momentum is assumed to be the \cancel{E}_T , but the longitudinal component P_z^ν is not measured. If we constrain the mass of the Standard Model W to be $80.403 \text{ GeV}/c^2$ [6], we can solve the resulting quadratic equation for P_z^ν . In the case of complex solutions (when the transverse mass sums to more than the total mass constraint), we assign P_z^ν to the real part. If both solutions are real, we use the solution with the smaller absolute value. The W' simulation indicated this approach was most accurate even for very massive W' events. The best P_z^ν solution was chosen 62-69% of the time, depending on W' mass.

In summary, we solve for the neutrino momentum and define $M_{t\bar{b}}$ as the reconstructed mass of the W boson and two leading jets, corrected to Level 7. Figure 5.2 contrasts the shape of the $t\bar{b}$ distribution between signal and background for $W+2$ jet events. Several W' masses are shown, illustrating how for small masses the signal becomes similar to background and for large masses the signal contribution piles up in the overflow bin. This

is why we only expect our measurement to be sensitive in the 300 to 950 GeV/ c^2 W' mass range. Our models for $M_{t\bar{b}}$ are truncated at 700 GeV/ c^2 by an overflow bin. This is necessary because some of the background components do not contain sufficient statistics to fully determine the shape of the distribution at larger values.

5.5 Measuring the Signal Contribution

In order to determine the presence of new physics, it is not sufficient to simply search for a feature characteristic of the signal. One must also determine the likelihood of producing this characteristic by standard physics alone. For example, suppose I claim I can predict coin flips and successfully do so three consecutive times. Before anyone is confident in my psychic powers, they should note that there is a one in eight chance of doing this simply by guessing. The scientific method requires comparing the likelihood an observation is consistent with new physics to the likelihood that it is consistent with known physics.

Our signal is expected to appear as an excess in the tail of the $M_{t\bar{b}}$ distribution. We must quantify the probability of W' producing any discrepancy observed in the data to the probability that it is simply a fluctuation in the Standard Model prediction. We measure these likelihoods using two hypotheses: the null hypothesis (H_B) consisting only of the background model, and the signal plus background hypothesis (H_{S+B}) comprised of background plus a specified W' contribution. If the ratio of the likelihoods of these hypotheses, known as CL_s , is sufficiently small, we can exclude the presence of signal. This is the heart of our measurement technique, known as the frequentist approach [40].

5.5.1 Setting W' Limits with CL_s

The figure of merit, CL_s [41], is given by the probability of H_{S+B} fluctuating to match the data divided by the probability of H_B fluctuating to match the data. These probabilities, P_{S+B} and P_B , cannot be determined without first incorporating uncertainties

(detailed in Chapter 6) into our hypotheses. This is done by repeatedly varying all the uncertain simulation parameters. Each parameter is randomly sampled from a Gaussian centered on the nominal value with a width set by the estimated uncertainty. Generating a collection of $\sim 25\text{k}$ such distributions is sufficient to map out the space of predictions consistent with that hypothesis. It is impractical to repeatedly run all the signal and background simulations with new sets of parameters; instead we individually simulate $\pm 1\sigma$ variations for each parameter. These are used to extrapolate or interpolate the changes expected for an arbitrary parameter variation; the results from each parameter are compounded together for the overall variation [42].

Each of these distributions is fit to the default H_B and H_{S+B} predictions; the same is done for data. We vary the normalization of each background component to minimize the overall χ^2 fit [43]. The normalizations are varied independently, treating the likelihoods as Gaussians with widths determined by their uncertainty (Table 4.4). The preferred hypothesis is quantified by: $\chi^2(\text{Data}|H_{S+B}) - \chi^2(\text{Data}|H_B) \equiv \Delta\chi^2$. The probability of H_B fluctuating to match the data is then given by the fraction of the H_B ensemble with a larger $\Delta\chi^2$ larger than in data; H_{S+B} is similar. These definitions are illustrated in Figure 5.3. Thus we define CL_s as:

$$CL_s = \frac{P_{S+B}(\Delta\chi^2 \geq \Delta\chi_{Data}^2)}{P_B(\Delta\chi^2 \geq \Delta\chi_{Data}^2)}. \quad (5.2)$$

In summary, the measurement of CL_s quantifies our confidence that the data prefers the signal hypothesis. We set an upper limit on the amount of signal present by iteratively increasing the $W' \rightarrow t\bar{b}$ cross-section assumed in H_{S+B} until CL_s is arbitrarily close to 0.05. This defines the 95% C.L. upper limit on the cross-section for a SM-like W' . This procedure is repeated using the model for each W' mass from 300 to 900 GeV/ c^2 .

5.5.2 Grouping of Background Components

In order to reduce the number of parameters that must be varied simultaneously in our χ^2 calculations, background processes producing similar $M_{t\bar{b}}$ distributions are grouped together. The processes in each of the five groups are summed according to expected contribution. The total normalization uncertainty determined by adding the various individual uncertainties in quadrature, which is slightly conservative because it neglects some correlations. The binning of the resulting $M_{t\bar{b}}$ distributions is set such that each bin, including the final overflow bin, has sufficient statistics to give a smooth shape.

We have five composite background distributions: W +bottom, W +charm, mistag/non- W , $t\bar{t}$, and single-top. Table 5.2 shows the composition of each grouping and Figure 5.4 shows their $M_{t\bar{b}}$ distributions. WZ and Z +jets are grouped with $Wb\bar{b}$ because Z bosons can decay via bottom quarks; similarly WW is grouped with charm processes because decays via cs are more common. Mistags and non- W are rather distinct kinematically, but the non- W histogram has too few statistics (Figure 5.4) to be kept separate. We group it with mistags because both have very long tails, and thus have similar shapes in the high-mass signal region.

BG Component	BG Processes Within
W +bottom	$Wb\bar{b}$, WZ , Z +Jets
W +charm	$Wc\bar{c}$, Wc , WW
$t\bar{t}$	$t\bar{t}$ (dilepton), $t\bar{t}$ (lepton+jets)
Mistag/Non- W	Mistagged W +lf, Non- W
Single Top	Single Top (s-channel), Single Top (t-channel)

Table 5.2: Background processes are combined into five components.

5.5.3 Fitting Channels in Parallel

As shown in Table 5.1, the signal-to-background ratio (which drives the overall sensitivity) varies depending on the channel: 2 jets 1 b -tag, 3 jets 1 b -tag, 2 jets 2 b -tags, and

3 jets 2 b -tags. The data in these channels, along with our nominal background models, are shown in Figure 5.5. No major discrepancy is apparent. The overall sensitivity to signal can be improved by fitting all four channels in parallel, preserving the sensitivity of the best bins rather than mixing them together. The multi-channel fit is performed using the same parameter variations and minimizing the χ^2 summed across all channels:

$$\Delta\chi_{total}^2 = \Delta\chi_{2J1T}^2 + \Delta\chi_{3J1T}^2 + \Delta\chi_{2J2T}^2 + \Delta\chi_{3J2T}^2.$$

5.6 Expected Limits

We can determine the upper limit on the $W' \rightarrow t\bar{b}$ cross-section we expect to set by substituting the null hypothesis H_B into the CL_s calculation in place of the data. This technique is useful for characterizing our expected sensitivity. We can see how changes to our event selection or modeling affect the anticipated result. This was the basis for selecting the $M_{t\bar{b}}$ distribution and not including additional jets.

We examine how the individual channels contribute to the overall expected sensitivity. Figure 5.6 shows that most of the sensitivity comes from the 2 jets 1 b -tag channel; we expect the best sensitivity here because it has the largest W' component and there is little contamination from top production. The 3 jet channels have more $t\bar{t}$ background, so that the $M_{t\bar{b}}$ distribution is more similar to signal. The double b -tag channels have a better signal-to-background ratio than in single tags, but contain too few events to provide much sensitivity to small excesses in the mass.

Another useful check for consistency is to compare the expected results using only electrons and muon events. The sensitivities will not be the same because we do not have the same number of events for each lepton type. The results are shown in Figure 5.7. From this plot we conclude that using loose muons clearly improves our expected result. This is because the large \cancel{E}_T cut used in that trigger tends to select more energetic (and

thus signal-like) events.

The next chapter discusses how our expected 95% C.L. upper limits on the $W' \rightarrow t\bar{t}$ cross-section are affected by the various sources of uncertainty in the simulation.

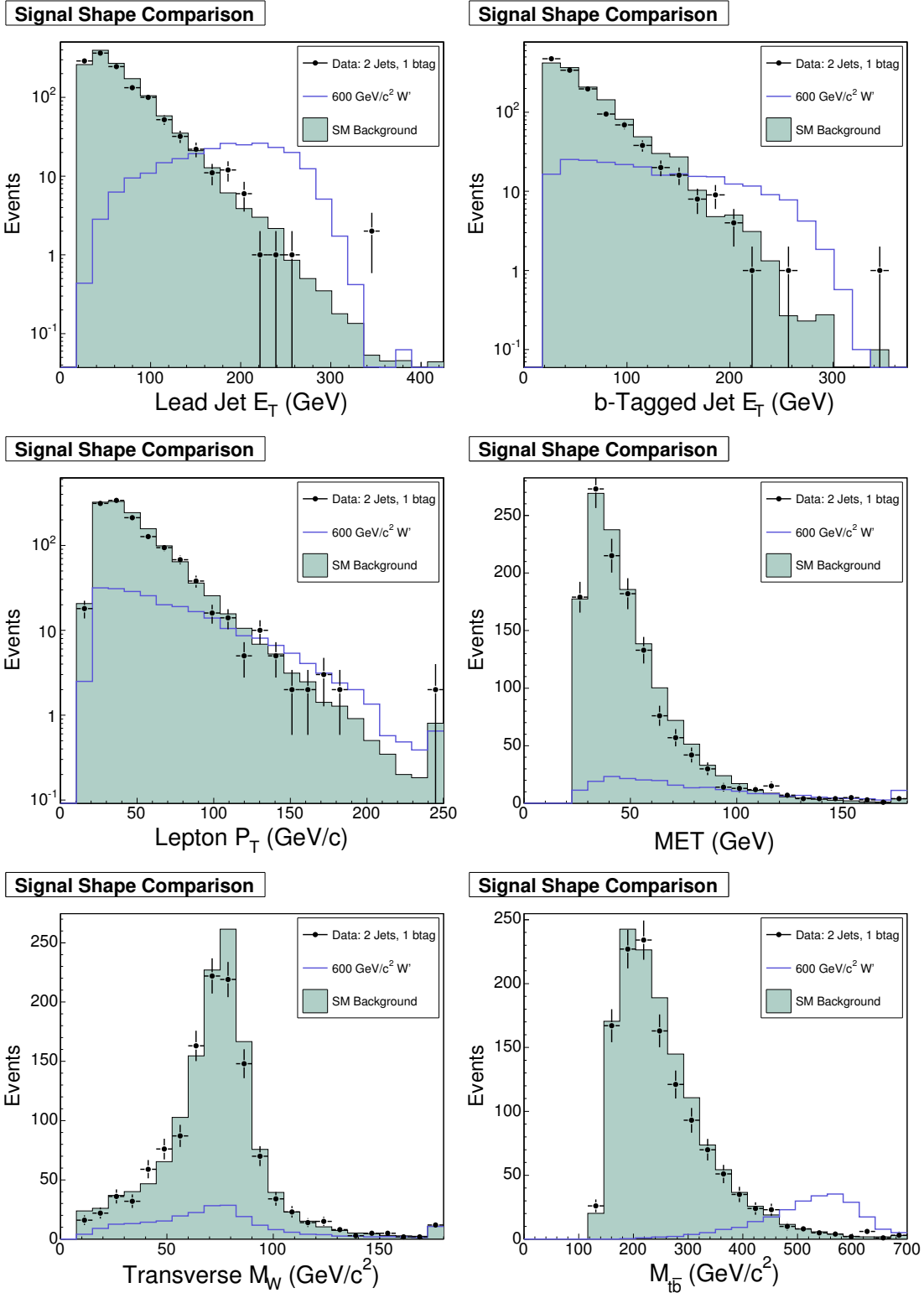


Figure 5.1: Comparison of various signal distributions. The $M_{t\bar{b}}$ distribution is shown to have separation from background superior to its individual inputs.

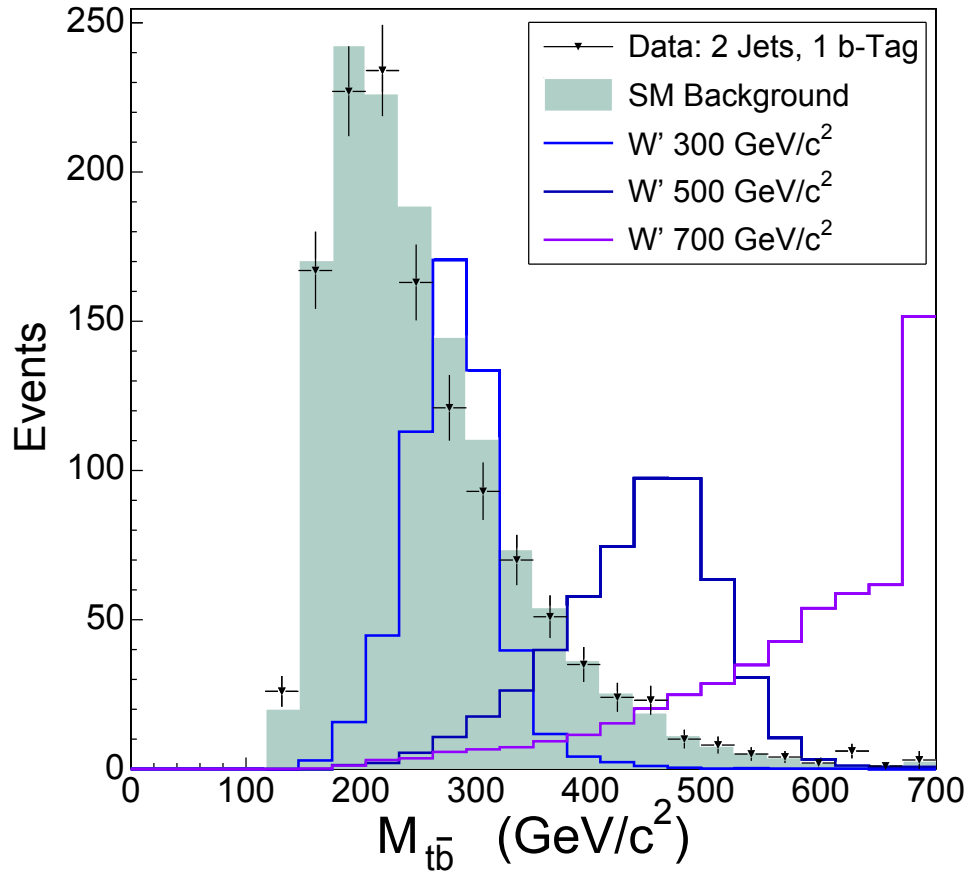


Figure 5.2: Comparison of the $M_{t\bar{b}}$ distribution shape in signal and in background. Models for several different W' masses are shown, set to arbitrary normalization.

Pseudo-data Distribution for H_B and H_{S+B}

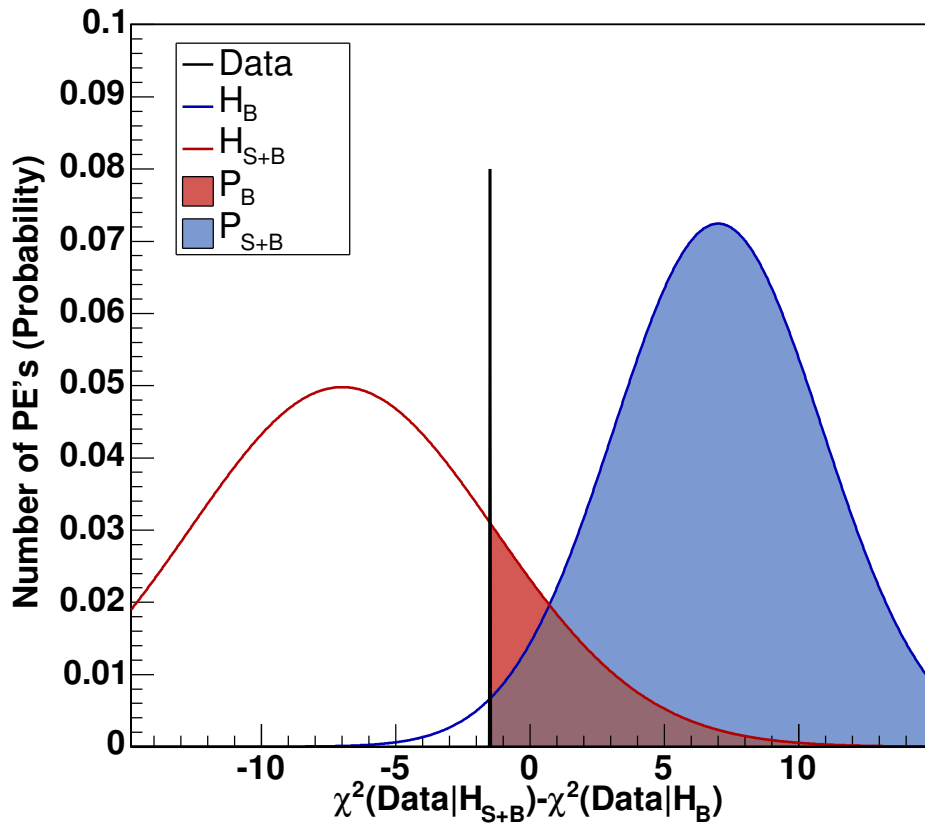


Figure 5.3: This figure shows how P_{S+B} and P_B are determined by plotting $\chi^2(\text{data}|H_{S+B}) - \chi^2(\text{data}|H_B)$ for ensembles of H_{S+B} pseudo-experiments and H_B pseudo-experiments. CL_s is the ratio of P_{S+B} (blue area) to P_B (red area).

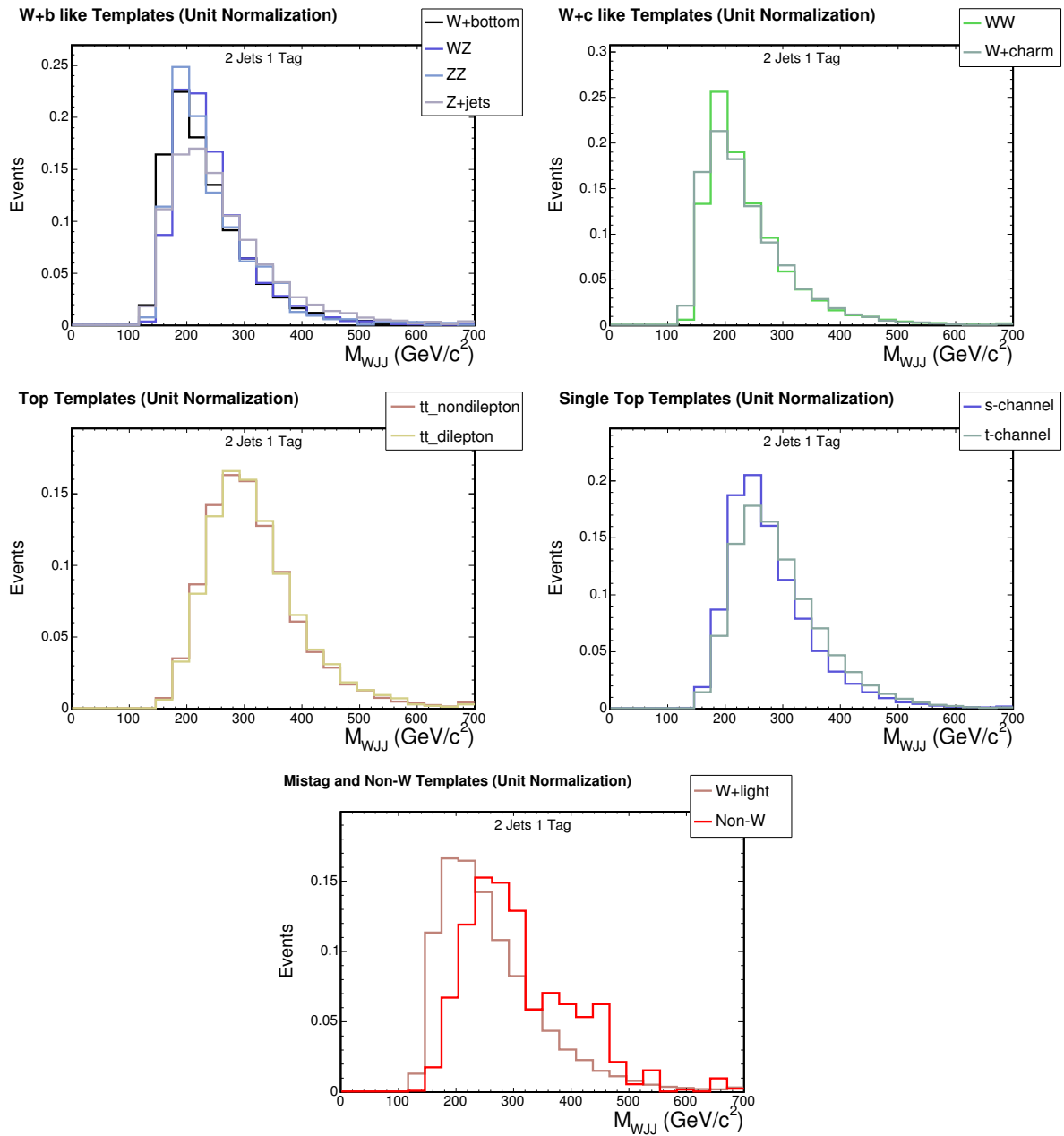


Figure 5.4: Comparison of the background shapes (normalized to unit area) in each grouping.

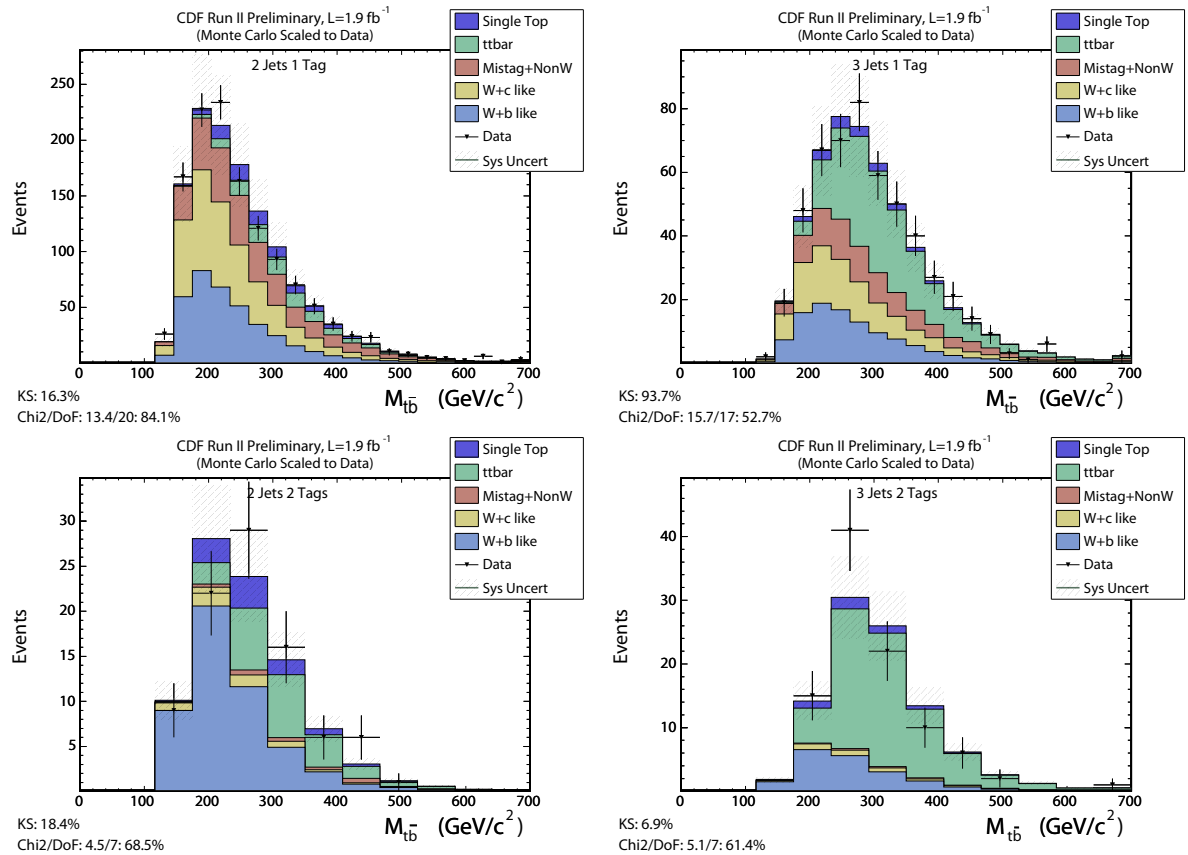


Figure 5.5: Comparison of the $M_{t\bar{t}b\bar{b}}$ distribution in data to background expectation. Channels are separated according to the number of jets and b -tags. No large discrepancy is apparent.

95% C.L. Expected Limits by Channel

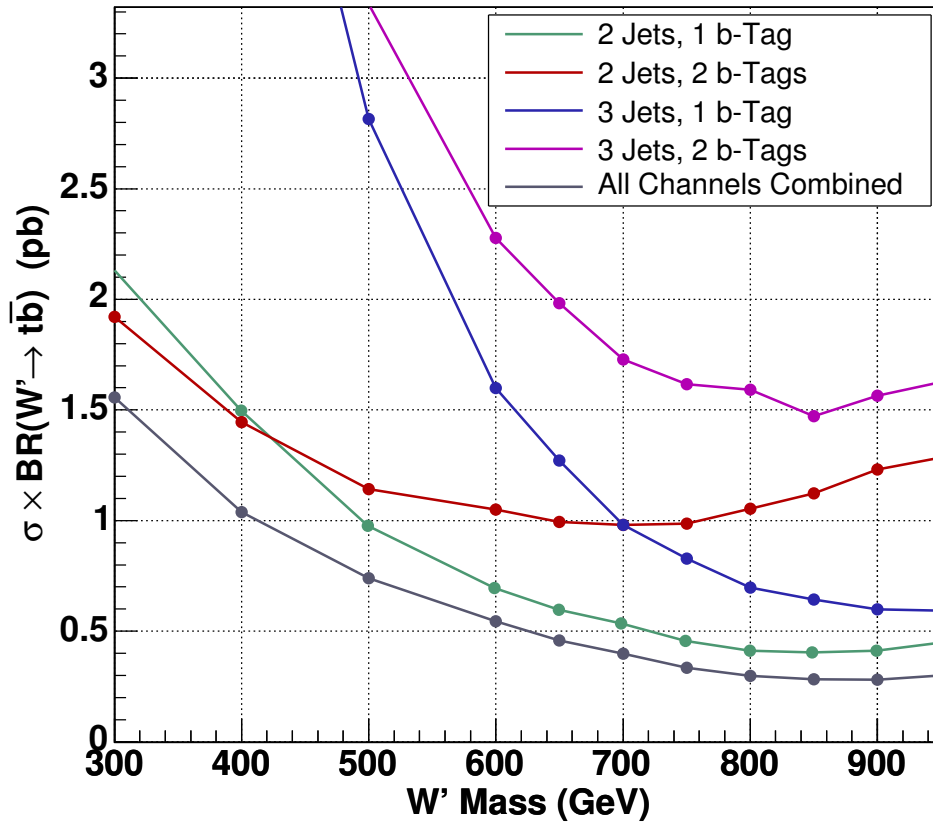


Figure 5.6: Expected 95% C.L. upper limits for each channel individually. The 2 jet 1 b -tag channel, with its small top fraction, is the most sensitive.

95% C.L. Expected Limits By Lepton Type

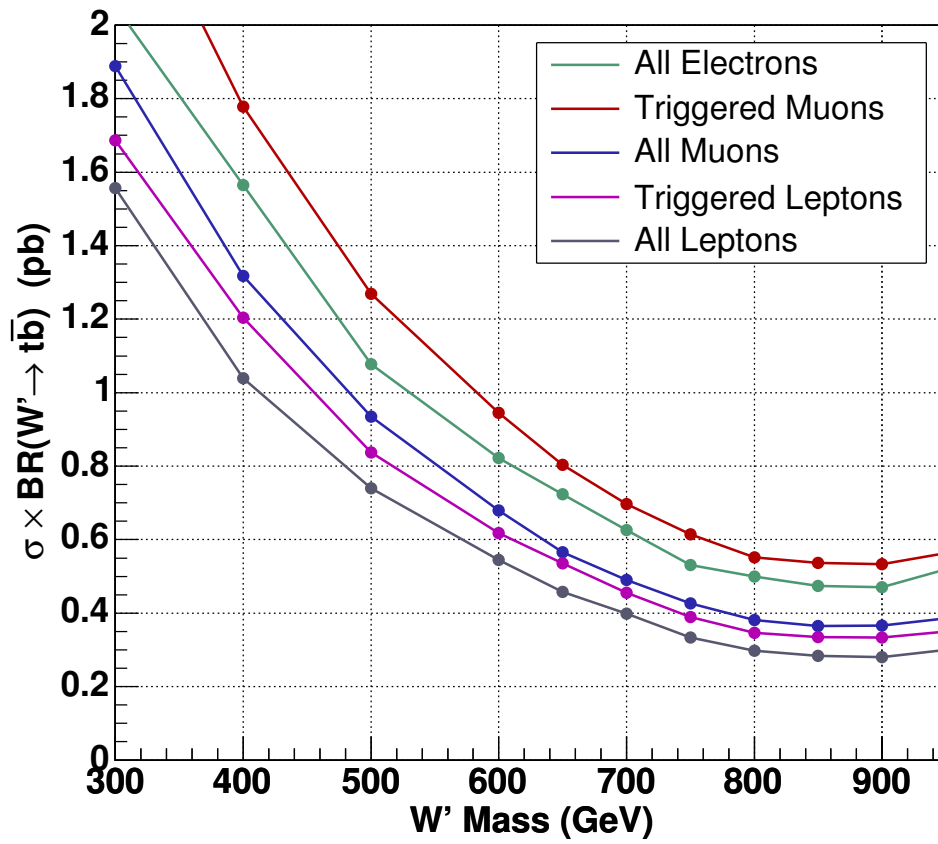


Figure 5.7: Comparison of expected 95% C.L. upper limits among various lepton types.

CHAPTER 6

Systematic Uncertainties

This analysis is fundamentally a comparison of data to the Standard Model prediction. Discoveries can only be made when discrepancies are statistically significant compared to the precision of the measurement. This requires detailed knowledge of the degree of uncertainty in our predictions.

The simulations of data are inexact: the responses of the various detector components are not perfectly known, the distributions of the incident partons are uncertain, the Feynman diagrams involved are approximated at leading order or next-to-leading order, and various other small background effects are approximated or neglected. These give rise to systematic uncertainties which, unlike statistical uncertainty, are independent of the size of the dataset.

Sources of systematic uncertainty can affect our $M_{t\bar{b}}$ prediction in two ways: they may alter the shape of the distributions, and they may alter the acceptance rates (and thus overall normalization) of the distributions. Some systematic uncertainties alter both.

As discussed in Chapter 5, our signal and background hypotheses include uncertain parameters by randomly sampling their values during many repeated trials, so as to map out the full space of possible predictions. The variations of these parameters are confined to Gaussian distributions with widths set by the estimated uncertainties. Rather than

rerun all the signal and background simulations for each possible set of parameters, we simulate $\pm 1\sigma$ variations for each parameter individually, such that all other variations can be extrapolated or interpolated. Thus our measurement requires we quantify each parameter's uncertainty with an initial estimate of the $\pm 1\sigma$ variations.

Types of systematic uncertainty for each background are shown in Table 6.1, and are explained in detail below. Full treatment of systematic uncertainties slightly worsens our expected 95% C.L. upper limits on the signal cross-section. For W' masses above $800 \text{ GeV}/c^2$, the upper limit goes from 0.2 pb to 0.3 pb as shown in Figure 6.1.

Background	Rate Uncertainties	Shape Uncertainties
W +bottom	JES, Lum, Acc_{Lep} , $\text{Acc}_{W+\text{bottom}}$	JES, Q^2
W +charm	JES, Lum, Acc_{Lep} , $\text{Acc}_{W+\text{charm}}$	JES
$t\bar{t}$	JES, Lum, Acc_{Lep} , $\text{Acc}_{t\bar{t}}$	JES
mistag/non- W	JES, Lum, Acc_{Lep} , $\text{Acc}_{\text{mistag/non-}W}$	JES, Mistag, Non- W
single top	JES, Lum, Acc_{Lep} , $\text{Acc}_{\text{single top}}$	JES
W'	JES, Lum, Acc_{Lep} , PDF, ISR, FSR, b -tag SF	JES, ISR, FSR, b -tag SF

Table 6.1: Sources of systematic uncertainty for each background process

6.1 Jet Energy Scaling

The dominant source of uncertainty arises from the hadron calorimetry. The underlying processes that produce a jet are diverse and modeling the detector response is complicated. An overall jet energy scale (JES) uncertainty arises when correcting the raw energy deposited in the calorimeter back to the energy of the incident parton. These corrections, mentioned in Chapter 3, give rise to associated uncertainties:

- Level 1 (η -Dependence): This uncertainty, also called the relative uncertainty, comes from correcting for the non-uniformity of the detector over its full η -range
- Level 2: No longer used
- Level 3: No longer used

95% C.L. Expected Limits Including Various Systematics

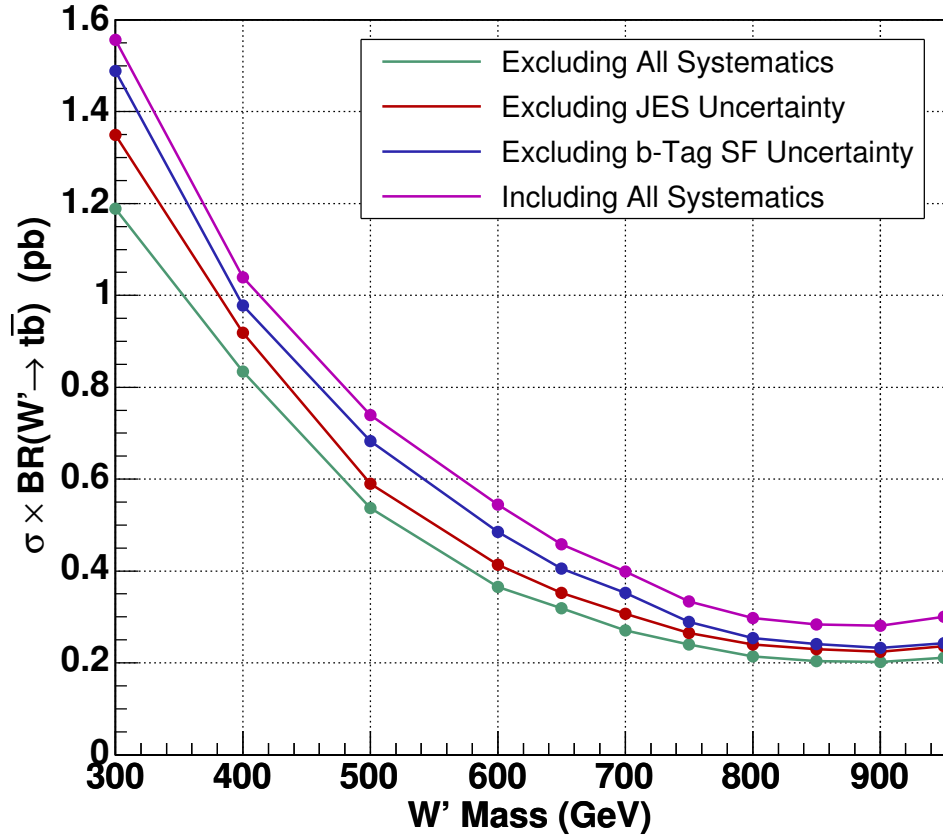


Figure 6.1: Expected sensitivity including various systematic uncertainties.

- Level 4 (Multiple Interactions): This correction has a negligible uncertainty
- Level 5 (Absolute): This uncertainty pertains to the energy lost in the gaps between towers
- Level 6 (Underlying Event) This uncertainty pertains to how energy is partitioned among the partons, including those not directly involved in the collision
- Level 7 (Out-of-Cone): This is the uncertainty concerning the amount of energy a jet deposits outside a cone of $\Delta R < 0.4$
- Level 8 (Splash-Out): This is an uncertainty not associated with a correction. It

pertains to the uncertainty in energy leakage beyond $\Delta R = 1.3$, the maximum extent of the out-of-cone correction.

The overall uncertainty of a jet's energy is determined by calculating $\pm 1\sigma$ variations for each of the individual energy corrections then summing the results in quadrature. By doing this for all jets, our simulation produces a $M_{t\bar{b}}$ distribution in which the overall jet energy scale differs by $+1\sigma$ or by -1σ . Arbitrary variations can be interpolated/extrapolated from the nominal and $\pm 1\sigma$ distributions. Thus if a randomly varied trial has a JES parameter of -0.4σ , the $M_{t\bar{b}}$ distribution is determined by interpolation between the -1σ and nominal background histograms.

Changes in the JES affect both the normalization and shape of each background component. Rates are affected because jet selection includes a cut on the energy; thus jets with their energy scale increased up are more likely to pass our selection, and vice versa. Similarly, the jet energy directly contributes to the calculation of $M_{t\bar{b}}$, so varying the jet energy will change the shape of the $t\bar{b}$ distribution also. We do not extrapolate JES variations beyond $\pm 3\sigma$ to prevent unbounded behavior.

JES affects all our simulations, thus we create $\pm 1\sigma$ JES alternatives for each signal and background distribution. The JES effect on each background is illustrated in Figures 6.2 and 6.3. JES is the source of our largest systematic uncertainty, individually accounting for half of the total sensitivity lost by including systematic uncertainties (Figure 6.1).

6.2 *b*-tag Scale-Factor Uncertainty

Some *b*-hadrons decay into a lepton and a lighter hadron. Because the decay products are substantially lighter in mass, the lepton is produced with large momentum. By counting jets which have a non-isolated electron or muon with large P_T , one can estimate the fraction of *b*-jets events. The *b*-tagging efficiency of the `SecVtx` algorithm is deter-

mined by measuring this fraction in b -tagged data. By grouping jets according to E_T and measuring the b -tagging efficiency in each group, a slight energy dependence is observed [44].

Our simulations do not perfectly model the b -tag efficiency and its jet E_T dependence. A b -tag scale-factor corrects this by weighting each event appropriately. This scale-factor has an associated uncertainty that is only well determined at low energy.

When a W' decays to $t\bar{b}$, the b -quark generally has an energy equal to half the W' rest mass, produces a jet spectrum far more energetic than Standard Model processes such as $t\bar{t}$ pair production. The leading jet E_T spectrum for W' of $900 \text{ GeV}/c^2$ is shown in Figure 6.4, with average energies far above those where the scale-factor is measured (Figure 6.5). Thus it is ambiguous what the scale-factor should be for our W' simulations. Even the slope of the E_T dependence is unclear.

Our technique for approximating this scale-factor is to linearly extrapolate to high energy the error band from the most recent scale-factor measurement (Figure 6.4). We weight events according to $1 + 0.0005 E_T^{J_1}$ for a $+1\sigma$ variation in the scale factor and according to $1 - 0.0015 E_T^{J_1}$ for a -1σ variation. This alters both the rate and shape of the $M_{t\bar{b}}$ distribution from signal. For events with two b -tags, the per-jet weights are combined via $(1 - 0.0015 E_T^{J_1}) \cdot (1 - 0.0015 E_T^{J_2})$. The nominal scale-factor is chosen to be 0.95 for jets of all E_T .

As with JES, we use the nominal and $\pm 1\sigma$ varied $M_{t\bar{b}}$ distributions to seed the extrapolation of signal distributions with arbitrary variation. We truncate the range of the b -tag scale-factor variation at $\pm 1\sigma$ to avoid large shape extrapolations. The b -tag scale factor variations are shown in Figure 6.5.

As shown in Figure 6.1, this systematic uncertainty has a large impact on our overall sensitivity, though not as severe as JES. For average jets from a $300 \text{ GeV}/c^2$ W' , this is

a fourteen percent uncertainty. For average jets from a $950 \text{ GeV}/c^2$ W' , this is a forty percent uncertainty. A technique to measure the b -tag scale factor at high energy will be needed to conduct future searches for a massive particle which decays via b -jets.

6.3 Initial and Final State Radiation

Gluons may be radiated from a parton either before or after a collision. These gluons often produce one or more additional jets, such that W' decays often end up in the $W+3$ jet channel. There is substantial uncertainty in the ability of our simulations to properly predict the amount of ISR and FSR. This is most significant in our signal distribution; we neglect the impact on background processes. We create alternate W' distributions in which the radiative parameters have been increased or decreased. The uncertainties affect both the rate and shape of $M_{t\bar{b}}$ distribution from background through changes in jet-energy distribution. The increments have been selected to approximate variations of 1σ . Thus we produce signal distributions that are varied $\pm 1\sigma$ in ISR and signal distributions varied $\pm 1\sigma$ in FSR. These histograms are shown in Figure 6.7. They seed the extrapolation of distributions with arbitrary variation in ISR and FSR, which is restricted to $\pm 1\sigma$.

6.4 Signal Acceptance

6.4.1 Integrated Luminosity

The instantaneous luminosity at CDF is measured based upon the intensity of Čerenkov radiation near the interaction region. There is a 6% uncertainty in the scaling of this quantity [45], which directly leads to a 6% uncertainty in the integrated luminosity of our dataset. This applies to all signal and background distributions.

6.4.2 Lepton Acceptance

The efficiency of lepton selection for simulated events differs slightly from data. There is a small uncertainty in the scale factor used to correct this. The uncertainty is trigger dependent and ranges from 0.6% for the CEM electron to 2.2% for loose muon selection [46]. For simplicity we add an overall 2.0% uncertainty to the normalizations of all our background components. The lepton P_T spectrum for signal events is more energetic than for background, but still similar enough that we apply the same 2% uncertainty.

6.4.3 Parton Distribution Functions

As mentioned in Chapter 4, PDF's describe the momentum distribution among the various quarks and gluons within the proton and antiproton. These are used by event generators to determine the initial kinematics of simulated events. Altering the PDF functions will alter the resulting dynamics, particularly the momentum transfer (Q^2) in the W' simulation. There exist various PDF's based on fits to data from different particle collider and fixed-target experiments [24]. We use only a single PDF set called CTEQ5L, which is a significant source of uncertainty for our signal simulation.

Our uncertainty could be determined by comparing W' simulations with different PDF sets. This is not practical because there are at least 46 alternatives and this would be too time consuming. The alternative is to take each event in our current simulation and weight it by the likelihood of it occurring in one of the alternative sets. This likelihood is calculated based on the Q^2 and how that momentum is initially distributed (x_1, x_2) [47].

We calculate the set of comparative weights for each event in a subset of the data. By summing each set weights across all the events passing our selection, we determine the expected change in acceptance. This gives an overall PDF uncertainty of four percent for the largest W' masses, which we quote in our current analysis. All W' simulations are

assumed to have a four percent rate uncertainty from PDF.

The uncorrelated integrated luminosity, lepton acceptance, and PDF uncertainties are added in quadrature for a 7.5% overall uncertainty in signal acceptance. These parameters are similarly varied within a Gaussian constraint.

6.5 Background Acceptance

Chapter 4 describes the technique used to obtain predictions for the normalization of each background component. Sources of uncertainty for the background calculations include: electroweak cross-section uncertainty, non- W fit uncertainty, heavy-flavor k-factor uncertainty (which itself comes from sources such as factorization scale), b -tag scale factor uncertainty, lepton ID uncertainty, and integrated luminosity uncertainty.

The resulting rate uncertainties are shown in Table 4.4. The uncertainty for each background group neglects the anti-correlations between any components in that grouping by simply summing their uncertainties in quadrature. Each of the five background groups is assigned a normalization parameter which is varied according to the overall uncertainty.

6.6 ALPGEN Q^2 Scale

There is an additional source of uncertainty from using our ALPGEN simulation to model W +jets. The choice of factorization and renormalization scale in the model's perturbative QCD calculation impacts Q^2 . The discrepancy with data is most severe in the $Wb\bar{b}$ simulation; we consider the effect in $Wc\bar{c}$ and Wc to be negligible. The mistag model uncertainty (below) subsumes any Q^2 dependence in W +lf simulation.

To estimate the uncertainty arising from ALPGEN the Q^2 scale, we create alternate simulations for $Wb\bar{b}$ in which the Q^2 scale is doubled and in which it is halved. This uncertainty only affects the resulting $M_{i\bar{i}}$ shape: the distributions have the same normal-

ization (Figure 6.8). These alternative distributions are treated as $\pm 1\sigma$ variations, and the range of the Q^2 variation is constrained to $\pm 1\sigma$.

6.7 Mistag and Non- W Modeling

As discussed in Chapter 4, our mistag model is based on $W+2p$ and $W+3p$. Jets in these events are not b -tagged, but are weighted by their mistag probability. There are several other techniques for modeling this background, introducing an uncertainty in our mistag model.

We quantify this uncertainty using pretag data to obtain an alternative $M_{t\bar{b}}$ distribution. Pretag data is enriched with $W+1f$ events and avoids some of the artifacts potentially introduced via event simulation. Using data in which events are negatively tagged (i.e. the jet vertex is displaced in the wrong direction to be from an actual b -decay) is also a possible alternative, but does not provide sufficient statistics to populate our distribution. The pretag data is considered a 1σ mistag model variation.

Due to the small non- W fraction remaining after our QCD veto, we do not expect to be sensitive to changes in the non- W model. Nonetheless, we estimate the possible uncertainty from our model by substituting the non-isolated electron data in place of the anti-electron data (discussed in Chapter 4), using this as a 1σ variation in the shape of our non- W model.

We only use a single alternative mistag model and a single alternative non- W model; these are shown in Figure 6.9. As before, the range of variation for these modeling parameters is truncated to $\pm 1\sigma$ to avoid the problem of unbounded shape extrapolation.

6.8 Top-Quark Mass

Our signal and background models assume a top-quark mass of $175 \text{ GeV}/c^2$, as do our upper limit calculations. We quote our result for this mass; it is not a source of systematic uncertainty. The current world-average top mass is slightly lower [6]; using it in our simulation would enhance the $W' \rightarrow t\bar{b}$ branching fraction. Thus our quoted result is slightly more conservative than one using the current top mass.

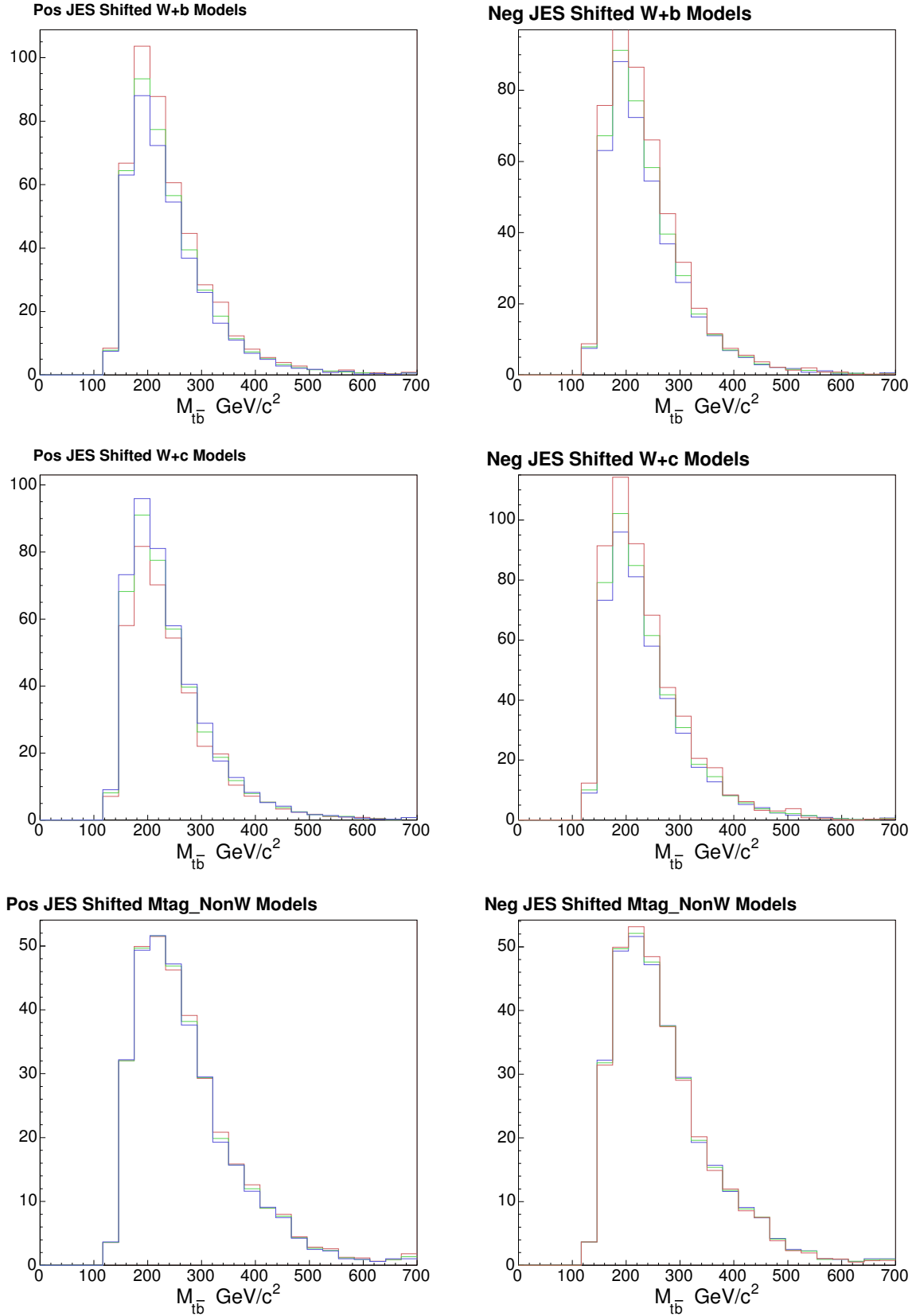


Figure 6.2: Comparison of the nominal background distributions (blue), 1σ JES varied background distributions (green), and 3σ JES varied background distributions (red). Positive variations are on the left and negative variations are on the right. 96

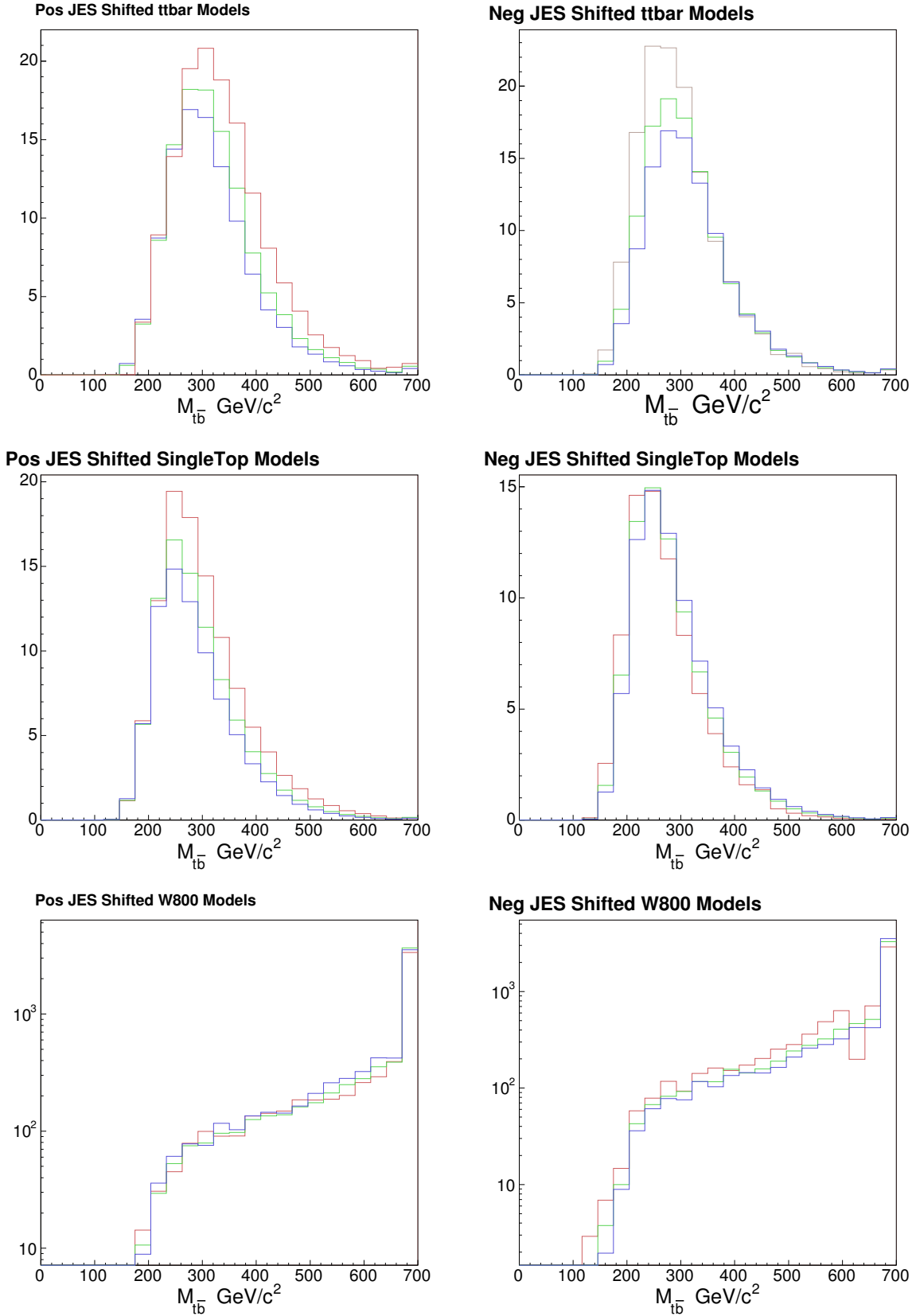


Figure 6.3: Comparison of the nominal background distributions (blue), 1σ JES varied background distributions (green), and 3σ JES varied background distributions (red). Positive variations are on the left and negative variations are on the right. 97

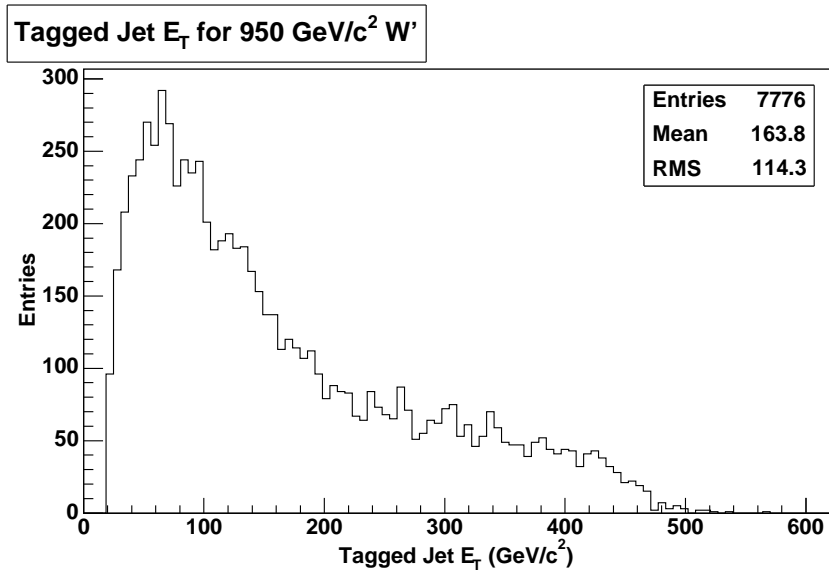


Figure 6.4: The lead jet E_T spectrum for W' of $950 \text{ GeV}/c^2$.

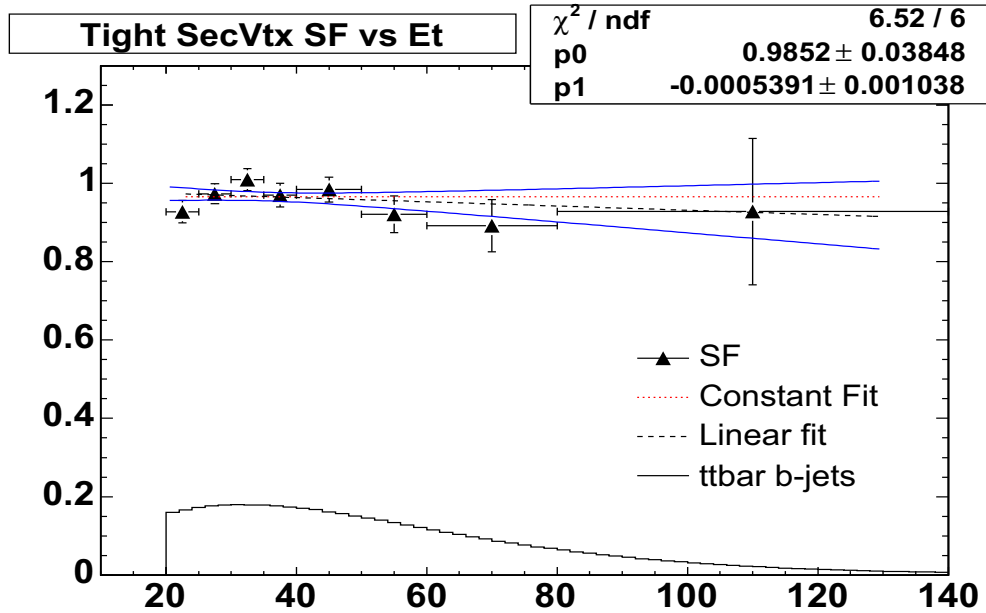


Figure 6.5: Current calculation for the b -tag scale factor [44]

Btag SF Shifted W800 Models

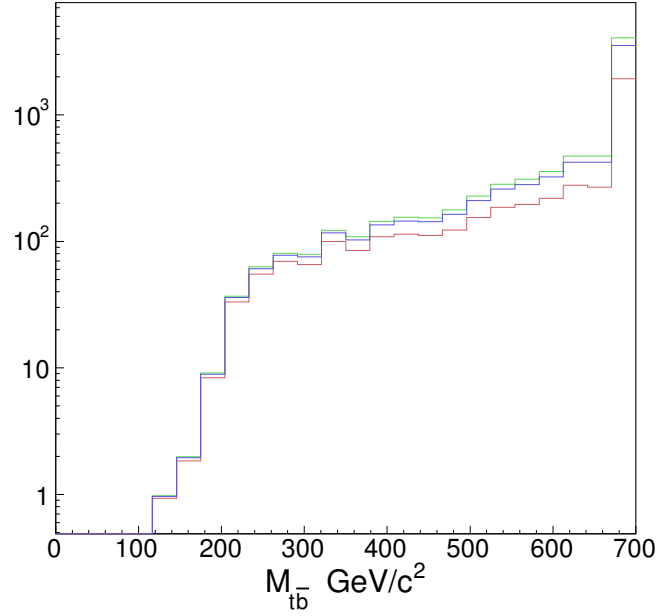


Figure 6.6: Comparison of the nominal $800 \text{ GeV}/c^2$ W' distribution (blue), $+1\sigma$ b -tag scale factor varied distribution (green), and -1σ b -tag scale factor varied distribution (red).

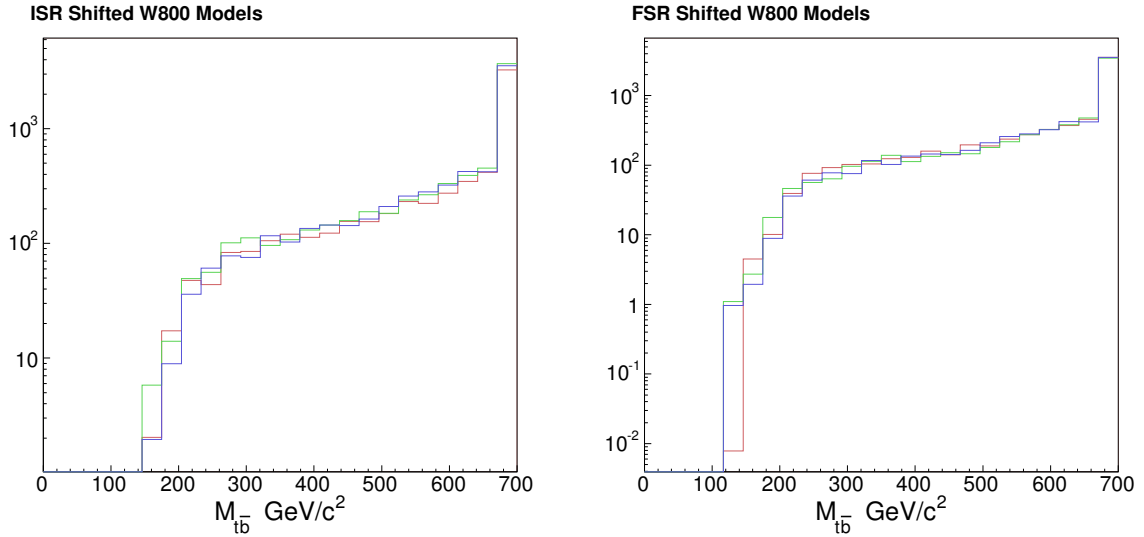


Figure 6.7: Comparison of the nominal $800 \text{ GeV}/c^2$ W' distribution (blue), $+1\sigma$ variation (green), and -1σ variation (red) for ISR (left) and FSR (right).

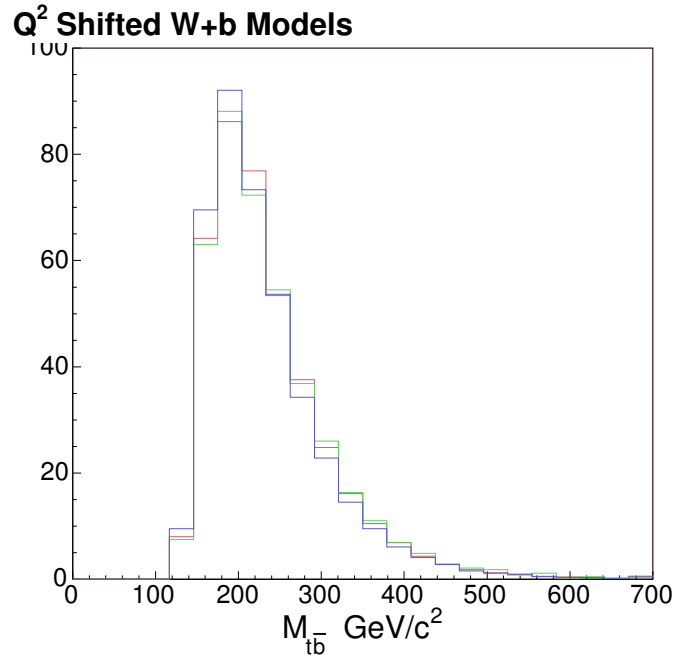


Figure 6.8: Comparison of the default W +bottom background distribution with nominal Q^2 scale (blue), alternative distribution with the Q^2 scale doubled (green), and the alternative distribution with the Q^2 scale halved (red).

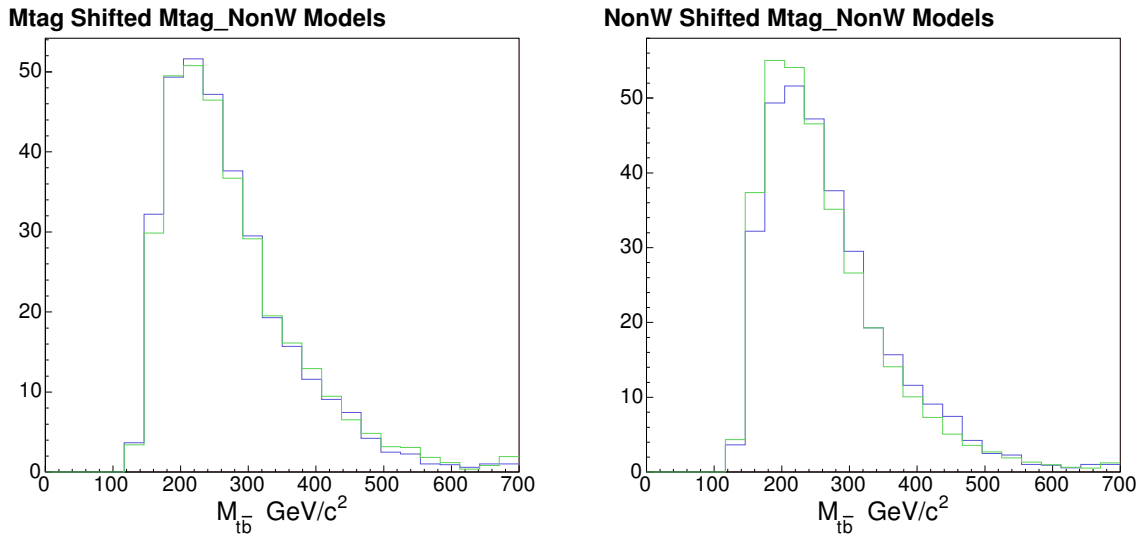


Figure 6.9: Comparison of the default mistag/non- W model (blue) and the $\pm 1\sigma$ variation (green) of the mistag model (left) and of the non- W model (right). For the mistag model variation we substitute pretag data, and for the non- W model variation we use non-isolated electron data in place of anti-electron data.

CHAPTER 7

Conclusion

We present a search for a narrow resonance in the $t\bar{b}$ mass spectrum using 1.9 fb^{-1} of $p\bar{p}$ collisions at $\sqrt{s} = 1.96\text{ TeV}$ recorded with the CDF II detector at the Fermilab Tevatron. We select events with a lepton, neutrino candidate, and two or three jets from which to construct the $t\bar{b}$ mass. We quantify the result using the model of a massive Standard Model-like charged-boson (W') decaying to $t\bar{b}$, but we are generally sensitive to the presence of any narrow state decaying to the third generation.

For a purely right-handed W' with Standard Model couplings, we set a new limit at 95% confidence of $\sigma(p\bar{p} \rightarrow W'_R) \times \text{BR}(W'_R \rightarrow t\bar{b}) < 0.28\text{ pb}$ and $M_{W'_R} > 800\text{ GeV}/c^2$. The limit increases to $M_{W'_R} > 825\text{ GeV}/c^2$ if decay to right-handed neutrinos is forbidden. These results are shown in Table 7 and plotted in Figure 7.1. The best prior search found $M_{W'} \geq 768\text{ GeV}/c^2$ if leptonic decays are forbidden [16].

For a simple W' model with effective coupling $g_{W'}$, the cross-section is proportional to $g_{W'}^4$. Relaxing the assumption of the universal weak coupling ($g_{W'} = g_W$), our cross-section limits can be rewritten as upper limits on $g_{W'}$ as a function of $M_{W'}$. This is relevant to both the right-handed W' model as well as a left-handed W' model in which the $W'_L - W$ interference is negligible. The excluded region of the $g_{W'} - M_{W'}$ plane is shown in Figure 7.2, with $g_{W'}$ in units of g_W . At $M_{W'} = 300\text{ GeV}/c^2$, we limit (95% C.L.)

$M_{W'}$ (GeV/ c^2)	Expected Upper Limit (pb)	Observed Upper Limit (pb)
300	$1.56^{+0.62}_{-0.45}$	1.59
400	$1.04^{+0.44}_{-0.30}$	1.17
500	$0.74^{+0.35}_{-0.22}$	0.84
600	$0.54^{+0.24}_{-0.17}$	0.44
650	$0.46^{+0.21}_{-0.13}$	0.39
700	$0.40^{+0.17}_{-0.12}$	0.32
750	$0.33^{+0.15}_{-0.09}$	0.28
800	$0.30^{+0.13}_{-0.09}$	0.26
850	$0.28^{+0.13}_{-0.08}$	0.25
900	$0.28^{+0.13}_{-0.08}$	0.26
950	$0.30^{+0.13}_{-0.09}$	0.28

Table 7.1: Expected and observed 95% C.L. upper limits on $\sigma \times \text{BR}(W' \rightarrow t\bar{b})$ as function of $M_{W'}$ for 1.9 fb^{-1} , including both statistical and systematic uncertainties.

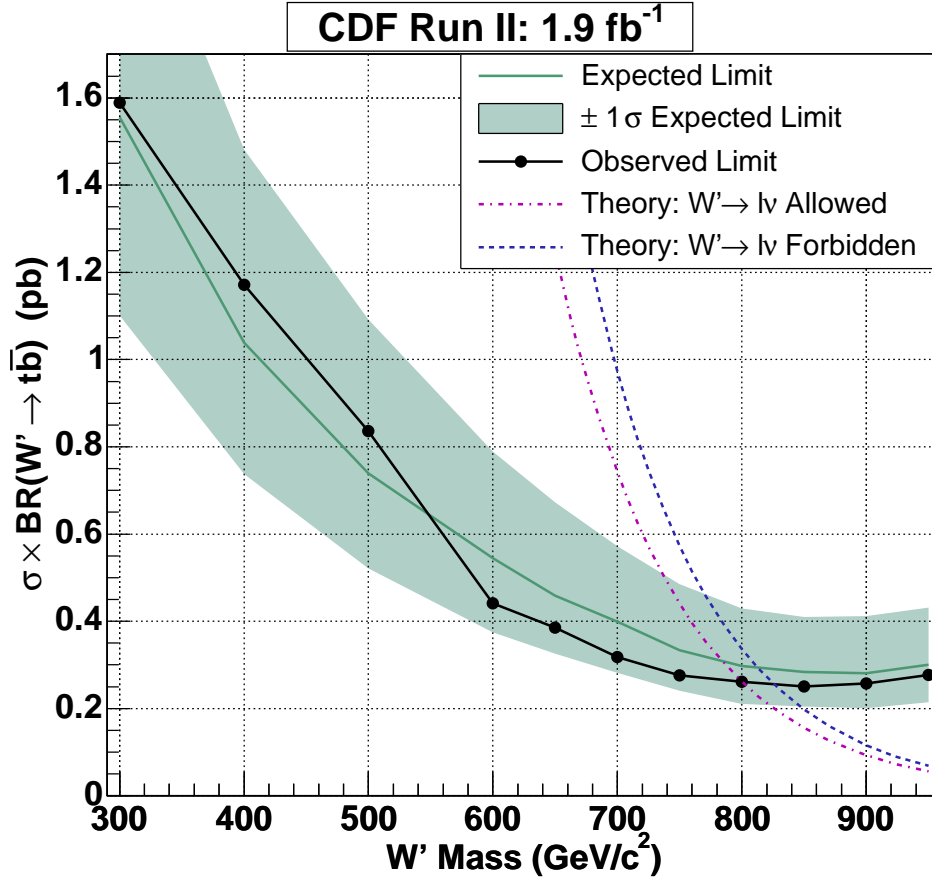


Figure 7.1: Expected and observed 95% C.L. limits on $\sigma \times \text{BR}(W' \rightarrow t\bar{b})$ as function of $M_{W'}$ for 1.9 fb^{-1} , along with theoretical predictions for a W'_R with Standard Model coupling strength.

the effective coupling to be less than 0.40 of the standard weak coupling.

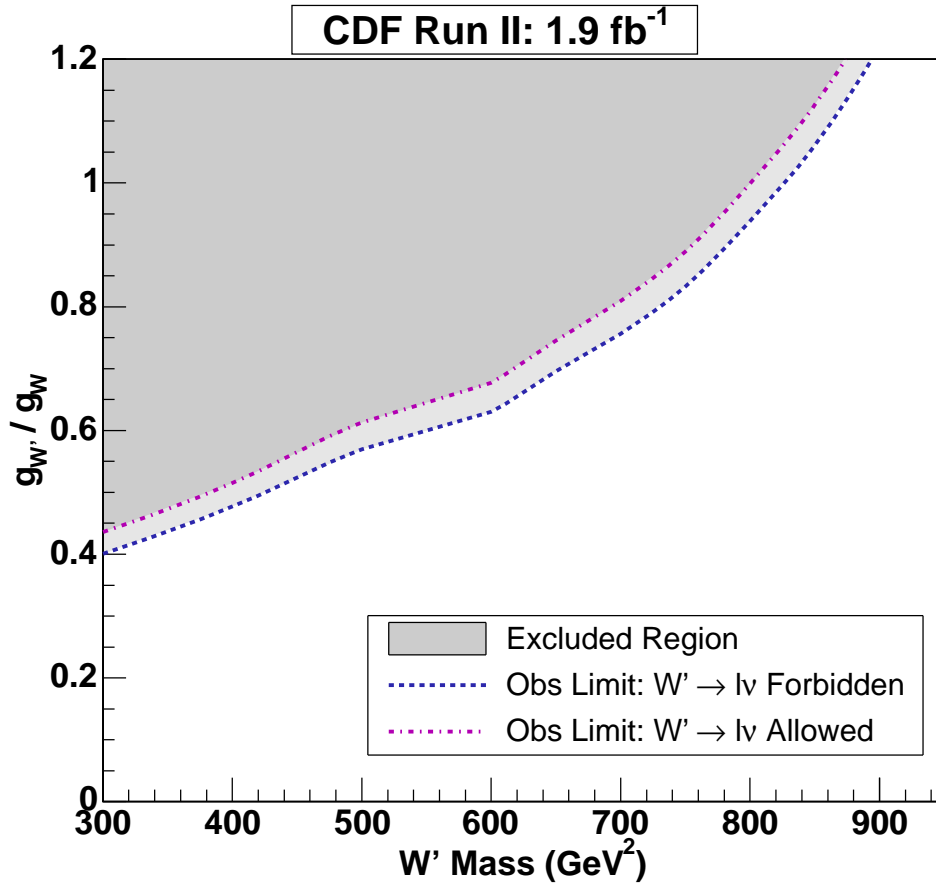


Figure 7.2: Observed 95% C.L. upper limits on the W' coupling strength compared to the Standard Model coupling, $g_{W'}/g_W$, as function of $M_{W'}$ for 1.9 fb^{-1} . The shaded regions above the lines are excluded.

BIBLIOGRAPHY

- [1] S. Glashow, Nucl. Phys. **22** 579 (1961);
S. Weinberg, Phys. Rev. Lett. **19** 1264 (1967).
- [2] D. Gross, F. Wilczek, Phys. Rev. D **8** 3633 (1973).
- [3] F. Abe *et al.*, (CDF Collaboration), Phys. Rev. Lett. **74**, 2626, (1995); S. Abachi *et al.*, (DØ Collaboration), Phys. Lett. B **74**, 2632 (1995).
- [4] A. Thalappillil, *Majorana Neutrinos and their Properties*, Available at: <http://home.uchicago.edu/~madhav/majorana.pdf>.
- [5] University of Bonn Physics Dept., Available at: http://lxa.physik.uni-bonn.de/outreach/wyp/exercises/hands-on-cern/old_pt/stdmod/stdmod.htm.
- [6] C. Amsler *et al.*, (Particle Data Group), Phys. Lett. B **667**, 1 (2008).
- [7] W.M. Yao *et al.*, (Particle Data Group), J. Phys. G **33**, (2006) pp. 183-190.
- [8] Wikipedia, *The Standard Model*, Available at: http://en.wikipedia.org/wiki/Standard_Model.
- [9] W.M. Yao *et al.*, (Particle Data Group), J. Phys. G **33**, (2006) pp. 197-203.
- [10] T. Aaltonen *et al.*, (CDF Collaboration), Phys. Rev. Lett. **100**, 231801 (2008); T. Aaltonen *et al.*, (CDF Collaboration), Phys. Rev. D **77**, 051102 (2008).
- [11] Y. Mimura, S. Nandi, Phys. Lett. B **538**, 406 (2002); G. Burdman, B. Dobrescu, E. Ponton, Phys. Rev. D **74**, 075008 (2006).
- [12] E. Malkawi, T. Tait, C.P. Yuan, Phys. Lett. **385**, 304 (1996); H. Georgi, E. Jenkins, E. Simmons, Nucl. Phys. B **331**, 541 (1990).
- [13] M. Perelstein, Prog. Part. Nucl. Phys. **58**, (2007).
- [14] J.C. Pati, A. Salam, Phys. Rev. D **10**, 275 (1974); R.N. Mohapatra, J.C. Pati, Phys. Rev. D **11**, 566 (1975); G. Senjanovic, R.N. Mohapatra, Phys. Rev. D **12**, 1502 (1975).
- [15] V.M. Abazov *et al.*, (DØ Collaboration), Phys. Rev. Lett. **100**, 031804 (2008); A. Abulencia *et al.*, (CDF Collaboration), Phys. Rev. D **75**, 091101 (2007).
- [16] V.M. Abazov *et al.*, (DØ Collaboration), Phys. Rev. Lett. **100**, 211803 (2008); D. Acosta *et al.*, (CDF Collaboration), Phys. Rev. Lett. **90**, 081802 (2003).
- [17] Z. Sullivan, Phys. Rev. **D66** 075011, (2002).
- [18] E. Boos *et al.*, Phys. Lett. B **655** 245 (2007).
- [19] D. McGinnis *et al.*, *The Run II Handbook*, Fermi National Accelerator Lab, (2000).
- [20] J. Marriner, Nucl. Instrum. Meth. A **532** 11 (2004).

- [21] D. Amidei *et al.*, *The CDF II Detector Technical Design Report*, FERMILAB-PUB-96-390-E, Fermilab National Accelerator Lab, (1996).
- [22] CDF Collaboration, *Measurement of Single Top Quark Production in 2.2 fb^{-1} of CDF II Data using the Matrix Element Technique*, CDF Note 0223, CDF Collaboration, (2008).
- [23] F. Canelli *et al.*, *Increasing Muon Acceptance with the MET plus Jet Trigger*, CDF Note 9105, CDF Collaboration, (2008).
- [24] H. Lai *et al.*, *Global QCD Analysis of Parton Structure of the Nucleon: CTEQ5L Parton Distributions*, Eur. Phys. Journal C, Springer, (2000).
- [25] CDF High Pt B-Tag Working Group, CDF Website, Available at: <http://www-cdf.fnal.gov/physics/new/top/2004/btag/>.
- [26] T. Sjostrand, L. Lonnblad, S. Mrenna, *PYTHIA 6.2 Physics and Manual.*, Comput. Phys. Commun. **101**, 232 (1997).
- [27] M. Mangano *et al.*, *ALPGEN, A Generator for Hard Multi-parton Processes in Hadronic Collisions*, J. High Energy Phys. **07**, 001 (2003).
- [28] G. Corcella *et al.*, *HERWIG 6: An Event Generator for Hadron Emission Reactions with Interfering Gluons*, J. High Energy Phys. **01**, 010 (2001).
- [29] F. Maltoni, T. Stelzer, *MadEvent: Automatic Event Generation with MadGraph*, J. High Energy Phys. **02**, 027 (2003).
- [30] M. Mangano *et al.*, *Matching Matrix Elements and Shower Evolution for Top-Quark Production in Hadronic Collisions*, J. High Energy Phys. **01**, 013 (2007).
- [31] S. Grinstein, *New HF Overlap Removal for Alpgen: Presentation to the CDF Top Properties Group*, Available at: http://www-cdf.fnal.gov/internal/WebTalks/Archive/0704/070427_topprop/04_Sebastian_Grinstein_1_overlap1.ps.
- [32] C. Ciobanu *et al.*, *MadEvent Signal Samples used in the Run II Single Top Search*, CDF Note 7020, CDF Collaboration, (2004); S. Budd *et al.*, *Validation of the Single-Top Samples with ZTOP NLO Calculations*, CDF Note 7701, CDF Collaboration, (2006).
- [33] J. Freeman, S. Grinstein, T. Junk, E. Palencia, *SecVtx Scale Factors and Mistag Matrices for 2.2 fb^{-1} of Data up to Period 13*, CDF Note 9280, CDF Collaboration, (2008).
- [34] T. Schwarz *et al.*, *Method II For You*, CDF Note 9185, CDF Collaboration, (2008).
- [35] J.C. Cully *et al.*, *Calibration of Heavy-Flavor Production in $W+1$ Jet Data*, CDF Note 9187, CDF Collaboration, (2008).
- [36] S. Budd, T. Junk, T. Liss, C. Neu, *Tight, Loose and Ultratight SECVTX Tag Rate Matrix with 1.2 fb^{-1}* , CDF Note 8519, CDF Collaboration, (2006).
- [37] M. Feindt, S. Richter, W. Wagner, *A Neural Network b Tagger for Single-Top Analyses*, CDF Note 7816, CDF Collaboration, (2006).
- [38] J.C. Cully *et al.*, *W' Background Model Validation*, CDF Website, Available at: http://www-cdf.fnal.gov/internal/physics/top/RunIISingleTop/Wprime/Validation_2fb.html
- [39] P. Dong *et al.*, *Single Top Validation*, CDF Website, Available at: http://www-cdf.fnal.gov/internal/physics/top/RunIISingleTop/Wprime/Validation_2fb.html.
- [40] T. Junk, *Sensitivity, Exclusion and Discovery with Small Signals, Large Backgrounds, and Large Systematic Uncertainties*, CDF Note 8128, CDF Collaboration, (2007).

- [41] S. Baker, R.D. Cousins, *Clarification of the Use of Chi-Square and Likelihood Functions in Fits to Histograms*, Nucl. Instrum. Meth. **A221** 437, (1984).
- [42] A.L. Read, *Linear Interpolation of Histograms*, Nucl. Instrum. Meth. **A425** 357, (1999).
- [43] F. James, *Minuit Reference Manual, Version 94.1*, CERN Program Library Long Writeup D506, CERN, (1994).
- [44] F. Garberson *et al.*, *Combination of the SecVtx 1.2 fb⁻¹ b-Tagging Scale Factors*, CDF Note 8666, CDF Collaboration, (2007).
- [45] S. Jindariani *et al.*, *Luminosity Uncertainty for Run II up until August 2004*, CDF Note 7446, CDF Collaboration, (2005).
- [46] B. Han, V. Biosvert, *Trigger Efficiencies for the High E_T Central Electron in the Gen 6 Data*, CDF Note 8629, CDF Collaboration, (2006); D. Hare, E. Halkiadakis, T. Spreitzer, *Electron ID Efficiency and Scale Factors for Winter 2007 Analyses*, CDF Note 8614, CDF Collaboration, (2006); U. Grundler, L. Lovas, A. Taffard, *High P_t Muons Recommended Cuts and Efficiencies for Winter 2007*, CDF Note 8618, CDF Collaboration, (2006).
- [47] C. Plager, *PDF Uncertainties*, CDF Website, Available at: http://www-cdf.fnal.gov/internal/physics/joint_physics/instructions/PDFUncertainties/pdf.html.